VANADYL TETRABUTYLTETRAKIS(DIMETHYLAMINO) PHTHALOCYANINE BASED THIN FILMS FOR ORGANIC SENSOR AND TRANSISTOR APPLICATIONS

NUR ADILAH BINTI ROSLAN

FACULTY OF SCIENCE
UNIVERSITY OF MALAYA
KUALA LUMPUR

2020

VANADYL TETRABUTYLTETRAKIS (DIMETHYLAMINO) PHTHALOCYANINE BASED THIN FILMS FOR ORGANIC SENSOR AND TRANSISTOR APPLICATIONS

NUR ADILAH BINTI ROSLAN

THESIS SUBMITTED IN FULFILMENT OF THE REQUIREMENTS FOR THE DEGREE OF DOCTOR OF PHILOSOPHY

DEPARTMENT OF PHYSICS
FACULTY OF SCIENCE
UNIVERSITY OF MALAYA
KUALA LUMPUR

2020

UNIVERSITY OF MALAYA
ORIGINAL LITERARY WORK DECLARATION

Name of Candidate: **NUR ADILAH BINTI ROSLAN**

Matric No: **SHC160009**

Name of Degree: **DOCTOR OF PHILOSOPHY**

Title of Thesis:

CHARACTERIZATION OF VANADYL TETRABUTYLTETRAKIS (DIMETYLAMINO) PHTHALOCYANINE (VTP) THIN FILMS FOR ORGANIC SENSORS AND TRANSISTORS

Field of Study: **EXPERIMENTAL PHYSICS**

I do solemnly and sincerely declare that:

(1) I am the sole author/writer of this Work;
(2) This Work is original;
(3) Any use of any work in which copyright exists was done by way of fair dealing and for permitted purposes and any excerpt or extract from, or reference to or reproduction of any copyright work has been disclosed expressly and sufficiently and the title of the Work and its authorship have been acknowledged in this Work;
(4) I do not have any actual knowledge nor do I ought reasonably to know that the making of this work constitutes an infringement of any copyright work;
(5) I hereby assign all and every rights in the copyright to this Work to the University of Malaya ("UM"), who henceforth shall be owner of the copyright in this Work and that any reproduction or use in any form or by any means whatsoever is prohibited without the written consent of UM having been first had and obtained;
(6) I am fully aware that if in the course of making this Work I have infringed any copyright whether intentionally or otherwise, I may be subject to legal action or any other action as may be determined by UM.

Candidate's Signature Date:

Subscribed and solemnly declared before,

Witness's Signature Date:

Name:

Designation:

CHARACTERIZATION OF VANADYL TETRABUTYLTET(DIMETYLAMINO) PHTHALOCYANINE (VTP) THIN FILMS FOR ORGANIC SENSORS AND TRANSISTORS

ABSTRACT

Organic electronic devices have been successively making progress into the commercial market to substitute conventional inorganic electronic devices. The endeavor to improve the performance displayed by organic semiconductor materials has urged a substantial number of researchers set to seek new materials. Metal phthalocyanines (MPcs), in particular, have garnered much attention due to their enticing benefits viz., cost efficiency, eco-friendly organic material, as well as thermal and chemical stability. Primarily, this study investigated the physical, morphological, optical, and electrical properties of vanadyl 3,10,17,24-tetra-tert-butyl-1,8,15,22-tetrakis(dimethylamino)-29H,31H-phthalocyanine or synonymously known as vanadyl tetrabutyltetrakis (dimethylamino) phthalocyanine (VTP). Subsequently, this study looked into the potential applications of VTP-based organic semiconductor devices in organic field effect transistor (OFET), as well as optical and humidity sensor. The initial phase of this study is devoted to the characterization of VTP thin films and fabrication of VTP-based OFETs. The photophysical study revealed that the band gap of VTP is 1.39 *eV* via expression approach, while 1.42 *eV* via Tauc plot. The highest occupied/lowest unoccupied molecular orbital (HOMO/LUMO) values of VTP were -5.10 *eV* and -3.90 *eV*, respectively, as determined via cyclic voltammetry (CV) analysis. The VTP was applied as the active layer in the fabrication of lateral OFETs (LOFETs), which served as a control device, whereby fixed parameters were employed for each layer, similar for the fabrication of vertical OFETs (VOFETs). The LOFETs exhibited poor performance due to the extended channel length between source and drain (S-D) electrodes. In the attempt of addressing this shortcoming, apart from enhancing the performance of LOFETs; the arrangement was altered to resemble that of VOFET, in which capacitor and diode cells were vertically stacked on top of each other. This design minimized the channel length and enhanced the device performance. In attaining optimum thickness for the active layer, VOFET was fabricated with a range of thicknesses; 90 ± 5 nm, 66 ± 5 nm, and 52 ± 5 nm. As a result, VTP thickness at 66 ± 5 nm exerted optimum performance, as it generated maximum current density and the lowest threshold voltage of ~ 37 mA/cm^2 and 7.0 ± 0.2 *V*, respectively. The second phase of this study probed into the fabrication of VTP-based optical organic devices. Initially, the study of optical properties and charge transport via current-voltage (*I-V*) method was executed. Utilizing the optimized bulk heterojunction (BHJ), ITO/PEDOT:PSS/VTP:PC$_{71}$BM/Al organic photovoltaics (OPVs) were fabricated by using the solution processed technique. By employing the similar OPV fabrication parameters, the device was used for light sensing application, which falls under the organic optical device category. The light sensor appeared to display high stability, rapid response time, and high sensitivity in the visible light. These features are attributable to the extended ligands in the molecular structure of VTP. The final phase of this study assessed the applicability of VTP as an active layer in the fabrication of organic humidity sensor. Physical characterization that involved structural and wettability evaluations were executed in advance to determine the association between the thickness of sensing film and the performance exerted by the sensor. The Al/VTP/Al humidity sensor devices were fabricated in three thickness values, which revealed that the thinnest sensing film displayed the best performance with a maximum sensitivity of 9.2 pf/%RH. In sum, this study had successfully adopted highly reproducible, solution generating, and cost-efficient fabrication techniques.

Keywords: VTP, OFETs, Light sensing, Organic humidity sensor

PENCIRIAN VANADYL TETRABUTYLTETRAKIS (DIMETHYLAMINO) PHTHALOCYANINE (VTP) BERASASKAN FILEM NIPIS UNTUK APLIKASI SENSOR DAN TRANSISTOR ORGANIK

ABSTRAK

Peranti organik elektronik menghasilkan kemajuan dengan pesat ke dalam pasaran komersil dalam menggantikan peranti elektronik konvensional. Oleh itu, usaha untuk meningkatkan prestasi peranti yang dimiliki oleh bahan organik semikonduktor telah menggalakkan penyelidik mencari bahan-bahan baru. Logam Phthalocyanine (MPcs) khususnya, mendapat perhatian yang sangat baik kerana ianya menawarkan kelebihan yang menarik, kos rendah, bahan organik yang mesra alam, serta stabil secara termal dan kimia. Kerja-kerja ini terutamanya tertumpu kepada kajian sifat fizikal dan elektrik vanadyl 3,10,17,24-tetra-tert-butil-1,8,15,22-tetrakis (dimethylamino) -29H, 31H-phthalocyanine atau dikenali sebagai vanadyl tetrabutyltetrakis (dimethylamino) phthalocyanine (VTP) dan seterusnya, menerokai potensi aplikasinya dalam peranti elektronik, cahaya dan sensor kelembaban. Bahagian pertama kajian ini ditumpukan kepada pencirian filem nipis VTP dan fabrikasi peranti elektronik berasaskan VTP. Kajian fotofizikal dan elektrokimia telah menunjukkan bahawa jurang tenaga VTP bersamaan dengan 1.39 *eV* dan tahap HOMO / LUMO VTP yang ditentukan ialah masing-masing, -5.10 *eV* dan -3.90 *eV*. Selanjutnya, VTP digunakan sebagai lapisan aktif dalam fabrikasi susunan sisi organik transistor (LOFET), yang bertindak sebagai peranti kawalan. LOFET mempunyai prestasi yang sangat rendah kerana saiz saluran panjang yang besar antara elektrod sumber dan longkang. Untuk mengatasi had ini serta untuk meningkatkan prestasi OFET sisi, susunan telah diubah menjadi susunan menegak (VOFET), di mana sel kapasitor dan sel diod diatur secara menegak di atas satu sama lain. Reka bentuk sedemikian telah didapati dapat mengurangkan panjang saluran dan akibatnya, prestasi peranti dapat ditingkatkan. Untuk mendapatkan ketebalan optimum lapisan aktif yang diperlukan, VOFET telah disediakan dengan ketebalan yang berbeza dari 90 ± 5 nm, 66 ± 5 nm dan 52 ± 5 nm. Telah didapati bahawa peranti dengan ketebalan VTP 66 ± 5 nm menunjukkan prestasi yang optimum, dengan memberikan kepadatan arus maksimum dan voltan ambang terendah, masing-masing sekitar 37 mA/cm^2 dan 7.0 *V*. Fasa kedua kerja ini difokuskan pada fabrikasi peranti organik optik berasaskan VTP. Sebelum itu, kajian mengenai sifat optik dan kajian pengangkutan caj melalui kaedah voltan semasa (*I-V*) telah ditunjukkan. Dengan menggunakan optimum pukal hetero-simpang, ITO/PEDOT: PSS/VTP:PC$_{71}$BM/Al organik sel suria telah disediakan dengan teknik proses larutan. Oleh kerana kecekapan penukaran kuasa yang rendah, aplikasi peranti telah ditukar kepada aplikasi sensor cahaya. Sensor cahaya tersebut telah menunjukkan masa tindak balas yang sangat stabil dan pantas dan sensitiviti tinggi dalam cahaya nampak. Hal ini mungkin boleh dikaitkan dengan ligan yang panjang dalam struktur molekul VTP. Bahagian terakhir kerja ini membincangkan penggunaan VTP sebagai lapisan aktif dalam pembuatan sensor organik kelembapan. Pengkajian fizikal mengenai ujian struktur dan pembasahan telah dilakukan terlebih dahulu untuk mengkaji kesan ketebalan filem terhadap prestasi sensor. Peranti sensor kelembapan Al/VTP/Al telah dibuat dalam 3 ketebalan yang berbeza dan hasilnya menunjukkan bahawa filem penderiaan nipis mempunyai prestasi terbaik. Kerja-kerja semasa adalah berdasarkan teknik-teknik fabrikasi yang berjaya dihasilkan berulangkali dengan penyediaan yang rendah.

Kata kunci: VTP, OFET, Sensor cahaya, Sensor organic kelembapan

ACKNOWLEDGEMENTS

First of all, I am beyond grateful to Allah Almighty the most Merciful and the most Beneficient for the strength He has given me to complete the biggest achievement of my life. It has been a very tough journey with full of bumps and obstacles during the ride. This day would not have come without the help and prayers of many people.

I would like to express my deepest appreciation to my supervisors, Dr. Azzuliani Supangat and Professor Dr. Wan Haliza Abd. Majid for their incredibly support, knowledge, advice, guidance and encouragement throughout this journey. Thank you so much for trusting me and never give up on me until the end of my study. Also, I am extremely grateful to my co-advisor, Dr. Shahino Mah Abdullah for his willingness to share ideas and help me to complete this work. He is a great mentor and always inspire people to do research. Special thanks to my group mates, especially to Dr. Asmaliza, Dr. Saipul and Afiq for their help and support along this journey. I would extend my appreciation to my lab member, Dr. Mohd Arif for always giving me ideas whenever I feel stuck to do experiment. Many thanks to my colleagues of the LDMRC in the Department of Physics, University of Malaya for their always prompt help, whenever I needed it. I would also like to extend my deepest gratitude to my good friends, Dr. Azmina and Dr. Fairus for always having my back!

Most important, my deepest appreciation goes to my beloved family especially my parents, for always encourage me and become a constant source of moral and emotional support. I am forever indebted to them. I would like to thank to the Ministry of Higher Education and University Putra Malaysia for the scholarship and financial support. Last but not the least, thank you to everyone, who is not, mentioned here, for his/her contribution, direct or indirect during the completion of my research work.

TABLE OF CONTENTS

LIST OF FIGURES

LIST OF TABLES

LIST OF SYMBOLS AND ABBREVIATIONS

J : Current density

I_{max} : Current at maximum power

μ : Charge carrier mobility

ε : Dielectric constant

V_{DS} : Drain-source voltage

e : Electronic charge unit

FF : Fill factor

ν : Frequency

V_{GS} : Gate-source voltage

P_{in} : Input power

C_{max} : Maximum capacitance

RH_{max} : Maximum relative humidity

P_{max} : Maximum power

C_{min} : Minimum capacitance

RH_{min} : Minimum relative humidity

V_{oc} : Open circuit voltage

E_{OX} : Oxidation energy

E : Photon energy

h : Planck’s constant

η : Power conversion efficiency

E_{RED} : Reduction energy

R_s : Series resistance

I_{sc} : Short circuit current

J_{sc} : Short circuit current density

R_{sh} : Shunt resistance

V_{th} : Threshold voltage

θ : Trap factor

V_{max} : Voltage at maximum power

λ : Wavelength

AgNWs : Silver nanowires

BHJ : Bulk heterojuntion

EQE : External quantum efficiency

ETL : Electron transport layer

HTL : Holes transport layer

HOMO : Higher occupied molecular orbital

ITO : Indium-tin-oxide

LUMO : Lower unoccupied molecular orbital

OFET : Organic field effect transistor

OLED : Organic light emitting diode

PC$_{71}$BM : (6,6)-phenyl C71 butyric acid methyl ester

PEDOT:PSS : Poly(3,4-ethylenedioxythiophene):poly(4-styrenesulfonic) acid

VOPcPhO : Vanadyl 2,9,16,23-tetraphenoxy-29H,31H-phthalocyanine

VTP : Vanadyl 3,10,17,24-tetra-tert-butyl-1,8,15,22-tetrakis(dimethyl-lamino)-29H,31H-phthalocyanine / vanadyl tetrabutyltetrakis (dimethylamino) phthalocyanine

CHAPTER 1: INTRODUCTION

1.1 Introduction

Organic electronics is a branch of modern electronics that has been regarded as a multidisciplinary subject. It combines the investigation within the fields of physics and chemistry, by incorporating the synthesis of organic polymer/molecules, as well as preparation and fabrication of electronic devices. Typically, the organic materials used are made up of carbon that resembles the molecules of living things. In 1977, Heeger, Shirakawa, and MacDiarmid discovered a highly conductive polymer called polyacetylene (Bredas et al., 2002). A decade later, organic electronics application was still absent. Until in the mid-1980s, growing interest was noted for organic conductive materials within the engineering and applied physics domains, hence the advent of a new technology with a new market, namely polymer or plastic electronics (Zhou et al., 2014).

Until to date, such devices are still inferior when compared to the standard silicon-based electronic devices in light of performance and durability. As stipulated in the Organic Electronics Market Research Report 2018, the demand for global organic electronics has been expected to be one of the fastest growing markets worth billions of dollars by year 2027, primarily due to its benefits to the environment, better resource utilization, and most importantly, lower in cost when compared to conventional inorganic electronics.

Among the vast range of organic materials, metal phthalocyanines (MPcs) have drawn substantial interest as molecular materials as they contribute to prominent optical and electrical properties (Torre et al., 2007; Rossi et al., 2016). In the past few decades, MPcs have been aggressively studied as active materials for electronic devices, such as sensors, organic field effect transistors (OFETs), organic solar cells (OPVs), as well as optical switching and limiting devices. Generally, phthalocynanines (Pcs) are composed of a nitrogen-linked tetrameric diiminoisoindoline conjugated macrocyle. The MPc is a highly stable material due to the chelate of metal with two covalent and two coordination bonds, which can function as dyes and pigment, as well as active materials in organic electronic devices (Dahlen, 1939; Li et al., 2008; Yuen et al., 2012). In light of synthesis process, most MPcs are relatively inexpensive and easily purchased in large-scale production from major chemical manufacturers. Such alluring factors have turned MPcs into a favorable material for vast commercial applications, with extended research laboratories continuously exploring their potential in a range of device applications.

The search of a new material is indeed preponderant to ascertain the growth of organic devices market. Ultimately, this study investigated in an in-depth manner the properties of a newly reported organic material, which refers to vanadyl tetrabutyltetrakis(dimethylamino) phthalocyanine (VTP) by evaluating the performance of fabricated organic electronic devices, namely organic thin film OFETs, OPVs, organic photodetector (OPD), and organic humidity sensors. Detailed characterization prior to the fabrication of each device is presented, so as to highlight and optimize the new properties of VTP thin film.

1.2 Research motivations

To date, several commercial electronic devices, such as transistors, solar cells, data storage memories, and sensors, are predominantly silicon-based (inorganic material) that exhibit exceptional performance with impressive stability. Nonetheless, these electronics semiconductor material devices are cost-inefficient in terms of its materials and demand energy-intensive processing technologies (Braga et al., 2008; Garnett & Yang, 2010; Huang et al., 2009). That being mentioned, a number of researchers have begun utilizing organic semiconductor materials to address the shortcomings of the conventional silicon-based inorganic electronics devices. Organic semiconductors, on contrary to their inorganic counterpart, are cost-efficient, generate viable solutions, and uphold environment-friendly fabrication processes. This is attributable to the weak intermolecular interactions that exist in the materials, which lead to low-temperature and high-throughput solution-based processing techniques, for instance, spin coating, inkjet printing (Aernouts et al., 2008), and spray deposition (Krebs, 2009).

Ahmad Makinudin & Supangat (2016) reported on the incorporation of fullerene as an acceptor with *p*-type conjugated small molecule organic material that is VTP. The outcomes displayed exceptional properties suitable for application in electronic devices. No work, however, has applied VTP as the active layer in fabricating organic electronics devices. The presence of extended π-orbital has been suggested to enable attainment of characteristics related to charge-transport and optical properties. It may also increase the solubility properties, which is integral for inexpensive processes by means of solution methods (Usta & Facchetti, 2015). Therefore, the extended ligands present in the macro-rings of Pcs have garnered considerable attention to investigate in depth about their properties, and the efficient performance of organic electronic devices, such as OFET, OPV, OPD, and organic humidity sensor.

Past studies have reported that alteration of OFET from lateral to vertical arrangement automatically reduces the channel length between source and drain (S-D) electrodes (Kudo et al., 2001; Kvitschal et al., 2015; Ma & Yang, 2004). Such arrangement permits the possibility of low-working voltages and high-current outputs (Ma & Yang, 2004). Halizan et al., (2017) revealed improved working voltages for vertical OFET (VOFET) with vanadyl phthalocyanine derivative (VOPcPhO) as the active layer. However, no work has used VTP as the active layer in fabricating OFET to assess the impact of varied extended ligands on the performance of VOFET, in comparison to the above study.

The presence of π-conjugated organic semiconductors seems to be attractive due to its tunable spectral sensitivity. In precise, Pcs molecules are mostly conjugated as it is composed of π-electron system (Di Natale et al., 1998), which is the key for their exceptional photosensitivity (Oleinick et al., 1993). Zafar et al., reported the fabrication of OPD using VOPcPhO and PCDTBT as the active layer in the device (Zafar et al., 2016). Nevertheless, none has incorporated VTP in the fabrication of OPV and OPD.

The application of VTP as the active layer in fabricating organic humidity sensor is motivated by the conjugated π-system and the porous nature of MPc, which is responsible for its highly sensitive attribute in ambient conditions (Ahmad et al., 2011). Besides, the sensing film of humidity sensor device highly depends on the thickness and the morphology of the film (Farahani et al., 2014). Despite the low sensitivity exerted by organic-based humidity sensor devices, there is always room to seek a better material. In search of a new material, it is significant to enhance the device sensitivity and to determine the effect of extended ligands on the sensitivity performance.

Hence, the motivation and aim of this study is to explore the utilization of VTP-based organic devices due to the presence of extended ligands in the macrocycle rings. The solution processed technique was selected for device fabrication due to its simplicity, versatility, and cost efficiency.

1.3 Objectives

This present study fabricated VTP-based organic transistors and sensors by using the simple and low-cost solution processed technique. The overarching aim of this PhD thesis is to study in detail the characterization of VTP thin films to determine their physical, electrical, structural, and morphological properties, as well as to explore the potential of VTP-based organic devices. The specific aims of this present study are as follows:

1. To characterise in-depth the optical, structural, and electrical properties of VTP thin films.
2. To evaluate the performance of different architectures of VTP-based OFET.
3. To study the performance of VTP-based optical devices.
4. To optimize the VTP-based organic humidity sensor by varying the thickness of the sensing layer.

1.4 Thesis framework

Chapter 1 presents a brief introduction about organic semiconductor materials, particularly MPcs derivative. Next, it describes the motivations behind this study and its objectives. **Chapter 2** reviews the general comparison of inorganic and organic semiconductor materials, especially metallophtahlocyanines. The mechanism and working principle of organic devices are highlighted in detail. Next, **Chapter 3** covers the details of materials used throughout this thesis, procedure of device fabrications, and a brief description regarding thin film characterization methods. The measurement techniques of each device are also presented in this chapter.

The following three chapters (Chapters 4 – 6) presents the results, some of which have already been published. Despite the elaboration of varied projects, these three chapters are essentially interlinked with the aim to examine the properties of VTP, as well as the fabrication of VTP-based organic transistors and sensors. **Chapter 4** examines the VTP-based electronic devices that embed different architectures of OFET. Characterizations to determine the optical band gap and the highest occupied/lowest unoccupied molecular orbital (HOMO/LUMO) levels were performed prior to the device fabrications. **Chapter 5** describes the utilization of VTP as the active layer in analysing the photovoltaic effects of OPVs and OPDs application. Beforehand, several characterizations were executed to optimize the blended ratio of donor and acceptor system. **Chapter 6** presents the employment of a range of thicknesses for the VTP as an active layer in organic humidity sensor. The physical, structural, and chemical characterizations were carried out to better understand the mechanism of the sensor. Finally, the overall conclusions of this work and the future research directions are presented in **Chapter 7**.

CHAPTER 2: LITERATURE REVIEW

2.1 Introduction

This chapter presents the literature review pertaining to organic semiconductor materials and theory related to organic electronic devices applied in this thesis. The general review concerning organic semiconductor materials in terms of their molecular orbital (MO) are discussed in Section 2.2. A review that emphasizes on MPc-based organic electronic devices is given in Section 2.3. Finally, the physics underlying the operation of organic electronic devices assessed in this study, namely OFET, OPD and organic humidity sensors, is elaborated in Section 2.4.

2.2 Organic semiconductor materials

Organic semiconductor materials refer to materials that exhibit semiconducting properties that are classified into polymers and small molecule materials. The main variance between these two types of materials lies in their chemical properties. A polymer reflects a macromolecule that is composed of a repetition of a fundamental unit called monomers, whereas small molecule materials consist of small molecules. These materials can dissolve in common organic solvents. These two types of materials contain alternating single and double carbon bonds, known as pi (π) conjugation. A conjugated system allows the delocalization of electrons in a molecule, aside from contributing to unique semiconducting and optical properties. In a conjugated system, the overlapping between the p_z-orbitals of sp^2-hybridised carbon atoms can generate molecular π-orbitals. The electron fills in these molecular π-orbitals are delocalised throughout the conjugated system. Figure 2.1 illustrates an instance of π-orbital and delocalised electron distribution, while Figure 2.2 displays the molecular structures of small molecule and polymeric materials.

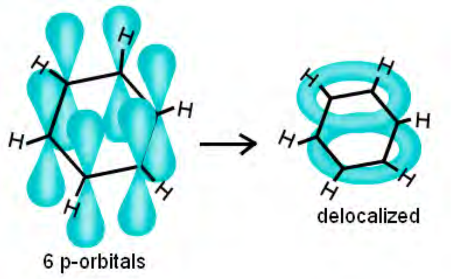

Figure 2.1: A π-orbital of conjugated system in benzene ring (Speight, 2019)

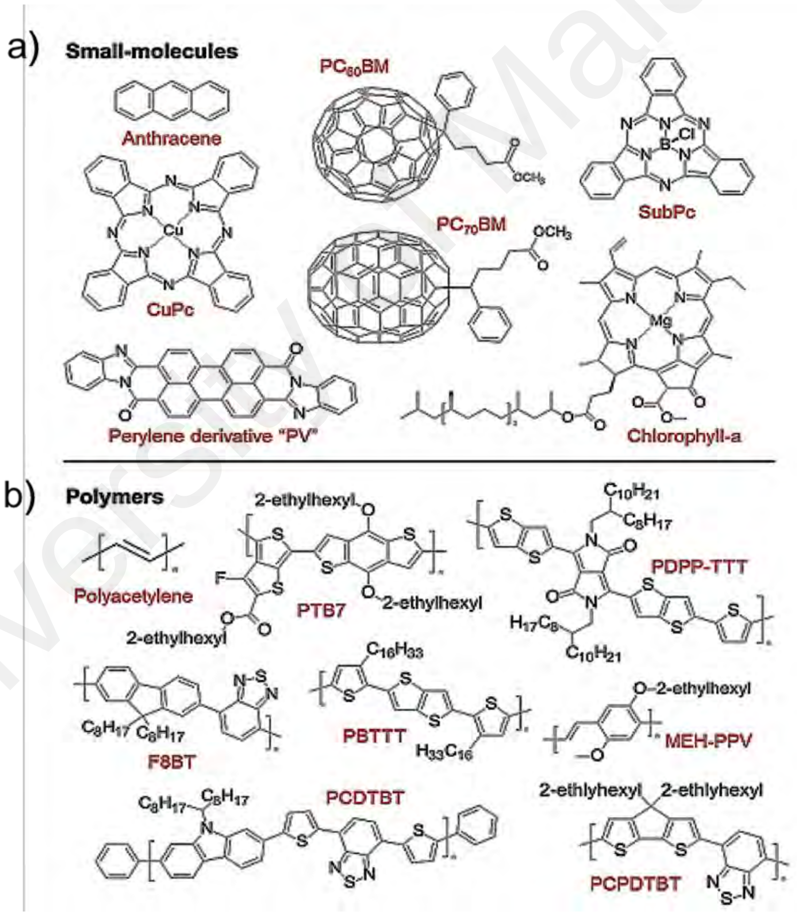

Figure 2.2: Molecular structure of: a) conjugated small molecules, and b) conjugated polymers (Zhang et al., 2018)

In the molecular π-conjugated system, the formation of π-bonds is responsible for current conduction, apart from providing the splitting of electron energy levels. If the energy of MO is less than the original atomic orbitals, it is known as bonding π-orbitals, while anti-bonding (π^*)-orbitals for otherwise. Both the bonding and anti-bonding states are also known as HOMO and LUMO, respectively. Figure 2.3 portrays an illustration of energy level splitting.

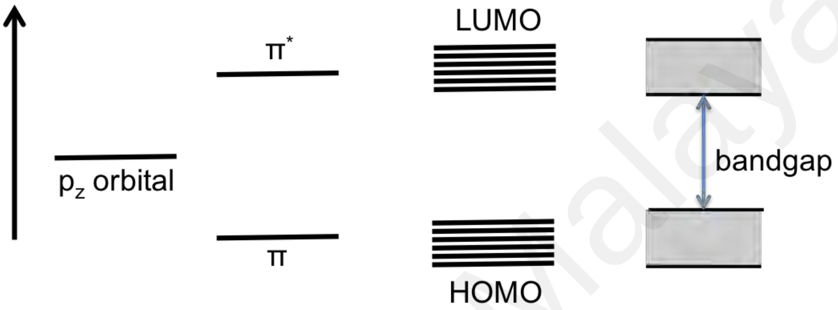

Figure 2.3: Schematic illustration of the energy level splitting

Figure 2.4 presents the energy levels that are responsible for charge transfer. Both HOMO and LUMO states tend to correspond to ionization potential (IP, or ionization energy) and electron affinity (EA), respectively, with reference to vacuum level. The HOMO and valence bands in organic and inorganic semiconductors, respectively, are analogous, and the same apply to LUMO and conduction bands. The HOMO level serves as a hole transport medium, while the LUMO level is responsible for electron transport. In transporting electrons, the energy levels must be aligned in such a manner that LUMO levels of donor and acceptor, as well as the work function of cathode, should appear in descending steps. As carriers in organic semiconductor are transported by hopping mechanism, the variances between the energy levels (donor, acceptor, and electrodes) ease the carrier to hop across the junction during transportation.

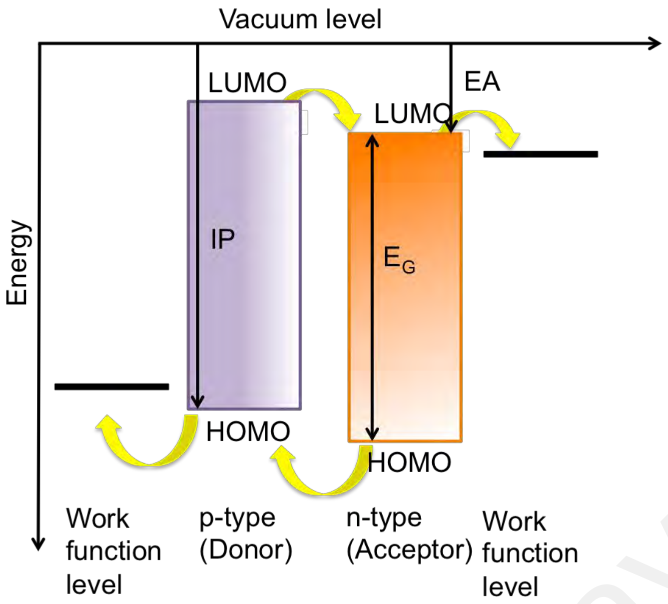

Figure 2.4: Example of energy levels for charge transfer

Typically, organic materials possess very slow mobility of charge carriers due to the disordered structure at the molecular level. In organic semiconductor, electrical current conduction is only possible with the movement of delocalized π-electrons (Brédas et al., 2004). The charge generation mechanism, however, is not limited within the organic material itself, as the charges are injected from electrode into organic materials. The structure of organic materials is highly disordered, when compared to crystalline inorganic silicon. Due to the presence of multiple traps and defects in the molecular level structure, the movement of charge carrier adheres to the hopping mechanism to generate conduction. Localized states are created due to these defects and disordered molecular structure. The charge carriers that hop and get trapped between the localized states lead to low mobility attribute (Gupta, 2007).

2.3 Metal phthalocyanine and its derivative

In the past few decades, extensive efforts have been made by researchers to develop new organic materials that can boost the performance of organic electronic devices. Parallel to this, Pcs have received much attention as molecular materials due to their outstanding electronic and optical properties, as well as their electronic delocalization, to function as active components in organic electronic devices (Torre et al., 2007). Figure 2.5(a) displays the structure of Pc that consists of 18 π electron aromatic porphyrin (Por) and four isoindole subunits that are linked via nitrogen atoms. Vast modifications have been made and incorporated by substituting more than 70 different metal atoms into the two hydrogen atoms of the central cavity (known as metallophthalocyanine or MPc) (see Figure 2.5(b)) (Przybyl & Janczak, 2014), which permits the fine tuning of the physical properties (Claessens et al., 2008). The versatility of Pcs can be defined by means of altering the physical, electronic, and optical properties through the selection of central metal atoms, as well as via chemical substitution at the periphery of the macrocycle and/or at the axial positions.

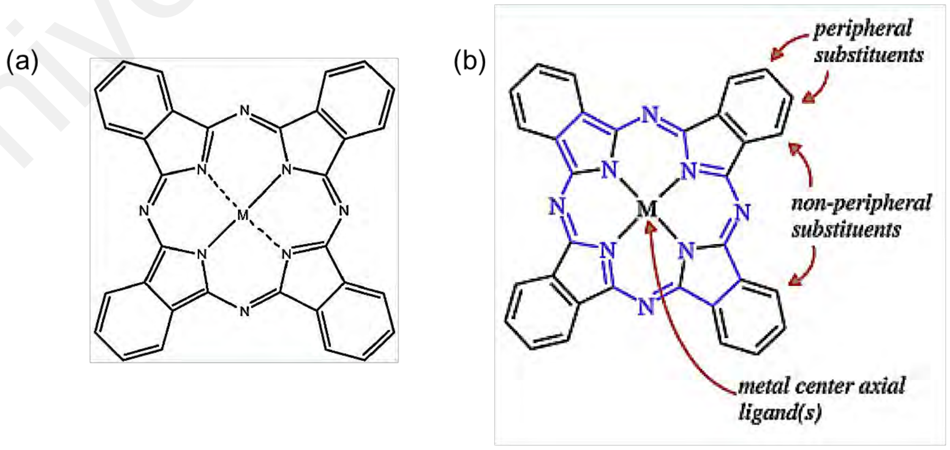

Figure 2.5: (a) Phthalocyanine body structure (Torre et al., 2007) and (b) possible modifications of metallophthalocyanine structure (Przybyl & Janczak, 2014)

As displayed in Figure 2.5(a), the Pc structure has no substituent at the periphery, this resulting in low solubility in most organic solvents due to strong stacking interaction between the molecules in the solid-state (Przybyl & Janczak, 2014). These thin Pc films still can be formed via vacuum evaporation, as it is a thermally-stable molecule that can be sublimed without decomposition. Alternatively, the substitution of Pcs in peripherical position with bulky groups or hydrocarbon chains enhances their solubility to limit the stacking interaction, and finally, allows the deposition of thin film onto the substrates via solution-processing methods (Leznoff & Lever, 1989; Claessens et al., 2008). The versatility of MPc complexes can be further investigated from their absorption spectral properties. The changes in symmetry and conjugation pathway of a porphyrin can affect its UV-Vis absorption spectrum (Gouterman, 1961; Nappa & Valentine, 1978; Rubio et al., 1999). Gouterman proposed the absorption spectrum of porphyrins theory, which can be understood in terms of the highly successful 'four-orbitals' that contain two HOMOs and two LUMOs, wherein this model is used to explain the significance of charge localization on electronic spectroscopic properties (Gouterman, 1959, 1961).

Based on Gouterman's theory, the absorption bands from the porphyrins structure are derived from the transitions between two HOMOs and two LUMOs (Gouterman, 1961). The relative energies of these transitions rely on the metal centre and the substituents in the porphyrins ring. Figure 2.6(a) illustrates the energy level diagram, in which HOMOs are categorized as a_{1u} and a_{2u} orbitals, while LUMOs reflect the degenerated set of e_g orbitals. The transitions between these orbitals give rise to two excited states. Orbital mixing splits these two states in energy; creating Soret band and Q-band, which are produced in higher energy state with higher oscillator strength, and lower energy state with less oscillator strength, respectively (Giovannetti, 2012).

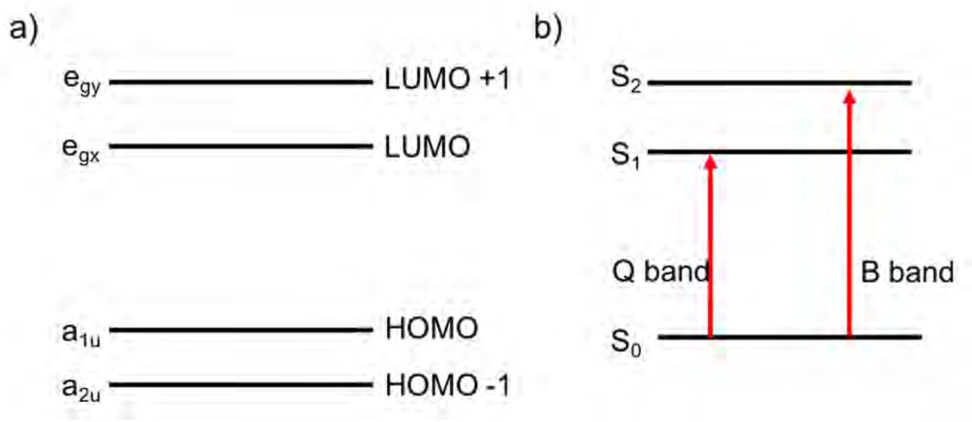

Figure 2.6: (a) Diagram of energy levels of the four Gouterman orbitals (Giovannetti, 2012) and (b) transitions that lead to Q and B bands (Hooper et al., 2018)

The electronic absorption spectrum of a typical porphyrin system is comprised of two distinct regions, as illustrated in Figure 2.6(b). The initial region lies from 380 nm to 500 nm, which is also known as Soret or B band, and it is linked to the transition from ground state to the second excited state (S0 → S2). Next, the second region, which lies between 500 nm and 700 nm, is called Q band and involves the transition from ground state to the first excited state (S0 → S1) (Giovannetti, 2012). The position of absorption bands, particularly the Q band, is affected by varying the central metal, the axial ligation, the solvents, the peripheral and non-peripheral substitutions, as well as by extension of the conjugation (Nyokong, 2010).

As a result of all the chemical versatilities mentioned above, MPcs have been widely investigated in the past few years as targets for organic devices, such as organic thin film transistor, organic light-emitting diode (OLED), OPD, optical switches, thin film solar cell, and molecular sensors (Hohnholz et al., 2000; Jiang et al., 2014; Rand et al., 2012; Warner et al., 2013).

Copper phthalocyanine (CuPc) is a well-known MPc derivative that has been applied as active layer in organic devices. For instance, Kudo et al., (Kudo et al., 2001) and Adan et al., (Kvitschal et al., 2015) developed CuPc-based organic transistor, while Farooq et al., (Farooq et al., 2015) applied CuPc to fabricate OPD, and (Karimov et al., 2017) assessed the performance of CuPc-based organic humidity sensor. Although CuPc is a suitable candidate for application in multifunctional organic devices; the absence of a substituent at the periphery causes CuPc to possess low solubility in any organic solvent. The deposition of CuPc has to be performed in vacuum evaporation, which makes it intricate and relatively a high-cost fabrication process.

Therefore, this present study focused on VTP, with the presence of hydrocarbon chain at the periphery, which in turn, enhanced the aspect of solubility. However, no study has looked into the use of VTP in the fabrication of organic device. That being said, a brief review regarding VOPcPhO is discussed in Section 2.3.1, mainly because the molecular structure of VOPcPhO resembles that of the VTP, but with variance in the extended ligands at the periphery.

2.3.1 Vanadyl phthalocyanine derivative (VOPcPhO)

The VOPcPhO has been comprehensively explored in light of its structural and spectroscopic properties (Nanai et al., 1995; Pan et al., 1998). Recently, due to its high solubility and large absorption coefficient in the Q-band region (Aziz et al., 2015), some studies had employed VOPcPhO as the active layer in organic devices, such as OPV, OPD, and organic humidity sensor (Abdullah et al., 2012; Azmer et al., 2017; Zafar et al., 2014). Meanwhile, Halizan et al., (2017) used VOPcPhO to fabricate VOFET, which yielded relatively low threshold voltage at ~10 *V*. Several research studies investigated the usage of VOPcPhO-based OPD. The best photodetector parameters reported were responsivity and photoresponse time at 5.0×10^{-4} mA/W and ~ 800 ms time, respectively (Ahmad et al., 2013; Zafar et al., 2014; Zafar et al., 2016). Hence, based on the literature mentioned above, the organic semiconductor material, VOPcPhO, can be applied in multipurpose organic devices.

Another less known organic material called vanadium derivative or VTP, has been studied by placing focus on its optical and structural properties in a prior study (Ahmad Makinudin & Supangat, 2016). The various extended ligands present in VTP, when compared to those in VOPcPhO, have an impact on optical, morphological, and electrical properties, as well as performance in organic semiconductor devices. This is attributable to the improvement noted in charge delocalization, which in turn, enhances the charge transport of VTP-based organic devices. Figure 2.7 illustrates the molecular structures of VTP and VOPcPhO, whereby VTP has extended ligands at the periphery that can improve both sensitivity and charge transport of the devices. The high solubility properties in most organic solvents of VTP can endow to facile the solution process technique via spin coating, thus minimizing the cost of fabrication process.

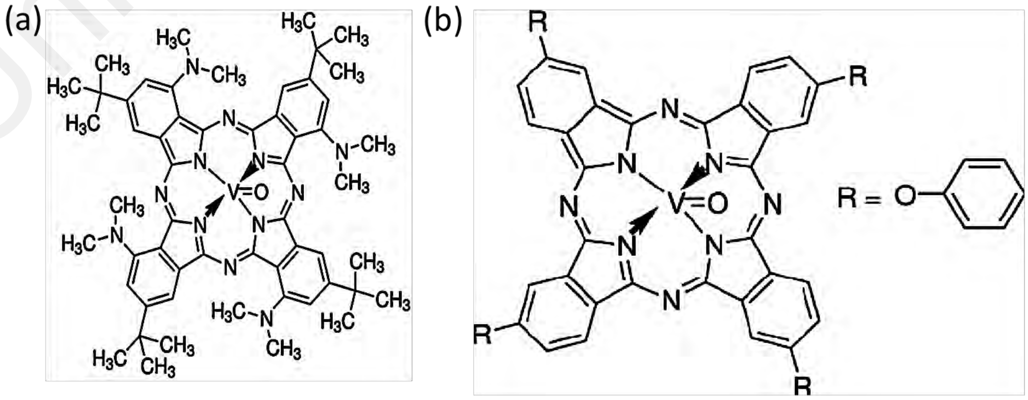

Figure 2.7: Molecular structures of a) VTP (Roslan et al., 2018) and b) VOPcPhO (Abdullah et al., 2012)

2.4 Device physics of organic electronic applications

2.4.1 Organic semiconductor materials-based electronics applications

Organic materials refer to charge-transporting medium in the mechanism of OFETs. Koezuka et al., appears to be the pioneer to introduce OFETs in year 1987 (Horowitz, 1998). The OFET device structure is composed of three electrodes (source (S), drain (D), and gate (G)), an insulating layer, and an organic semiconducting layer. The S-D electrodes are responsible for injecting and draining out charge carriers, whereas the gate electrode is used to endow a gate field and to govern the drain current. Next, the insulating layer separates and forms a barrier between the gate electrode and the organic semiconductor. The interface between insulator and organic semiconductor layer is managed by the gate field and forms a charge-transporting channel.

The OFET is grouped into two types; LOFET, and VOFET, which vary in terms of movement of charge carriers and distance of gate from S-D electrodes. In LOFET, the charge carriers move in horizontal direction between S-D electrodes, in which the channel is parallel to the gate electrode. On the other hand, the charge carriers move in vertical direction for VOFET and the channel is normal to the gate electrode. In LOFET, the gate is in equidistant with S-D electrodes; while in VOFET, the gate is closer to the source electrode than to the drain electrode. Since the organic layer in VOFET is sandwiched between S-D terminals, the channel length is dictated by the thickness of organic layer.

The two common types of measurement performed on both types of OFETs are output and transfer characteristics. Output characteristics are determined by supplying voltage between S-D terminals, V_{DS}, to measure the output current across load, I_{DS}, at a certain biasing magnitude of V_{GS}. Transfer characteristics are characterized by measuring the I_{DS} at varied V_{GS} with constant V_{DS}. These measurements offer vital parameters, which are threshold voltage and ON/OFF ratio. The description of LOFET and VOFET is given as follows:

(a) Lateral type OFET

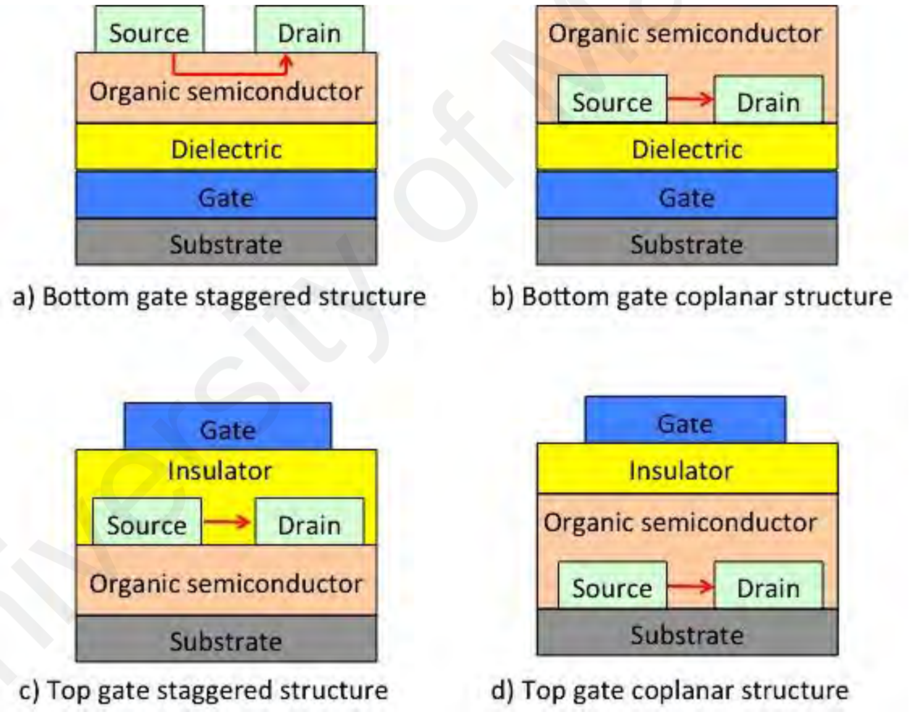

Figure 2.8: Basic configurations of LOFETs, a) bottom gate staggered structure, b) bottom gate coplanar structure, c) top gate staggered structure and d) top gate coplanar structure

The LOFET is classified into four sub-types based on its configuration; gate position (top or bottom contact) or by adjusting the position of S-D terminals (planar or staggered structure). Figure 2.8 (a-d) shows the basic configurations of LOFET. Each device configuration has its own advantages and drawbacks. In this study, the bottom gate staggered structure was selected to fabricate the OFET due to its benefits in terms of charge injection that provides continuous charge concentration in the whole channel area (Kim et al., 2011).

Figure 2.9 illustrates the operation of LOFET. A gate voltage is biased to govern the amount of current flow between S-D terminals. The most common OFET is the *p*-type due to its stability in air and relatively high mobility upon usage in OFET (Wang et al., 2009). A negative voltage that is biased between gate and source (G-S) can form a *p*-type channel at the semiconductor-insulator interface. Thus, negative voltage was applied in this study between drain and source (D-S) electrodes; causing holes charge carrier to flow from S-D electrodes. Over time, increment in the V_{DS} magnitude would contribute to the increasing magnitude of I_{DS} until it is pinched off. At this juncture, the p-channel pinches closed at one side, and results in the I_{DS} to saturate at its maximum value (Perkinson, 2007). Unfortunately, the OFET devices suffer from low mobility that causes poor performance, including low ON-current, high active voltage, and low working frequency (Tessler & Ben-Sasson, 2014).

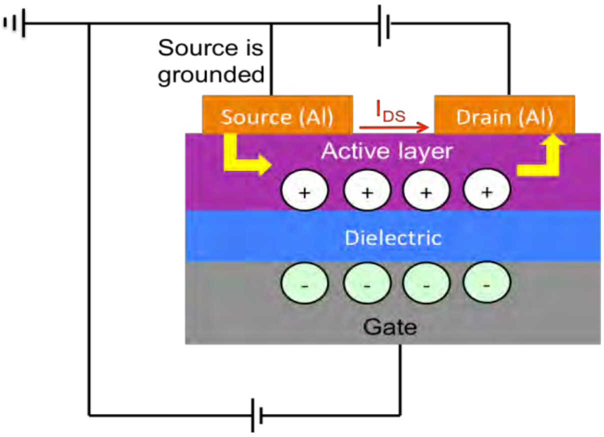

Figure 2.9: Operation mechanism of lateral OFET

(b) Vertical type OFET

Numerous attempts have been taken by researchers to gain better performance of OFET. Introduction of a new device structure is integral to address the shortcomings of OFET (Ma & Yang, 2004; Stutzmann et al., 2003). The VOFETs display a straightforward method in decreasing the dimension of lateral device. Nevertheless, limited literature describes VOFET, since this work has been reported a decade ago and it is still at its infancy stage. To date, many configurations and geometries of VOFETs have been fabricated using polymeric materials. The deposition of metals, organic semiconductors, and oxides has been executed via thermal evaporation method. Several studies have reported the use of photolithography process in fabricating the step-edge structure of VOFET (Kudo et al., 2010; Liu et al., 2010; Takano et al., 2009). Although photolithography process is somehow promising, its process is intricate with incorporation of several solvents, such as hydrofluoric (HF) acid, which is unfavorable with organic materials.

Alternatively, cost-efficient fabrication devices may be achieved by using thin film deposition techniques, such as spin coating, dip coating, and drop casting, instead of thermal evaporation or photolithography methods. Ma and Yang proposed a new architecture of VOFETs, whereby an active cell and capacitor cells are vertically stacked on top of each other (see Figure 2.10) (Ma & Yang, 2004). Over time, extensive studies have begun initiating low-cost fabrication of VOFETs using the solution-processed technique (Halizan et al., 2017; Sarjidan et al., 2018).

Figure 2.10 illustrates that the centre electrode (source) is shared by two cells, while the active and capacitor cells are defined as drain and gate electrodes, respectively. The source electrode must exhibit thin and rough surface, which is crucial for device operation. This condition ensures that the electric field generated by the charged capacitor cell does not vanish at the source/organic interface, apart from inducing positive charge in the organic layer that is close to the source/organic interface (Ma & Yang, 2004). The working principle of the VOFET structure is elaborated in Chapter 4.

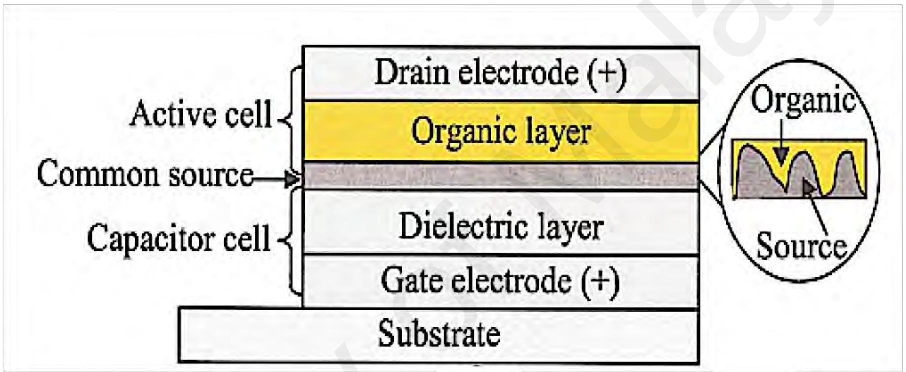

Figure 2.10: Schematic diagram of device structure proposed by Ma & Yang (2004)

2.4.2 Organic semiconductor materials-based optical applications

Several types of structures do exist in the fabrication of OPVs and OPDs, such as single layer, bulk heterojunction (BHJ) layer, ternary heterojunction, as well as inverted and tandem structures. Their variety is meant to enhance efficiency and stability. Primarily, this present study focused on the BHJ structure to study the photovoltaic effect of VTP-based optical devices. The benefits of utilizing the BHJ structure are the ability to fine tune the optical properties of the blend film and the ease of fabrication process (Roncali, 2009). A simple mechanism of OPVs and OPDs is based on the active layer of a single material. Singlet excitons are a strong coulomb-bound electron hole pairs created by absorption of light. These excitons have to be split to generate photocurrent. This process has to overcome the binding energy by either hopping on the thermal energy, or dissociating the excitons at the contacts (Bagher, 2014).

The BHJ structure is composed of donor (D) and acceptor (A) materials, which are blended together. The working principle of BHJ structure is discussed step-by-step, starting from light absorption, exciton generation, exciton diffusion and dissociation, until the transport of charge carrier with collection at the electrodes. Finally, the key performances of OPVs and OPDs are described in the final paragraph of this section.

i. **Photon absorption and exciton generation**. The excitation of an electron in an organic semiconductor is analogous, when compared to exciting an electron from valence to conduction bands in inorganic semiconductor. The electron in organic semiconductor is excited from HOMO to LUMO level upon photon absorption. A strong Coulombic attraction exists between the electron-hole pair due to low dielectric constant, localized electron, and hole wave functions in organic semiconductors. The electron-hole pair bond is called an exciton (Choy, 2012). The electron in HOMO level excites to the LUMO level upon receiving sufficient energy from the photon and leaving behind a hole. At this point, the electron still cannot move freely in the LUMO level as it is still bound to exciton. This process continues until the next stage, where the exciton is diffused at the donor/acceptor (D/A) interface prior to dissociation.

ii. **Exciton diffusion and dissociation.** Diffusion refers to a process where the excitation energy is transferred at lower energy sites. The distance that excitons can migrate towards D/A heterojunction is very short (a few tens of nanometres) and this is called exciton diffusion length (Kietzke, 2007). Hence, to ascertain the occurrence of dissociation, the exciton must be formed just within the interface of the diffusion length, or else it will decay back to its ground state. Next, the photocurrent generation takes place during the exciton dissociation process at the junction between D/A interface, wherein charge carriers formed upon illumination are separated via hopping mechanism, and are, finally, collected at the electrodes. The electron-hole pairs that form a charge pair after dissociation, known as a geminate pair, is still Coulomb bound and only can be separated by an internal field (Choy, 2012).

iii. **Carrier transport.** The geminate pairs formed after the exciton dissociation process move to their respective electrodes within their lifetime. The holes and electrons carriers travel to anode and cathode, respectively, wherein the main driving forces that are responsible for these transports are drift and diffusion currents (Koster et al., 2005). Drift current refers to the transport of charge carrier via potential gradient by means of the electrodes selection in a solar cell. Due to the difference in high work-function anode and low work-function cathode, a built-in electric field is generated within the device that determines the open circuit voltage (V_{OC}) of the cell. This internal electric field is modified and the drift current changes upon presence of supply from the external bias. With the existence of internal electric field, the carriers are drifted towards their respective electrodes for collection. Meanwhile, diffusion current refers to diffusion of charge carriers along concentration gradient in a solar cell. The charge carriers electron and holes are concentrated around the heterojunction as the geminate pairs are generated around the device heterojunction. The carriers diffuse along the concentration gradient, aside from heterojunction, to generate diffusion current. When the applied bias modifies the internal electric field to be close to zero, the device is dominated by diffusion current; and when the internal electric field is large, the mechanism is governed by drift current (Choy, 2012).

iv. **Charge collection at electrodes.** Extraction of charges at the electrodes is the last stage in the photocurrent generation process in OPV devices. The potential barrier at the active layer/electrode interfaces has to be minimized to attain exceptional efficiency in OPV devices. The contacts are usually in ohmic state when the donor HOMO is expected to match the work function of the anode, while the acceptor LUMO is ideally expected to match the work function of cathode (Brabec et al., 2001).

v. **Performance characteristics of OPVs.** The performance characteristics that govern the operation of solar cells are determined by its ability to yield output power based on the application of input power gained from the light. The maximum power output is determined by the magnitude of the maximum products of J and V. Parameters V_{oc}, short-circuit current density (J_{sc}), Fill Factor (FF), and power input density, P_{in} are used to evaluate the power conversion efficiency (PCE) of solar cell performance, as detailed in this section. Figure 2.11 portrays a typical current density-voltage (J-V) curve for a solar cell, inclusive of several critical parameters that determine the PCE of an OPV.

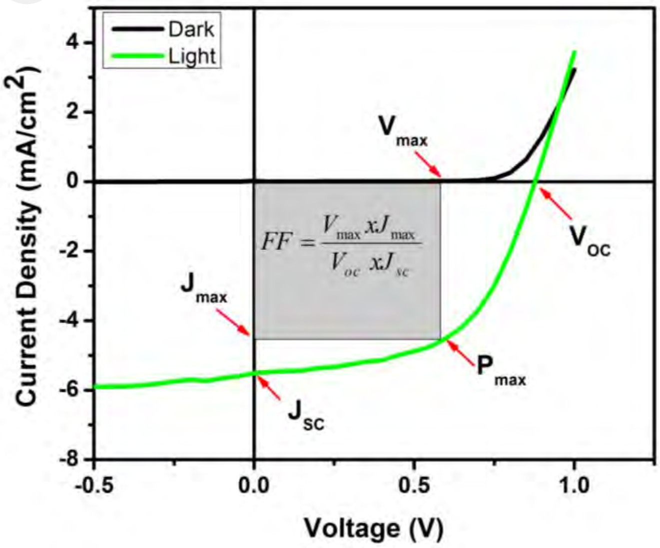

Figure 2.11: Typical J-V curves of an OPV

The description of each of the parameter is presented as below.

a) *Short circuit current density (J_{sc}).* The J_{sc} is defined as the maximum photocurrent density generated at which the external applied potential is zero (Padilla et al., 2014). This value signifies the onset of power generation although no power is produced at this point. It represents the number of charge carriers generated and subsequently collected at the respective electrodes at zero-applied bias (Choy, 2012). Technically, the J_{sc} is a negative number; while conventionally, its magnitude is treated as a positive number. Simply put, a higher J_{sc} is required to determine higher efficiency.

b) *Open circuit voltage (V_{oc}).* The V_{oc} is the voltage at zero current density output. It relies on the work function of varied metal contacts. The ohmic contact between two electrodes makes V_{oc} rely on HOMO-LUMO variance between donor and acceptor (Choy, 2012).

c) *Fill factor (FF).* The *FF* elucidates the shape of *J-V* curve, which is defined as follows:

$$FF = \frac{J_{max} V_{max}}{J_{sc} V_{oc}} \tag{2.1}$$

where J_{max} and V_{max} are current density and voltage at maximum output power, respectively. Based on the equation above, the *FF* refers to the ratio of maximum power output point and maximum attainable power output, such as the products of J_{sc} and V_{oc}.

d) *Power conversion efficiency (PCE).* The PCE, which is the final parameter that dictates the efficiency of solar cells, is calculated using the following equation:

$$PCE = \frac{V_{oc} J_{sc}\, FF}{P_{in}} \tag{2.2}$$

The *I-V* characteristics of the photodetector resemble the electrical characteristics of the conventional rectifying diode, thus it is occasionally described as photodiode. The overall mechanism of OPDs reflects the mechanism of an OPV, inclusive of the following four steps: 1) light absorption that generates exciton, 2) exciton diffusion at D/A heterojunction, 3) exciton dissociation at heterojunction site to form geminate pairs, and 4) charge carriers transported to respective electrodes. On the contrary to solar cell, photodetector operates with external potential bias.

The standard electrical performance of OPDs is evaluated by measuring the reverse biased *I-V* as a function of varied illumination intensities. Figure 2.12 illustrates the typical *I-V* characteristics of a photodiode in forward and reverse bias conditions. Based on Figure 2.12, slight magnitude of dark current, I_D, flows through the photodiode in dark condition (ϕ = 0). With increment of power density of light (ϕ), the photocurrent value increases, and this depicts the basis of photodetection mechanism.

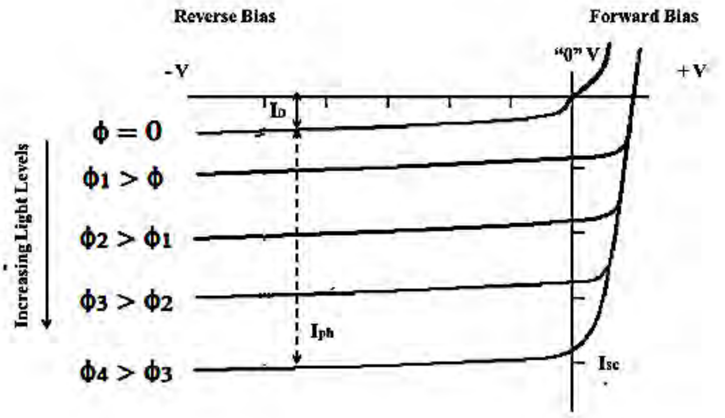

Figure 2.12: Typical electrical characteristics of a photodetector (Yang & Ma, 2019)

i. Performance characteristics of organic photodetector.

a) *Responsivity.* The responsivity "*R*" is a significant parameter for photodetector and it is defined as the ratio of output current density to incident light power (Karimov et al., 2015). It can be calculated based on the following equation:

$$R = \frac{J_{ph}}{P_{in}} \tag{2.3}$$

Where J_{ph} and P_{in} refer to photocurrent density and incident optical power, respectively. The value of responsivity indicates how efficiently a photodetector can convert incident light photon to current output.

b) *Spectral response*. Spectral response assesses the value of photocurrent by a given level of incident light that varies with wavelength. Spectral response is linked with the frequency bandwidth of the photodetector, mainly because the photodetector is sensitive to light in certain frequency or wavelength.

c) *Response recovery time.* Dynamic response and recovery of the photodetector reflect the time taken by a photodetector to reach an output signal from 10% to 90% of its amplitude, and to drop from 90% to 10%, respectively. In an ideal photodetector device, the response and recovery time should be rapid to adhere to the input optical signal. The magnitude of recovery time heavily depends on the applied input bias.

d) *Photo to dark current ratio (I_{ph}/I_d).* The I_{ph} value refers to photocurrent that originates from continuous generation and extraction of free charge carriers upon exposure of photodetector to illumination. The I_d value reflects the dark current that flows under dark condition. High I_{ph}/I_d can effectively minimize noise (Tzeng et al., 2010).

e) *Incident photon to electron conversion efficiency (IPCE).* The IPCE is similar to external quantum efficiency (EQE), as it corresponds to the percentage of incident photons that are converted to carriers, and finally, collected at the electrodes under short circuit conditions (Choy, 2012).

2.4.3 Organic semiconductor materials-based organic humidity sensor application

The fundamental mechanism of humidity sensor device takes place upon exposure to high humidity setting at the opening capillary pores of the sensing layer (Hong-Tao et al., 1989). The water absorption ability heavily relies on dimensions, density, and size of the pores (Banerjee & Sengupta, 2002; Korotcenkov, 2016). At the initial phase, when the sensing films are exposed to humidity, the water vapor molecules that condensed on the surface are chemically absorbed (chemisorption). This chemisorption reaction is accompanied with dissociative process of vapor molecules to form free-moving hydroxyl groups. These free-moving hydroxyl groups are adsorbed and attached on the metal cations, which is present on the sensing layer. Subsequently, an immobile layer forms as the water vapor molecules continuously accumulate on the surface. The first chemisorbed layer owes its rigidity to double hydrogen bonding and this does not change despite the exposure to humid air. Khanna and Nahar (1986) proposed, at this early mechanism stage, that the electrical conduction is generated by electrons tunnelling, which occurs between the donor water sites (Khanna & Nahar, 1986).

In the second phase, another layer of water vapors is physically adsorbed (physisorption) after completing the chemical chemisorption process in the initial layer. These condensed water vapor molecules enable the proton conduction mechanism inside the waterlogged, wherein proton functions as the dominant carrier. Being called as ionic conductivity, the active reactions between water vapor and sensing surface contribute to the dissociation of condensed H_2O molecules into two ionic elements of hydrogen ions (H^+), and hydroxide ions (OH^-). This enhances the magnitude of dielectric constant and the conductivity of the system, thus decreasing its resistivity (Farahani et al., 2014).

More layers are formed as the amount of water vapors augment at higher humidity level. In this phase, proton (H^+) moves freely owing to the disordered secondary physisorbed hydroxyl multilayer, which offers a significant rise in conductivity. Proton diffusion happens between the nearby OH^- ions, where the discharged H^+ ions will hop between the water molecules as the air receives moisture, thus resulting in the formation of hydronium ions, H_3O^+. This process continues relentlessly as the emerging H_3O^+ ions release protons to combine with adjacent water molecule and generate more H_3O^+ ions. Figure 2.13 displays the proton hopping mechanism pioneered by De Grotthuss (Agmon, 1995).

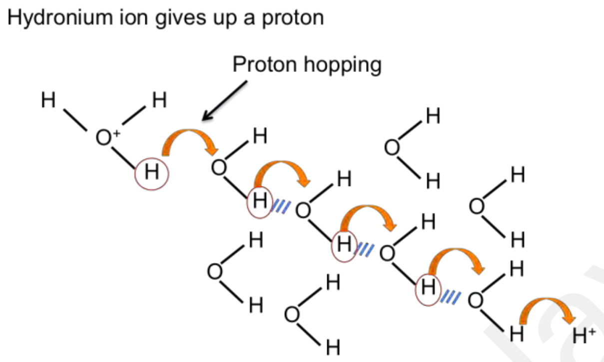

Figure 2.13: Illustration mechanism of proton hopping

Several units of measurement may be employed to measure the amount of water vapors that pervade the surrounding atmosphere. The most ubiquitous measurements are Relative Humidity (RH) and Absolute Humidity (AB). The measurements are selected based on the techniques applied. The former type of measurement is most commonly used compared to the latter one, mainly due to its simplicity and cost efficiency. The RH can be expressed as in Equation 2.4:

$$RH\% = \frac{P_V}{P_S} \times 100 \tag{2.4}$$

where, P_V refers to measured partial pressure of vapor in air, and P_S is saturated vapor pressure at certain temperature. Simply put, RH is the ratio of vapor in the surrounding to maximum content pressure of air, which can be held at a specific temperature. The relative measurement is attributed to its dependency on magnitude, such as temperature. The parameters used to assess the performance of humidity sensors include sensitivity, hysteresis, as well as response and recovery time, as described in the following:

a) *Sensitivity.* Sensitivity is the most prominent parameter to assess the performance of organic humidity sensor. The sensitivity of the proposed sensor can be determined via Equation 2.5 (Al-Ta'ii et al., 2016):

$$Sensitivity, S = \frac{(C_{max} - C_{min})}{(RH_{max} - RH_{min})} \times 100\% \qquad (2.5)$$

C_{max} and C_{min} refer to maximum and minimum capacitance, respectively, whereas RH_{max} and RH_{min} stand for maximum and minimum relative humidity, respectively.

b) *Hysteresis.* Hysteresis is a common issue when measuring humidity sensor, which is a major source of errors due to pore size and geometry, as well as dielectric sensing layer thickness (Islam et al., 2014). It refers to the ability of the devices not to return to their original position despite measuring a change (Sayyad et al., 2010). The hysteresis effect is defined as the percentage of deviation in the measured capacitance during absorption cycle, $C_{adsorption}$, and from that during desorption cycle, $C_{desorption}$. The hysteresis gap is measured by using the following equation (Azmer et al., 2016):

$$Hysteresis, H = average \left[\frac{C_{desorption} - C_{adsorption}}{C_{adsorption}}\right] \times 100\% \qquad (2.6)$$

c) *Response and recovery time.* Response and recovery time are vital to assess the sensing performance of organic humidity sensor. Response time (adsorption) and recovery time (desorption) are described as the time taken for a sensor to reach

90% and 10%, respectively, of the total change of their output capacitance (Morris & Iniewski, 2017).

2.5 Summary

This chapter presents the general review regarding organic semiconductor materials. The MPc and its derivatives, which are grouped under organic molecular materials, are discussed in detail. Several studies have investigated MPc, but in narrowing down the list, VOPcPhO has been given focus due to its resemblance with molecular structure of VTP. Hitherto, only a handful of studies have looked into the physical properties of VTP. The search of a new organic material, thus, is essential to enhance the performance of organic semiconductor devices in market. Hence, to bridge the literature gap, this present study evaluated the characteristics of VTP in an in-depth manner, and subsequently, applied the VTP as the active layer in fabricating electronics, optical, and organic humidity sensor devices. The assessments conducted for each device performance and its characteristics are elaborated in Chapters 4, 5, and 6.

CHAPTER 3: MATERIALS AND METHODS

3.1 Overview

In this chapter, the processes involved in the characterization and fabrication of VTP thin films and VTP-based devices are presented. The initial part of this chapter describes the materials and methods employed in the fabrication process, inclusive of substrates cleaning, solution preparations, and deposition techniques, such as spin coating and thermal evaporation. Brief explanation on thin film characterization, including surface profilometer, cyclic voltammetry (CV), UV-Vis spectrometer, photoluminescence spectroscopy (PL), Raman spectroscopy, x-ray photoelectron spectroscopy, and wettability of the VTP thin film, are outlined in this chapter. The fabrication of VTP-based electronics, optical, and humidity sensor devices are described in the end of this chapter.

3.2 Materials

3.2.1 Vanadyl 3,10,17,24-tetra-tert-butyl-1,8,15,22-tetrakis(dimethylamino)-29H,31H-phthalocyanine (VTP)

The VTP refers to a small molecule *p*-type semiconducting material that derive from MPc derivative. The VTP was purchased from Sigma Aldrich in powder form, which displayed a light purple shade when in thin film form and a molecular weight of 976.16 g/mole. The VTP was not utilized as the organic layer in any device fabrication. The addition of certain attachment on the macro-ring site of VTP exhibited significant variances in its stability and photo absorption spectra, which led to possible applications in optoelectronics appliances. The VTP served as the main material in this study to assess its properties and performance in OFETs, OPVs, OPD, and organic humidity sensors. Figure 3.1 illustrates the molecular structure of VTP.

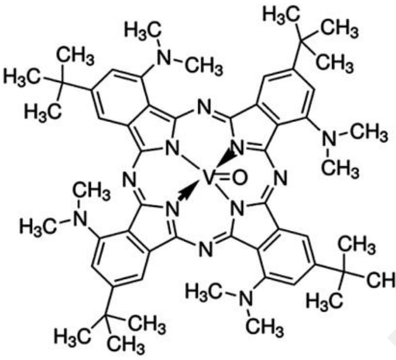

Figure 3.1: Molecular structure of VTP (Roslan et al., 2018)

3.2.2 [6,6]-phenyl C71 butyric acid methyl ester ($PC_{71}BM$)

$PC_{71}BM$ is a well-known polymer that originates from fullerene group and it has been widely reported in device fabrication of OPVs (Srinivasan et al., 2015). In this study, 99% pure $PC_{71}BM$ with empirical formula ($C_{82}H_{14}O_2$) was purchased from Sigma Aldrich, USA. $PC_{71}BM$ is a fullerene derivative of C70 buckyball, which possesses a molecular weight of 1030.93 g/mole and its powder form is black. It has been reported to display main peak absorption between 450 and 500 nm with exceptional electron mobility at 1×10^{-3} cm^2 V^{-1} s^{-1} (Bakar et al., 2015; Ebenhoch et al., 2015). Figure 3.2 portrays the molecular structure of $PC_{71}BM$.

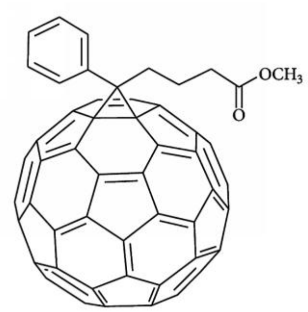

Figure 3.2: Molecular structure of $PC_{71}BM$ (Ochiai et al., 2012)

The application of $PC_{71}BM$ is indeed promising due to its excellent solubility in commonly available organic solvents, and its superior capability in transporting electron (Murugesan et al., 2015). Turning to this study, $PC_{71}BM$ was applied as an n-type electron donor to optimize the performance of OPVs and OPDs by fabricating the BHJ of VTP and $PC_{71}BM$.

3.2.3 PEDOT:PSS

The Poly(3,4-ethylenedioxythiophene):poly(styrene sulfonate) (PEDOT:PSS) thin film in a device structure serves as a hole injection layer (HIL) for anode, primarily due to its virtue of high work function, high optical transmittance in the visible region, moderate thermal stability, and exceptional hole transport (Xu et al., 2017). It also has a smooth morphology with high conductivity that ascertains efficient transport of hole collection at ITO anode electrode (Zhang et al., 2004). In this present study, aqueous dispersion of Heraeus Clevios PH1000 PEDOT:PSS was employed with conductivity of 900-1000 S/cm. In order to achieve a uniform and smooth morphology of buffer layer, the PEDOT:PSS aqueous dispersion was filtered by using a commercially available nylon (0.45 μm) prior to the spin coating process. This organic conducting polymer material was applied to fabricate OPVs and OPDs. Figure 3.3 illustrates the molecular structure of PEDOT:PSS.

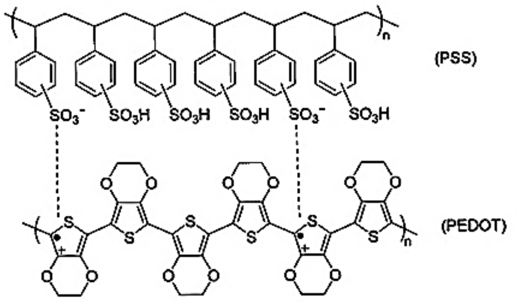

Figure 3.3: Chemical structure of PEDOT:PSS

3.2.4 Silver nanowires (AgNWs)

Silver nanowires were employed as the source electrode for the fabrication of VOFETs. A key aspect of the VOFETs is that the source electrode is sandwiched between capacitor and diode. In order to permit such condition, the source electrode has to be transparent to DC vertical gate electric field so that it can influence the channel region (Ben-Sasson et al., 2015). In this study, AgNWs with a concentration of 5 mg/ml in isopropanol (IPA) was purchased form Novarials Corporation and used without further purification. Its value of sheet resistivity, R_{sheet}, which was measured by four-point probe, was 78.68 Ω/sq.

3.2.5 ITO and Aluminum Electrode

The selection of electrodes for the fabrication of organic semiconductor devices is significant. The work function of metallic electrode and the HOMO-LUMO energy levels of organic semiconductor materials determine if the metal-semiconductor interface is of rectifying or ohmic type. Aluminum (Al) was purchased from Sigma Aldrich. It is graded as 99.999% metal in the form of 1 m length of wire. In this study, Al with a work function of 4.3 eV was applied as electrode for OFETs, OPVs, OPDs, and organic humidity sensors. Indium tin oxide (ITO) coated glass substrates with a work function of 4.7 eV (~20 Ω/sq. sheet resistance) was utilized as the anode electrode for OPVs and OPDs, mainly due to its high transparency in visible spectrum and high electrical conductivity. The ITO was also employed to fabricate OFETs as gate electrode.

3.2.6 Poly[(vinylidenefluoride-co-trifluoroethylene)] (PVDF-TrFe)

PVDF-TrFe was purchased from Kureha, Japan. It is a widely known polymer that displays ferroelectric behavior and it can be used as a dielectric later in OFETs (Nguyen & Lee, 2006; Yildirim et al., 2007). Figure 3.4 portrays the molecular structure of PVDF-TrFE (Wan & Bowen, 2017). PVDF-TrFE is a good dielectric polymer with a dielectric constant that ranges between 8 and 11 at room temperature (Mao et al., 2011). A prior study reported that the PVDF-TrFE consisted of β-phase, which is beneficial when used as a dielectric in a transistor, where it can assist in tunnelling the charge carriers through it to the next layer (Hu et al., 2009).

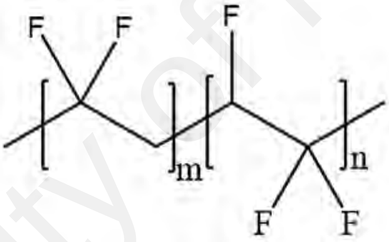

Figure 3.4: Molecular structure of PVDF-TrFE

3.3 Experimental procedure

3.3.1 Substrate cleaning and solution preparation procedure

Two types of substrates were applied throughout this study; glass and ITO-coated glass substrates. Glass substrate was employed for materials characterization and fabrication of organic humidity sensor. The substrate cleaning procedure is a crucial part that discards contamination and forms a homogenous thin film deposited on the substrate. For characterization of materials, the glass slides were cut into 1 cm × 1 cm;

while for fabrication of organic humidity sensors, the glass slides were cut into a fixed dimension of 2.5 cm x 2.5 cm prior to cleaning process. The glass substrates were cleaned thoroughly by sequentially sonicating them for 10 min in soap water, acetone, ethanol, and de-ionized water, accordingly. After that, the glass substrates were dried in a dust-free environment by passing nitrogen onto their surfaces.

The ITO-coated glass substrate was applied for fabrication of optical and electronics devices due to its high electrical conductivity, optical transparency, and easy for deposition as a thin film. The cleaning processes for ITO-coated glass substrates are similar for glass substrates, except that IPA was applied instead of ethanol. The pre-patterned ITO-coated glass substrates were purchased from Ossila, which simultaneously allowed six devices to be fabricated at a time. Figure 3.5 illustrates the substrate pattern that formed 0.045 cm^2 active area for each device.

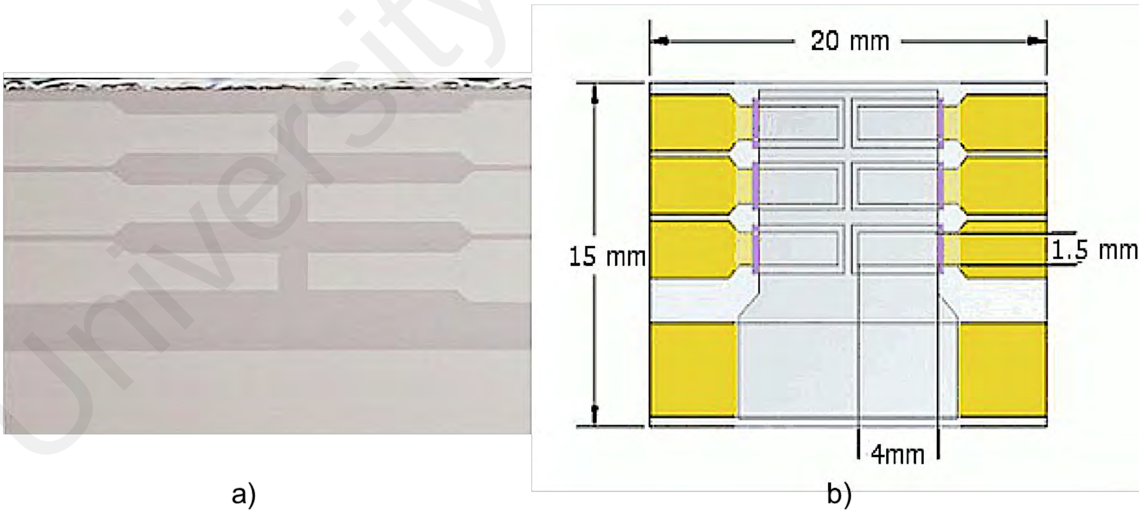

a) b)

Figure 3.5: a) Image of pre-pattered ITO, and b) geometry design of pre-patterned ITO coated glass substrate

As for solution preparation, the VTP served as the focus material that was used throughout this study. For characterization and fabrication purposes, 10 mg of VTP was dissolved in 1 ml of chloroform (with 99.99% purity) to prepare 10 mg/ml solution concentration. This concentration was maintained throughout this study to fabricate the electronics, optical, and organic humidity sensors devices. For the optimization process, new materials were incorporated to fabricate OPVs in order to form BHJ blended system. The 10 mg/ml of [6,6]-phenyl C71 butyric acid methyl ester ($PC_{71}BM$) was prepared in isolation. $PC_{71}BM$ was mixed with VTP matrix at a certain volume ratio to generate a BHJ blended system. Table 3.1 presents the related details.

The prepared solutions were stirred at 600 rpm stirring speed in a glove box using magnetic stirrer for at least an hour to ensure that the materials are dissolved completely. Prior to thin film deposition, the prepared solutions were filtered by using a disposable PTFE filter (the size of filtration membrane was ~0.25 micrometre).

Table 3.1: Solution preparations for VTP-based organic semiconductor device applications

Materials / volume ratio	**Concentration**	**Volume ratio**	**Organic electronic device applications**
VTP	10 mg/ml	-	1. Electronics devices (LOFETs and VOFETs) 2. Optical devices (OPVs and photodetector) 3. Organic humidity sensor applications
$VTP:PC_{71}BM$		1:1 1:2 1:4	Optical devices (OPVs and photodetector)

3.3.2 Thin film preparation

Several methods have been commonly used for thin film deposition, such as dip-coating, drop casting, and spin coating. Both dip-coating and drop casting are inappropriate for this study due to the demand of huge amount of solution in depositing a thin film, the production of a thick film that is above the sought nanoscale range, and the challenge in controlling their thicknesses. Hence, the spin coating technique was adopted in this study for deposition of thin films. This technique is beneficial as it only requires a small amount of solution and easy to control the thickness of thin film within a nanoscale range. Figure 3.6 displays the spin coater from Laurell (model WS-650MZ-23NPP) that was used throughout this study.

Figure 3.6: Laurell model (WS-650MZ-23NPP) spin coater

A few drops of solution were injected on top of a cleaned substrate prior to spinning at a desired spin speed. The thickness of the spin-coated film is inversely proportional to the spin speed. Upon increasing the spin speed, the film thickness decreases, and vice versa (Jayamurugan et al., 2015).

3.3.3 Physical Vapour Deposition (PVD)

A thermal evaporator was applied to deposit the top Al contact on the active layer via High Vacuum Thermal Deposition System that was placed in a glove box, as illustrated in Figure 3.7. The evaporator evaporates the metal Al placed on the tungsten boat with the presence of large current (~80 A). The metal that melts will eventually evaporate on the target substrate above the source and produce a film. In order to deposit < 100 nm top contact of Al, the process was performed in a high vacuum environment with controlled evaporation rate.

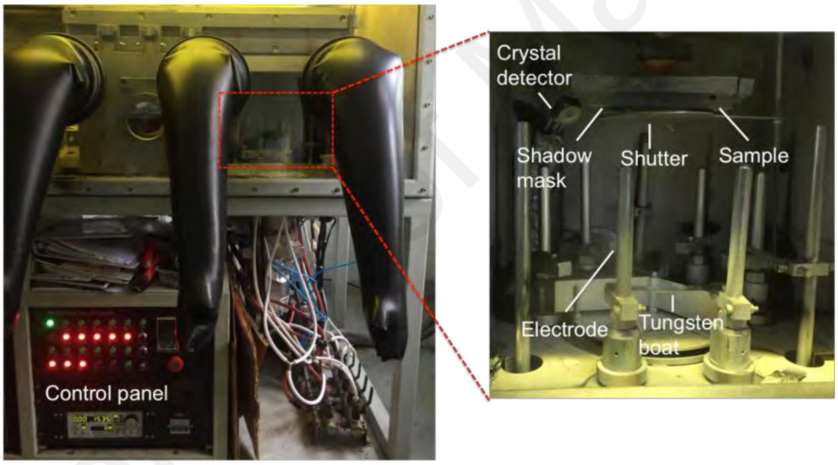

Figure 3.7: High Vacuum Thermal Evaporation System

A shadow mask is required to deposit the aluminum electrode, either in square or round shape, depending on the device pattern. During the deposition process, it is typical to use the square shadow mask for pre-patterned ITO-coated glass substrate to generate an active area of 4.5 mm^2 (3.0 mm × 1.5 mm). The round shape shadow mask is used for plain ITO substrate (without patterned) to produce an active area of 3.03 mm^2 (radius 1.5 mm). In this study, both OPV and OPD devices used the same square shadow mask, OFET devices applied round shape mask, and organic humidity sensor used a shadow mask with copper wire wrapped around the glass substrate.

Figure 3.8 portrays a schematic diagram of a thermal evaporator. Finally, the devices were encapsulated to prevent reactions from external elements, such as oxygen that can degrade the active material, causes oxidation, and deteriorates the device performance exponentially. The encapsulation helps to prolong the device performance and stability for an extended period.

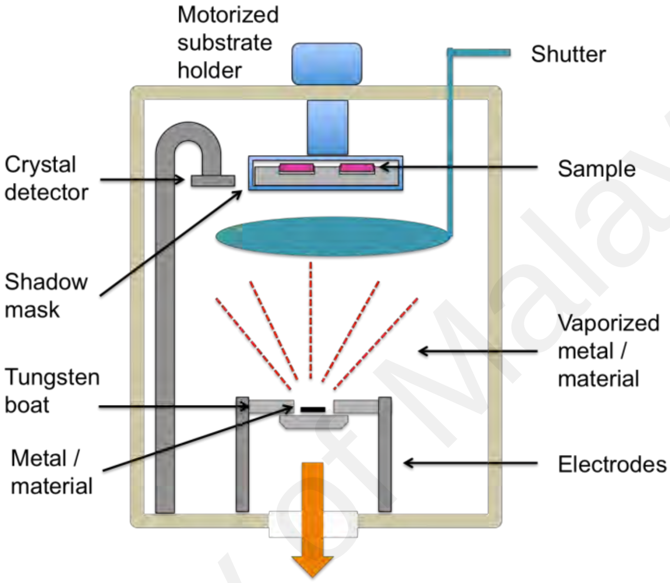

Figure 3.8: Schematic diagram of physical vapour deposition

3.4 Thin film characterization

This section summarizes a series of characterization methods of thin film. It is divided into six sections, namely physical, structural, morphological, chemical, optical, and electrical characterizations. Surface profilometer and wettability tests were performed to characterize the physical properties of the thin film. Raman and X-ray photoelectron spectroscopies were utilized to assess the structural and chemical bonding properties of the thin film, respectively. Atomic force microscopy (AFM) was employed to characterize the aspect of morphology, while PL and UV-Vis spectroscopy were applied to evaluate the optical properties. Finally, CV as electrical characterization was performed to examine the HOMO-LUMO of the thin film.

3.4.1 Physical characterization

*(a) **Surface profilometer***

Surface profile and topography of the material had been characterized by using a KLA Tencor Surface Profilometer (model P-6 Stylus Profiler). The resolution of the surface roughness could be up to 0.5 Å. Such profiler functions based on contact mode, where the stylus (probe) is used to detect the surface and move along the sample surface in vertical direction to determine the surface height and to measure the minor changes on the surface as a function of position with a scan length up to 150 nm, vertical (height) range of 327 µm, and stylus force of 0.3-5.0 mg. The stylus tip of this profiler is made of diamond (2 µm) and uses a cantilever system with 60° radius to ensure that the tip is at a constant force during the scanning process.

Apart from detecting surface roughness at a minimum scale, the surface profilometer measures the thickness of a thin film. In order to measure the sample thickness, a thin film with linear scratching is required to generate a trace of step between film sample and substrate surface. Next, the stylus tip is dragged perpendicularly across the scratched trace to distinguish the film level from the substrates level. The distance between these surface levels determines the thickness of the thin film. Figure 3.9 illustrates the surface profilometer applied for characterization in this study. The sample preparation for surface profilometer was performed by spin coating the organic layer on top of a cleaned glass.

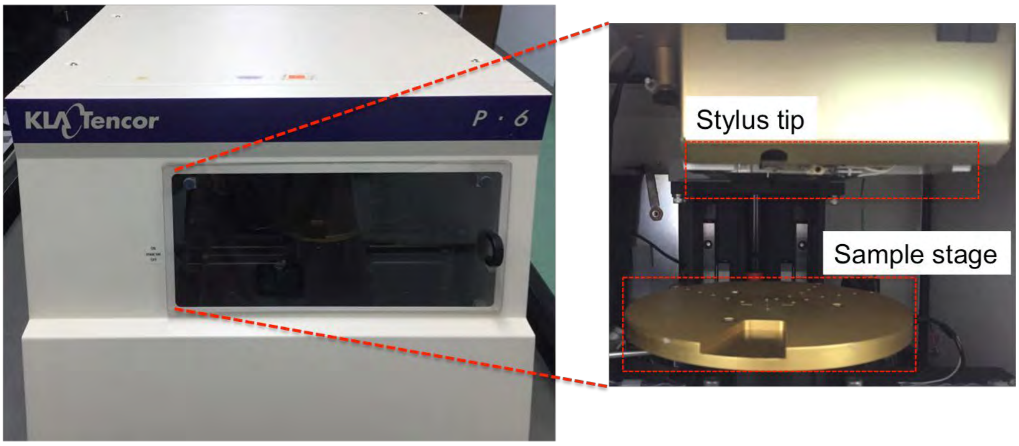

Figure 3.9: Image of surface profiler meter KLA tencor (P-6)

(b) ***Contact angle measurement***

The easiest way to measure the contact angle of sessile drop is by applying the contact angle goniometer technique, in which a direct measurement is performed visually to determine the contact angle directly to the drop surface at the point of contact (Dimitrov et al., 1991). The measurements were conducted at room temperature. Distilled water was utilized as the droplet liquid on top of the VTP thin film, which was placed on the sample stage as the solid surface. The sample was prepared by spin coating the VTP on top of a cleaned glass substrate. The film was placed on a horizontal stage and a 100 μl syringe capacity was positioned at the centre and above the sample surface with background light behind the droplet to improve the image of water droplet. The syringe was connected to the micromanipulator. The function of micomanipulator is to adjust the position of the syringe needle tip carefully above the film. The syringe tip was adjusted until it was several micrometres away from the sample thin film surface in order to minimize the gravitational effect upon release of droplet. The spreading process upon release of 1 μl water droplet was recorded using a computer-connected CCD camera.

In this study, the wetting behavior of the VTP thin films was examined by measuring the contact angle using a computer installed with OneAttension software. Figure 3.10 illustrates the measurement set up for contact angle measurement.

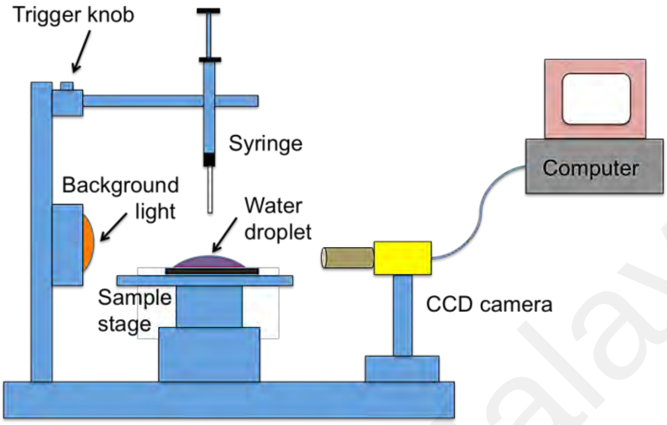

Figure 3.10: Schematic diagram of contact angle measurement set up

3.4.2 Structural characterization

*(a) **Raman spectroscopy***

The incident light (photon) that propagates through a material scatters into two scattering types, namely Rayleigh scattering (elastic) and Raman scattering (inelastic). In Rayleigh scattering, the incident photon that propagates into a material emits with the same energy and frequency, but with varied propagation directions. Such scattering does not alter the electronic state of the material. As for Raman scattering, the photon energy that passes through a material is absorbed by the material (molecule) and excites to a virtual electronic level. The molecules relax at a ground state to either a lower-energy level (Stokes) or higher-energy level (Anti-stokes) relative to its original state by emitting another photon. The emitted photon has lower energy than the incident photon. In Raman spectroscopy, monochromatic light from a laser (in UV/visible/NIR range) is applied to interact with the molecular vibration system, whereby the shift in laser photon offers information regarding the system vibrational modes (Frost, 2006).

In this study, Raman spectroscopy with 512 nm excitation wavelength was applied to assess the molecular structure and the bonding properties of VTP thin film and VTP:$PC_{71}BM$. Figure 3.11 portrays an image of Renishaw inVia Raman microscope. The sample preparation for Raman spectroscopy incorporated spin coating the organic layer on top of a cleaned glass.

Figure 3.11: Image of Renishaw inVia Raman microscope

3.4.3 Chemical characterization

(a) X-Ray Photoelectron Spectroscopy (XPS)

The XPS was applied to determine the chemical bonding of the VTP material. The samples meant for such characterization must be placed in ultra-high vacuum (UHV) setting with low pressure below 2.7×10^{-8} Pa. Such environment minimizes any contamination on the sample by a gas molecule. High energy x-rays (100-2000 eV) allow electrons from the core level to be injected into the sample. The thin film surface is illuminated by UV radiation or x-ray photon energy. The core electron of the atoms is knocked out from the sample surface due to the illumination of high-energy x-ray photons. The ejected electron, known as photoelectron, is detected and collected by an electron analyzer that measures its kinetic energy (Geng et al., 2002).

In this study, the elemental composition of VTP thin film was assessed via XPS (PHI Quantera II), along with photoemission spectroscopy (PES) beamline BL3.2 at the Synchrotron Light Research Institute (SLRI) located in Thailand. The sample was prepared by spin coating the VTP layer on top of ITO-coated glass substrate to hinder charging effect. A Thermo VG Scientific CLAM2 electron spectrometer was attached to the PES system and operated at a maximum photon energy of 600 eV with an energy step of 0.1 eV. The retrieved binding energy spectra were calibrated using C 1s energy of 284.6 eV, which had been assigned to the adventitious carbon that exhibited unavoidable presence in all air-exposed materials. Figure 3.12 displays a schematic diagram of basic XPS characterization.

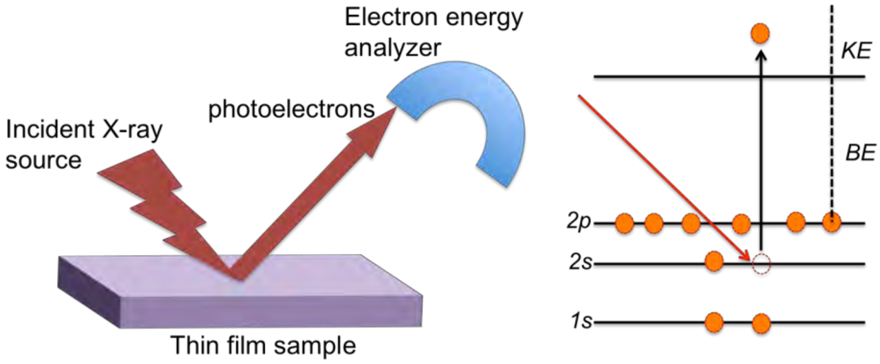

$$KE = hv - BE - \Phi$$

Figure 3.12: a) Schematic diagram of basic XPS operation, and b) principle of photoemission: when an x-ray (red arrow) bombards a sample, some electrons (orange sphere) become sufficiently excited to escape the atom (black arrow)

3.4.4 Morphological characterization

(a) Atomic Force Microscopy (AFM)

Several studies concerning organic film surfaces had used AFM to gain understanding of the morphology of a specific material or blend layer. The surface morphology of a thin film can immensely influence its electronic properties. This refers to one of the main characteristics of an organic semiconductor film. Figure 3.13 illustrates a schematic diagram of a standard AFM instrument. The sample surface is scanned with a sharp silicon tip that is connected to a piezo oscillator. Upon touching the sample surface, the tip interacts with the molecules and the tip becomes deflected. This deflection is determined by the reflection of laser light that is reflected to a fast photo-diode, which is used by a feedback loop to control the movement of piezo scanner that moves the tip. The AFM is operated in tapping mode, wherein small force of interaction serves between tip and sample surface to avoid damaging the organic material. Sample preparation for AFM was executed by spin coating the organic layer on top of a cleaned glass.

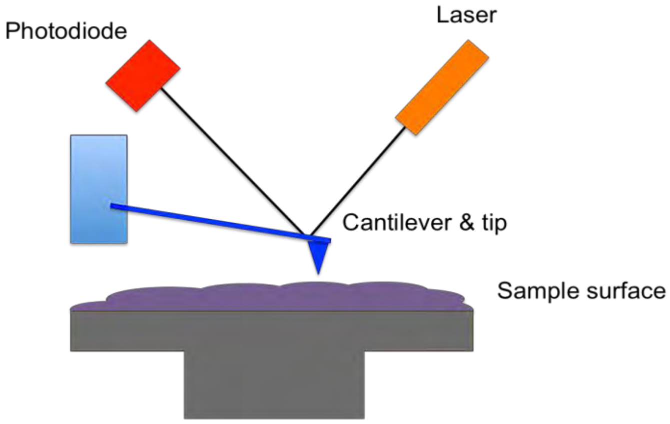

Figure 3.13: Schematic diagram of AFM scanning mechanism

3.4.5 Optical characterization

(a) Ultraviolet/visible/infrared (UV/Vis/NIR) Spectrophotometer

A number of methods are available for electromagnetic radiations to interact with matter. The term 'spectroscopy' refers to the study of interaction between electromagnetic radiations of varied energies and matter, whereby each interaction reveals some properties of the studied matter. A spectrophotometer is an instrument that measures the amount of light in a certain wavelength range upon passing through a medium. The basic concept of this spectrometer is that when light propagates through a material, an interaction occurs with the molecules inside the materials, thus resulting in absorption, transmission, and reflection of light. These interactions happen when the electromagnetic (light) photons are absorbed by the molecules and energetic enough to promote the outer electrons from the HOMO level to the LUMO level of the material, thus creating electronic transitions. Figure 3.14 displays the potential electronic transitions that occur in organic molecules that contain bonded π, σ, and unbonded neutral (n) electrons, namely $\pi - \pi^*, n - \pi^*$, $n - \sigma^*$, and $\sigma - \sigma^*$ transitions, whereby those conjugated (star) contribute to the anti-bonding of respective transition electrons. Of the six transitions outlined, only two higher wavelengths were achieved in the range between 200 and 800 nm spectrum, which is attributable to $n - \pi^*$and $\pi - \pi^*$ transitions found within the UV-visible region. Meanwhile, $n - \sigma^*$ and $\sigma - \sigma^*$ transitions occur in shorter wavelengths ranging below 200 nm.

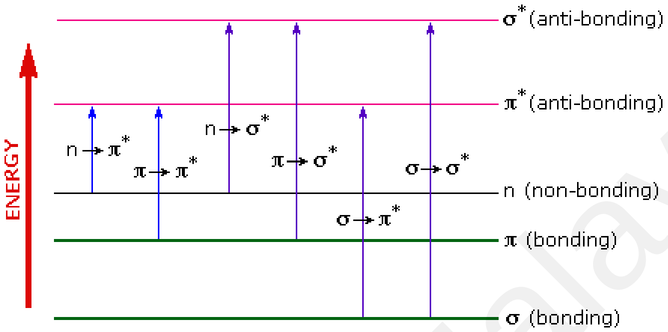

Figure 3.14: Transitions of electrons (Retrieved from: https://www.chemguide.co.uk/analysis/uvvisible/theory.html)

Most organic materials have π-conjugated system with the presence of single and double carbon-carbon bonds. The double bond transitions the π conjugated electron from either π or n electrons. Such transitions can be detected by UV/Vis/NIR spectrophotometer that corresponds to the energy absorbed to promote an electron from low to high energy orbital. Thin film absorption was studied using Perkin Elmer Lambda 750UV/Vis/NIR spectrophotometer that covered wavelengths between 190 and 3300 nm. The UV-Vis resolution for this spectrophotometer ranged from 0.17 to 5.00 nm, while 0.2 to 20.0 nm for NIR resolution. Sample preparation for UV-Vis spectroscopy involved spin coating the organic layer on top of a clean glass.

Figure 3.15 shows an image of UV/visible/NIR spectrophotometer Perkin Elmer model Lambda 750 that has two substrate holders: i) reference for baseline calibration, and ii) sample for optical characterization of thin film sample. For baseline measurement, two uncoated substrates were placed on both holders. Characterization of thin film was conducted after performing the baseline analysis, which is by replacing one of the uncoated substrates with that coated. Light absorption intensity of the thin film was identified based on the uncoated substrate as reference. The light source from UV and NIR derived from deuterium and tungsten lamps.

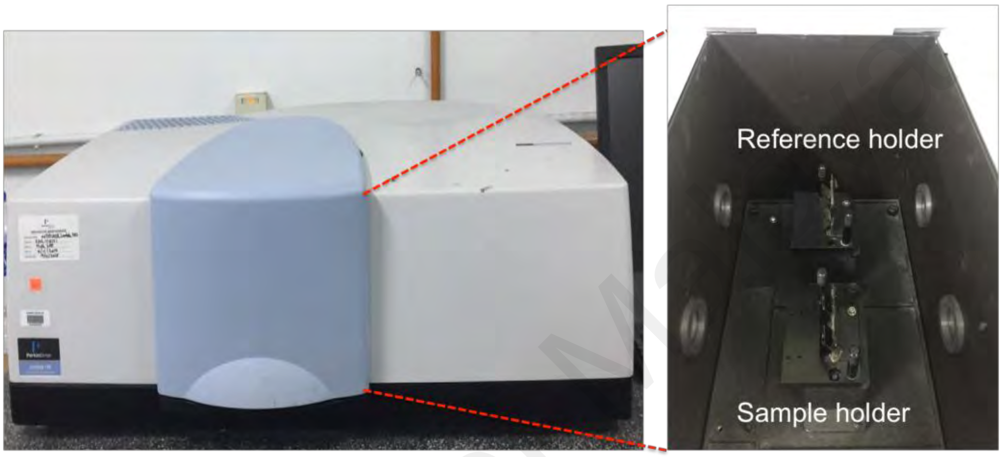

Figure 3.15: UV/visible/NIR spectrophotometer Perkin Elmer model Lambda 750 with enlarged images of reference and sample holders of the spectrophotometer

*(b) **Photoluminescence spectroscopy***

The process of luminescence occurs when radiations or other forms of energy are converted to visible light. Photoluminescence refers to the process that happens in a material when an electron in lower energy level state (HOMO) is excited by incident radiations to a higher energy level state (LUMO), and then, falls back to a HOMO state by emitting photon of lower energy. Such characterization has a significant role in determining the optoelectronic properties of OLED and OSC. The PL measurement in OLED application is required, mainly because higher PL intensity signifies that the material is good to produce light due to the huge number of recombination rate of photo-induced electron-hole pairs. As in the OPVs application, lower intensity of PL is required to generate photocurrent due to less recombination rate (Liqiang et al., 2006). This characterization offers a vivid illustration on electron-hole pair interaction, if they recombine or dissociate under conditions in which energy is emitted in the form of luminescence photon.

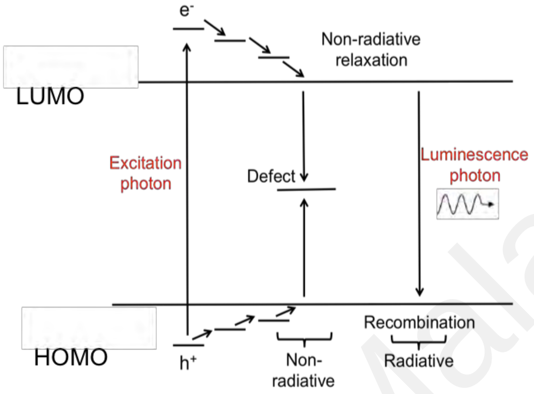

Figure 3.16: Photo-excitation and emission process

Figure 3.17: The PL spectrometer (Horiba LabRAM HR Evolution)

Figure 3.16 portrays the photo-excitation and emission processes that occur when an electron receives sufficient energy to excite and return to the valence band through release of energy. Figure 3.17 shows the PL spectrometer from Horiba LabRAM HR Evolution, which was applied in this study using 325 nm excitation wavelength. The PL measurement included fluorescence, phosphorescence, chemiluminescence, and bioluminescence. The sample for PL spectroscopy was prepared by spin coating the organic layer on top of cleaned glass.

3.4.6 Electrical characterization

(a) *Cyclic voltammetry (CV)*

The CV refers to a convenient method for a broad range of applications. In this study, CV was applied to measure the HOMO and LUMO values of VTP small molecule organic material. Prior to device fabrication of OPVs and OPDs, selection of the most suitable active semiconducting material is crucial, whereby the active region turns into a place for charge generation, separation, and transfer to occur under light illumination. In satisfying the energy requirements for BHJ device architecture, the LUMO level of the acceptor must exceed the donor to allow transfer of electron, whereas the HOMO level for the donor must exceed the acceptor to permit transfer of holes, so as to generate photocurrent (Forrest, 1997; Tang, 1986). In FET devices, the function of electrode materials must suit the HOMO/LUMO of the organic semiconductor layer to ascertain efficient injection of electron/holes into empty HOMO/LUMO levels. Hence, it is critical to identify the energy levels of HOMO and LUMO, as well as the energy band gap, when selecting a new material for the mentioned applications.

In an organic semiconductor, HOMO is described as the energy required to extract an electron from a molecule, wherein oxidation (ox) process occurs. Meanwhile, LUMO is the energy required to inject an electron into a molecule, which is also known as the reduction (red) process (Leonat et al., 2013). The measurement of these processes can be determined via CV technique by measuring the redox potential reduction energy, E_{red}, and oxidation energy, $E_{ox.}$ Ferrocene, in this case, may serve as a standard reference with a value of -4.4 eV to calculate the energy of HOMO and LUMO levels. In this study, the HOMO and LUMO energy levels were determined by using the following empirical equations:

$$E\ (\text{HOMO}) = -e\ [\boldsymbol{E_{ox}^{onset}} + 4.4] \tag{3.1}$$

$$E\ (\text{LUMO}) = -e\ [E_{red}^{onset} + 4.4] \tag{3.2}$$

In CV characterization, the VTP film was prepared on 1 × 3 cm ITO-coated glass via spin coating method. Figure 3.18 portrays the set up that adhered to common electrical connections comprising of a platinum working electrode, a platinum wire counter electrode, and an Ag/AgCl reference electrode. Next, the film was dipped into a mixture of potassium chloride (KCl) electrolyte and 0.1 M ferricyanide electrolyte. Both oxidation and reduction potentials were determined with 5 mV/s scan rate, which was later used to calculate HOMO and LUMO of VTP.

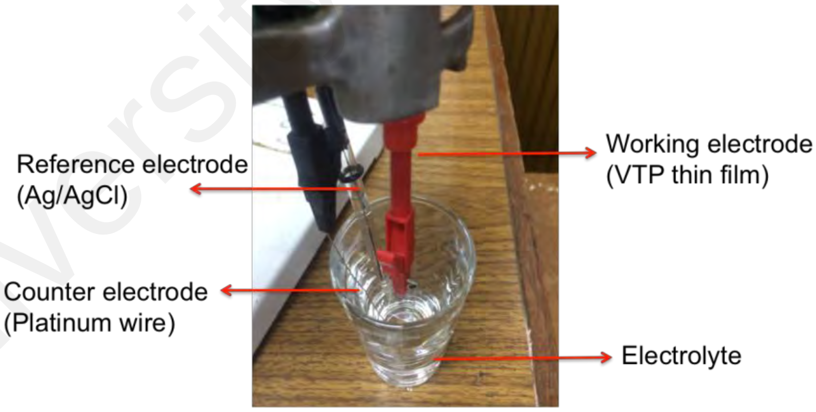

Figure 3.18: Cyclic voltammetry set up

3.5 Measurement of VTP-based organic devices

This section describes the measurement techniques employed to assess the related devices. This section is divided into three sections; *I-V* characterization of (i) transistor application, (ii) optical application, and (iii) humidity sensor application.

3.5.1 *I-V* characterization of OFETs device

A FET refers to a three-terminal device that consists of source (S), drain (D), and gate (G), whereby each terminal is capable of carrying current. The gate terminal regulates current between S-D electrodes by generating electric field and controlling channel formation into the semiconductor layer. The drain terminal is biased with positive or negative applied voltage, whereas the source terminal is grounded. The gate terminal is applied with the same polarity of the applied voltage, but the value of the applied electric field may vary, particularly during the saturation characteristics measurements. Since transistors contain more than two terminals, they need a two-channel Source Measure Unit (SMU) to perform the measurement of FET. Figure 3.19 show the image of a two-channel SMU unit Keithley B2900A source meter, which had been utilized in this work to characterize FET. Figure 3.20 displays the connection of VOFET device.

Figure 3.19: SMU unit Keithley B2900A source meter

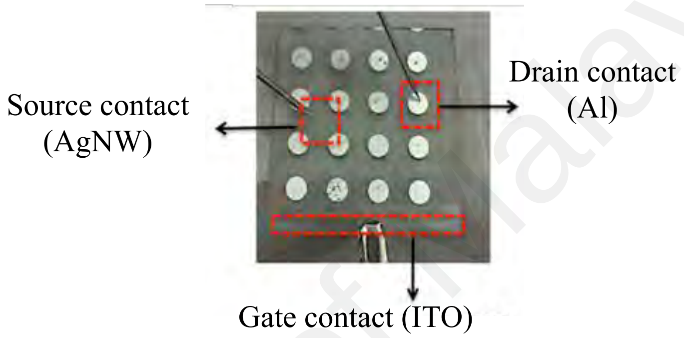

Figure 3.20: Image of VOFET device

3.5.2 *I-V* characterization of optical devices

A diode refer to an electronic device that has two terminals; positive and negative, which allow current to flow in one direction and block it from flowing in the reverse direction. Despite the vast range of diodes available, this study focused on only two types of diodes, namely Schottky transport and photosensitive diodes. The *I-V* characteristics measurement of these fabricated diodes was performed under dark and illumination settings at selected wavelengths.

In dark condition, the measurement is executed in sweep voltage mode, which is suitable for Schottky diode. In illumination condition for photosensitive diodes, the current generated is higher and the modulus value of short circuit current is increased upon exposure to light. All *I-V* measurements for Schottky diodes were performed using computer installed with Keithley SMU unit (see Figure 3.21). As for the measurement of photosensitive diodes, such as OPVs and OPD in this case, the devices were placed under Oriel 67005 solar simulator. Figure 3.22 portrays the measurement set up for solar simulator to characterize both transport and photosensitive diodes.

Figure 3.21: Keithley SMU unit

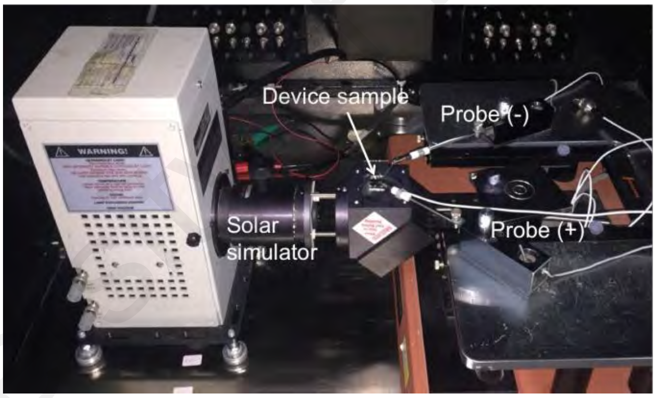

Figure 3.22: Solar simulator measurement setup

3.5.3 *I-V* characterization of organic humidity sensor devices

The organic humidity sensor often is fabricated in a planar structure, whereby the VTP is deposited between electrodes on each side. The fabricated device is directly characterized in custom-made humidity chamber upon completing the fabrication process. The level of RH value within the chamber can be manipulated. Further details on the measurement procedure and the sensing response mechanism for capacitive outputs are presented in Chapter 6. The electrical characterization measurement was conducted under multiple applied frequency AC current input with constant voltage bias of 1 kV. The measurement set up of organic humidity sensors are described in Table 3.2, while the image of experimental set up is illustrated in Figure 3.23.

Table 3.2: Description of measurement set up described in Figure 3.23

Component	**Roles**
Sample holder chamber	To place the sample
Humidifier	To provide the vapour source
Nitrogen gas	To remove the vapour source
Thermohygrometer	The RH indication level
LCR meter	To measure the sensor outputs

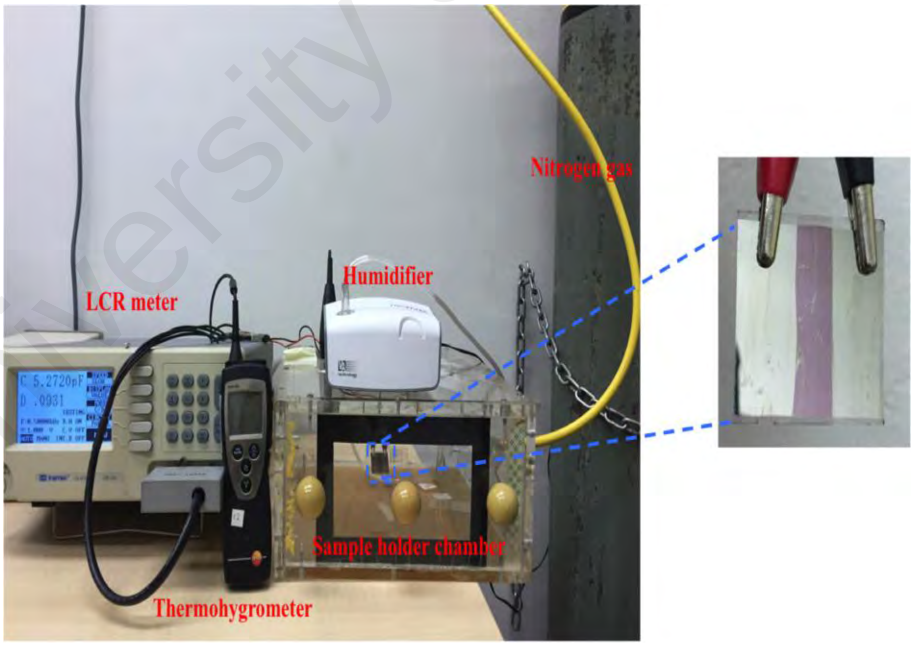

Figure 3.23: Characterization set up of the humidity sensor

3.6 Summary

This chapter presents all the materials and chemicals applied in this study. The characterization of VTP thin films, BHJ blended film, and *I-V* characterization of each device is described accordingly. Finally, based on the properties of optimized thin film characterizations, three organic devices based on VTP were fabricated, namely VTP-based OFET applications, VTP-based optical applications, and VTP-based organic humidity sensor. The fabrication of these devices is elaborated in Chapters 4, 5, and 6, respectively.

CHAPTER 4: VTP-BASED ORGANIC TRANSISTOR DEVICES

4.1 Introduction

This work demonstrates the fabrication of VTP-based organic transistor devices of two architectures; LOFETs, and VOFETs. Prior to fabrication of LOFETs and VOFETs, the basic properties of HOMO and LUMO of VTP were determined via oxidation and reduction potentials using CV. The energy level of VTP was determined via optical absorption spectroscopy, which was analyzed via two methods; absorption wavelength and Tauc plot. Next, the architecture of VTP-based LOFETs was fabricated to serve as a control device. Finally, VOFETs were fabricated, wherein the device thickness was optimized to improve their performances.

4.2 OFETs Technology Development

The emergence of OFETs in the present technology progression has received remarkable attention from both research and industrial sectors, mainly due to their flexibility, physical features, lower production cost, and suitability for application in large area of consumptive productions (Jaisutti et al., 2010). In spite of their impressive features, the use of organic semiconductor in conventional LOFETs seems to exhibit poor electrical performance, for instance, low output current, high operational voltage, and low operational frequency (Kudo et al., 1998). These discrepancies are attributable to low charge carrier mobility in organic semiconductor materials, and the long channel path for the charge carriers to flow from source to drain in LOFETs (Kudo et al., 2001).

In recent times, researchers have made extensive efforts to circumvent the above mentioned shortcomings by fabricating the organic transistors in vertical arrangement (Yu et al., 2016) by employing organic semiconductors, such as MPc derivatives (Kvitschal et al., 2015). The MPc is a promising organic materials with tailored properties and comparable performance to conventional inorganic materials applied in optoelectronic applications (Melville et al., 2015). The MPcs, along with their various substituents on macro-ring and metal derivatives, have garnered much interest in light of electronics and optoelectronics applications due to their charge transport properties, thermal and chemical stability, as well as massive absorption coefficient at Q-band (visible spectral region) (Sakamoto & Ohno, 1997). One well-known MPc that has been employed as an active layer is VOPcPhO, which refers to small molecules *p*-type semiconducting material widely applied in OPVs and OPDs (Abdullah et al., 2012; Zafar et al., 2014). Such organic material has a tendency to have low turn on voltage when fabricated into OFET. As for vanadium phthalocyanine derivative or VTP, it has yet to function as an organic layer in OFET fabrication. The VTP and its derivative (VoPcPhO) differ in terms of their substituents in the macro-ring of Pc. Incorporation of certain attachments to the macro-ring site of VTP exhibits essential variances in its charge transport, absorbance spectra, and ease of synthesis, which suit a range of applications (Ahmad Makinudin & Supangat, 2016; Melville et al., 2015).

The fabrication of VOFET had significantly reduced channel length, wherein the source and gate electrode were separated by few hundreds of nanometre due to the thickness of active organic layer. This, in turn, addressed the drawbacks of the conventional OFETs by producing lower operational voltages and higher output current. The structure of VOFET refers to vertically stacked layer-by-layer with the gate placed at the bottom, followed by dielectric layer, intermediate source electrode, semiconducting channel layer, and top drain electrode. Kudo et al., (2001) reported that the vertical arrangement of FET using CuPc as the active layer benefitted in terms of operational output current at ~2.6×10^{-6} A, along with two orders larger than that of LOFET. Kvitschal et al., (2015) investigated the fabrication of VOFET using an Sn single layer as source grid electrode and CuPc as channel semiconductor. Their research revealed that the VOFET using CuPc as semiconductor material operated at low operational voltage using Sn grid, which signified permeability to the electric field. Halizan et al., (2017) assessed the performance of VOFET, wherein VOPcPhO served as channel semiconductor layer by altering the morphology of dielectric layer. The outcomes indicated the successful fabrication of VOFET device and the enhanced performance of VOPcPhO-based device with porous dielectric, when compared to that with non-porous layer dielectric film.

This study proposes another *p*-type of MPc derivative by studying the performances of the varied architectures of LOFET and VOFET. This study assessed the less-reported MPc that derives from vanadium phthalocynine, which is also known as VTP. To the best of the author’s knowledge, VTP has not been applied in the fabrication of FET so far. The values of HOMO and LUMO of VTP were determined in the initial part of this study. Subsequently, LOFET was fabricated to assess the effect of FET performance on two arrangements. Finally, the optimization of active layer thickness in fabricated VOFET devices was performed.

4.3 Experimental procedure

The ITO-coated glass substrates (~20 Ω/sq sheet resistance) with 2 × 2 cm^2 dimension were thoroughly cleaned by adhering to the cleaning protocol elaborated in Section 3.3.1 of Chapter 3. A 10 mg/ml of active layer solution was prepared by dissolving VTP powder into chloroform and subjected to stirring process for 1 h. The thin film sample was prepared via simple spin coating method at a spin speed of 2000 rpm for 30 s. After that, the thin film was annealed at 100 ºC for 30 min. Next, the absorption spectrum of the film was characterized using PerkinElmer LAMBDA 900 UV-Vis spectrophotometer, which was later applied to estimate the optical energy gap.

The VTP film was prepared on 1 x 3 cm ITO-coated glass via dip-coating method for CV measurement. The set up adhered to the common electrical connection that comprised of a VTP thin film working electrode, a platinum wire counter electrode, and an Ag/AgCl reference electrode. After that, the film was dipped into a mixture of KCl electrolyte and 0.1M ferricyanide electrolyte. The oxidation and reduction potentials were determined via 5 mV/s scan rate, which were later applied to calculate HOMO and LUMO of VTP.

The LOFETs in lateral geometry were fabricated in bottom gate staggered structure configurations, while the layer-by-layer method was employed to fabricate VOFETs. Initially, in fabricating LOFETs and VOFETs, the cleaned ITO-coated glass substrates functioned as gate electrode. The copolymer poly(vinylidene fluoride-trifluoroethylene), or P(VDF-TrFE) 75/25, was purchased from Kureha and used without further purification as the dielectric layer. A 5 wt% of P(VDF-TrFE) solution with dielectric constant of 13 was prepared using methyl ethyl ketone (MEK) as solvent prior to being spin coated onto the ITO substrates (Nguyen & Lee, 2006). Next, 200 nm of PVDF-TrFE thin film, which functioned as dielectric, was prepared via spin coating method with the optimized spin speed of 4000 rpm for 30 s. The samples were kept in the oven overnight at 80 °C to remove residual solvent and they were further annealed at 100 °C to enhance the crystallinity of P(VDF-TrFE) thin films (Mahdi et al., 2014). In particular for fabrication of OFETs, the organic layer with spin speed of 2000 rpm was spin coated on the dielectric layer. Finally, the formation of 100 nm aluminum (Al) top contacts of source (S) and drain (D) of the device was deposited in vacuum condition via thermal evaporation.

As for VOFET fabrication, silver nanowires solution (AgNWs) with 5 mg/ml concentration, which served as source channel, was applied as received from Novarials Corporation. It was spin coated onto ITO/PVDF-TrFE substrate at a constant spin speed of 5000 rpm for 30 s, and later, annealed at 80 °C for 1 h. The length and diameter of the AgNWs were 15 μm and 20 nm, respectively. Next, the VTP thin films were produced by spin coating some drops of 10 mg/ml of VTP solution on top of ITO/PVDF-TrFE/AgNWs. Prior to that, the VTP was dissolved in chloroform solvent and its concentration was kept constant for all devices. Varying the spin coating rate at 500, 2000, and 3000 rpm for 30 s generated varied thicknesses for VTP thin films. The thicknesses of dielectric layer and electrodes were fixed. Lastly, the sample was transferred into a vacuum chamber for the deposition of 100 nm Al drain electrode on top of the VTP layer under 0.0024 kPa base pressure. A shadow mask was applied to control the area and the shape of Al electrodes. The device area, defined by the crossover area between S-D electrodes, was 3.03 mm^2. The cross-sectional views of the fabricated LOFET and VOFET are shown in Figures 4.1(a) and (b), respectively. Next, the fabricated devices were electrically characterized under standard steady state conditions using Keithley B2900A source meter, while the film thickness was measured with KLA Tencor Surface profilometer (model P-6 Stylus Profiler).

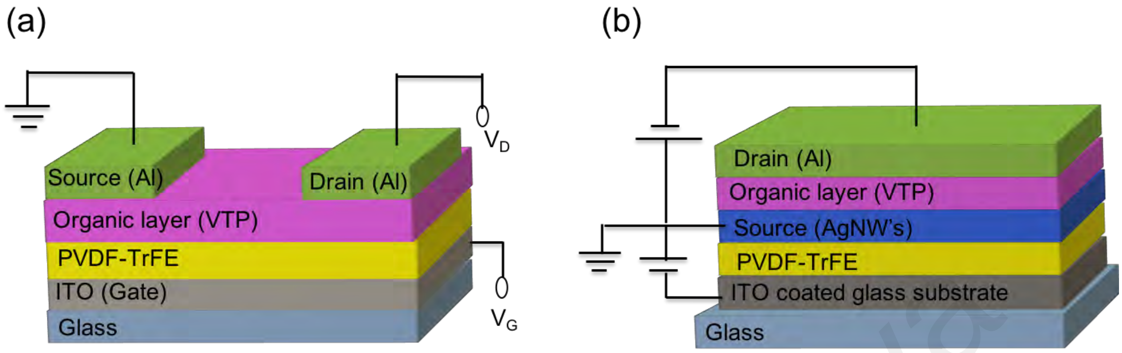

Figure 4.1: Cross-sectional views of (a) LOFET, and (b) VOFET

4.4 Results and discussion

4.4.1 Determination of energy band gap of VTP

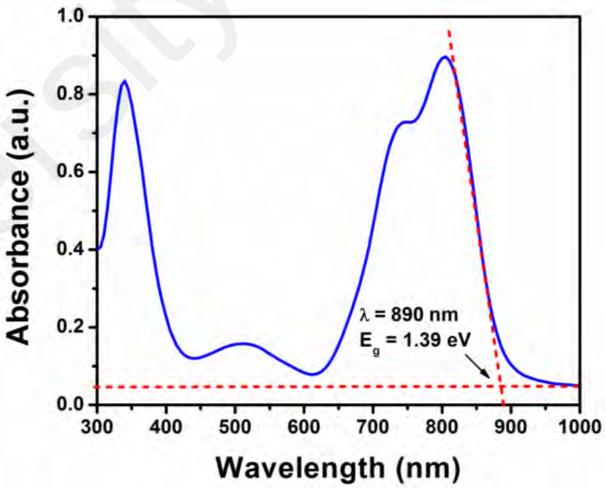

Figure 4.2: UV-vis absorption spectrum of VTP thin film to measure the optical band gap

The electronic absorption spectrum of VTP thin film was characterized via UV-Vis spectroscopy, as illustrated in Figure 4.2. The two methods employed to determine the energy band gap are: 1) absorption spectra, and 2) Tauc gap relation. Schlaf et al.,

(2000) asserted that the energy band gap for the first mentioned can be extracted from the UV-vis absorption spectrum by extrapolating a line on a dominant peak towards a corrected absorption base line.

The Q-band peak was selected, instead of the Soret band due to the promotion of electrons from HOMO to LUMO level in VTP. As depicted in Section 2.4, Q and Soret bands refer to the transition from ground to the first and the second excited state, respectively. The calculation of energy band gap in the Soret band may not be as precise as it represents the transitions from the internal orbital. The red shifting of the Q band of VTP, in comparison to the other Pc, is attributable to the expansion of π conjugation in the molecular structure. The value of wavelength at the intersection of both lines can be applied to determine the optical energy band gap through Equation (4.1), as given below:

$$E_g = \frac{1241}{\lambda}\ eV \tag{4.1}$$

Turning to this study, based on Figure 4.2, the intersection of both lines was noted at 890 nm, which corresponds to optical energy band gap of 1.39 eV.

The second method that determines the optical band gap is the Tauc gap, wherein this technique has been acknowledged to offer more accurate value in characterizing the optical band gap of amorphous semiconductor material (Viezbicke et al., 2015). This approach uses the near-edge region that can fit a simple expression, whereby the intercept gives the band-gap, while the fitting exponent determines the electronic transition as direct or indirect gap. In Tauc plot, the square of absorption coefficient and photons energy $(\alpha E)^2$ is plotted against the photon energy using the following expression (Rafique et al., 2016; Stenzel, 2005):

$$(\alpha hv)^r = \alpha_0\left(hv - E_g\right) \tag{4.2}$$

where, E_g is the band gap that corresponds to a specified transition that occurs in samples, α_0 denotes a constant, h represents Plank's constant, v refers to transition frequency, and r is an exponent that determines the band of transitions classification. The r value may reflect 2, 1/2, 2/3, and 1/3, respectively in relation to direct allowed, direct forbidden, indirect allowed, and indirect forbidden transitions (Mohammadian-Kohol et al., 2016). Meanwhile, α denotes absorption coefficient that is expressed as $\alpha = 2.303\, A/t$, where A and t refer to absorption and thickness of film, respectively (Muhammad & Sulaiman et al., 2011). The optical band gap is determined from the extrapolated values from the straight line to the abscissa. Figure 4.3 illustrates the Tauc plot of $(\alpha E)^2$ versus photon energy (E) of VTP thin film, wherein the value of optical band gap evaluated via Tauc plot method is 1.42 eV.

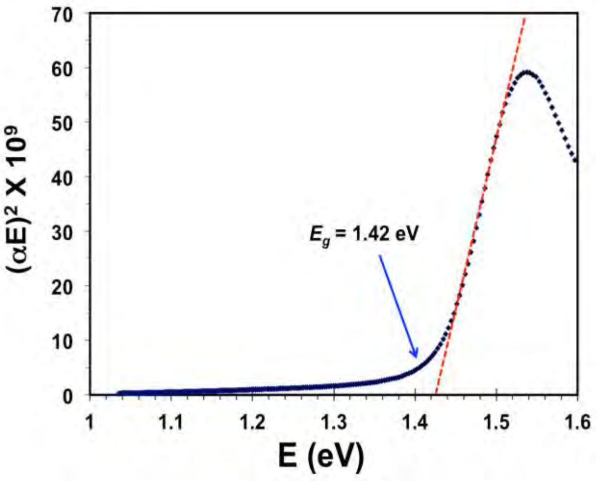

Figure 4.3: The Tauc plot method

In order to ascertain the type of transitions, Equation 4.2 can be manipulated by embedding natural logarithm and derivative, as given in the following:

$$\frac{d[ln\ (\alpha h\nu)]}{d[h\nu]} = \frac{r}{h\nu - E_g} \tag{4.3}$$

Figure 4.4 portrays the plot of $\frac{d[\ln(\alpha h\nu)]}{d[h\nu]}$. The slope of $\ln(\alpha h\nu)$ versus $\ln(h\nu - E_g)$ determined the value of r, and in this case, the value of $r \sim 2$ signified the existence of direct allowed optical transitions between intermolecular energy bands in VTP thin films. This appears to be in line with band-to-band transition in other Pcs group (Collins et al., 1993; El Nhass et al., 2001; Krier et al., 1993).

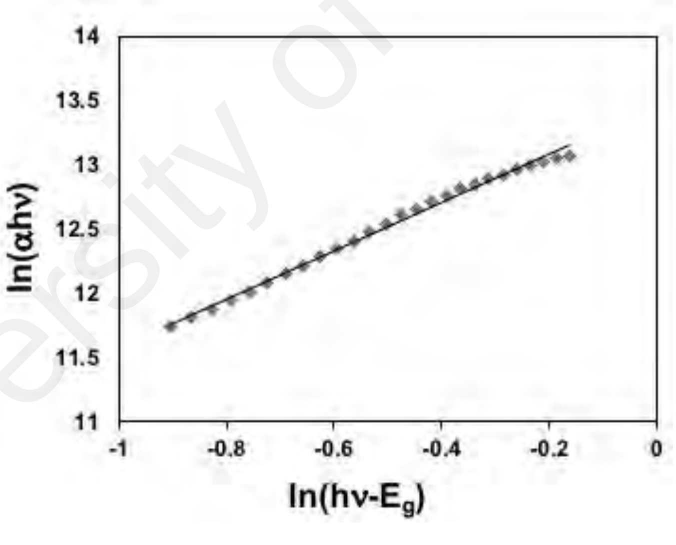

Figure 4.4: $\ln(\boldsymbol{\alpha h\nu})$ versus $\ln(\boldsymbol{h\nu - E_g})$ to determine the type of transition

4.4.2 Determination of HOMO-LUMO of VTP

The values of HOMO and LUMO of organic semiconductors compound are the fundamental parameters in designing and fabricating the electrical devices. In this study, both HOMO-LUMO levels of VTP were determined via electrochemical analysis. These values are significant as they ascertain that materials between metal, organic materials, and metal in energy level are aligned during fabrication of device, so as to allow the charge carriers to move under the influence of electric field (Meixner et al., 2006). Figures 4.5 and 4.6 illustrate the oxidation and reduction curves of VTP thin film, respectively, while Equation 4.4 presents the direct calculation of HOMO-LUMO in an empirical manner:

$$E_{HOMO/LUMO} = -e\,[E_{OX/RED} + 4.4] \tag{4.4}$$

Where E_{OX} and E_{RED} reflect the onset values for oxidation and reduction curves, respectively. The -4.4 eV value applied in the equation refers to the value of ferrocene that functioned as known reference in light of vacuum level (Shafiee et al., 2011). The values of E_{OX} and E_{RED} onsets were 0.7 *eV* and -0.5 *eV*, respectively, based on the plots; while the calculation resulted in -5.10 *eV* and -3.90 *eV* for HOMO and LUMO energy levels of VTP, respectively.

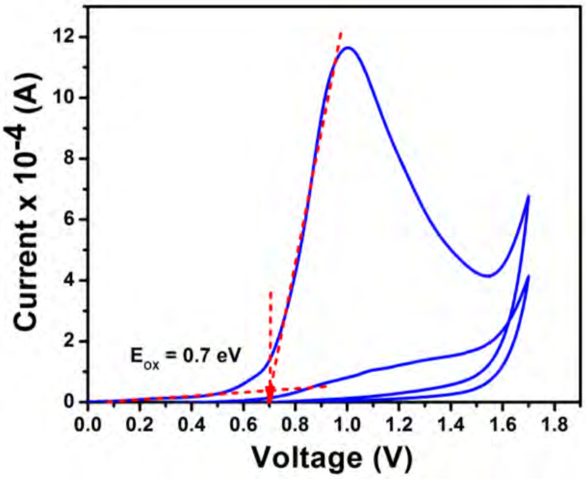

Figure 4.5: Current-voltage curve of VTP for oxidation curve

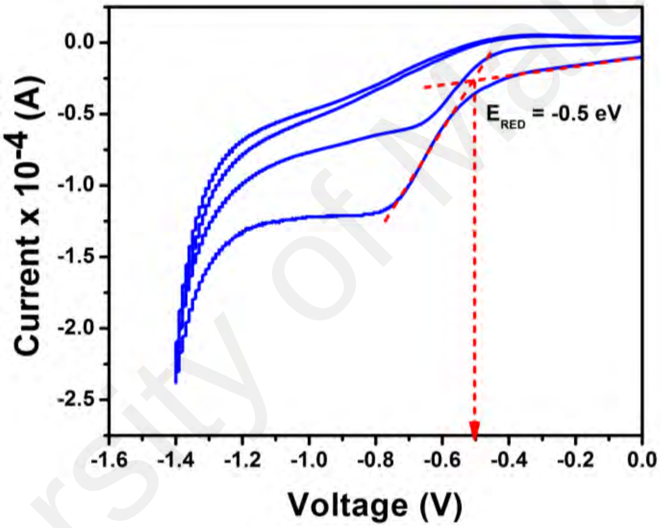

Figure 4.6: Current-voltage curve of VTP for reduction curve

4.4.3 Current-Voltage (*I-V*) performance of lateral OFETs (LOFETs)

This performance of VTP as the active layer in the fabricated OFET device was assessed by looking into output and transfer characteristics. Figure 4.7 displays the output characteristics, in which *I-V* values are plotted by biasing the negative D-S voltage, V_{DS}, at fixed negative G-S voltage, V_{GS}. The increment of J_{DS} at each increment of $-V_{GS}$ revealed that the device operated in *p*-channel (holes charge carrier or positive charge) accumulation type OFET. Nonetheless, Figure 4.7 discloses that the output characteristics did not adhere to the normal curve in LOFET.

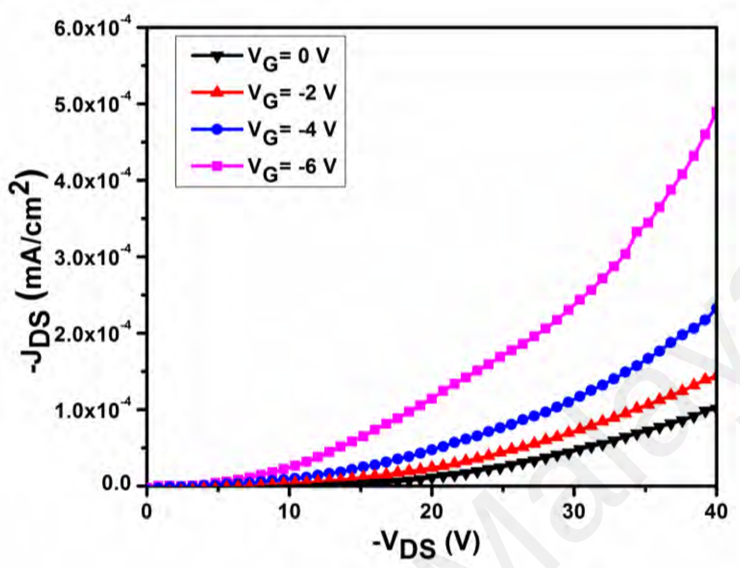

Figure 4.7: Output characteristics of lateral OFET curve

The J_{DS}-V_{DS} characteristics turned parabolic when the device was operated in the linear region and failed to attain the saturation region. Failure to meet saturation could probably due to the preformed channel that resulted in incomplete formation of pinch off current. Since it is common to characterize OFETs using high voltage range (Lai et al., 2018), a technical limitation is reported here at the time of characterization due to constriction in power supply at the laboratory up to merely 40 *V* that restricted the voltage range only to linear region. Past studies suggested that in order to gain saturation region, operating the device at higher drain or gate voltages is a must, primarily due to the irregular deposition of organic semiconductor around the contacts during fabrication, instead of the device structure (Cosseddu & Bonfiglio, 2007; Ishikawa et al., 2010; Mittal et al., 2012).

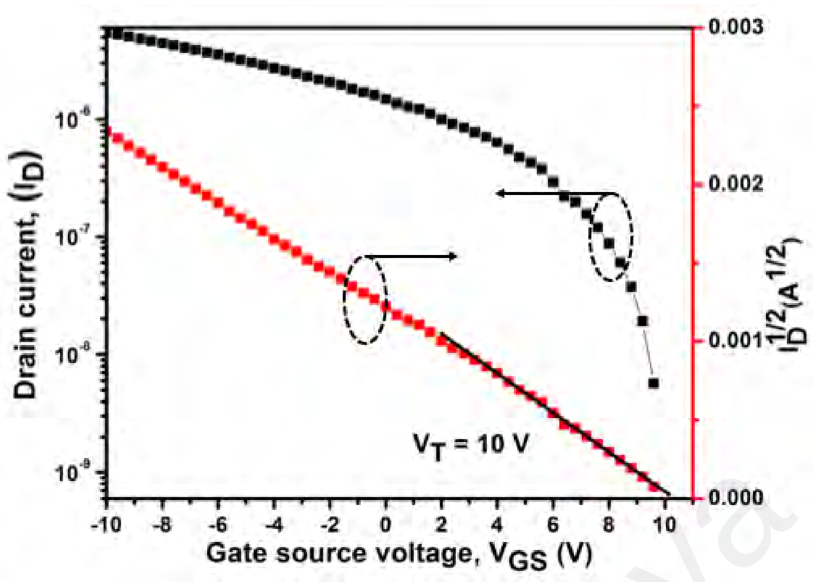

Figure 4.8: Transfer characteristics of lateral OFET curve at V_{DS} = - 10 V

Figure 4.8 shows the transfer characteristic curve of VTP-based LOFET, expressed as follows; I_D versus G-S voltage, V_{GS} at constant S-D bias, and V_{DS} = -10 *V*. Increment of I_D towards negative voltage values (see Figure 4.8) revealed that the device operated as *p*-type transistor with the semiconducting VTP material. For the *p*-type material to function in the device, $V_{GS} < 0$ V ascertains flow of current. The on–off current ratio (I_{on}/I_{off}) is a vital parameter that describes the performance of a transistor. This ratio, which reveals the ability of a device to shut down, is retrieved from the transfer curve by dividing the maximum I_D over its pinch-off current. Next, the threshold voltage (V_T) was determined from the intersection of the linear relation between the square root of output drain current and V_{GS}. The V_T value indicates the starting point of the electric current flow (Kymissis, 2008). Figure 4.8 displays that the ratio of the on-to-off current for VTP-based OFET is 10^2, while the apparent threshold voltage is 10 *V*.

4.4.4 Current-Voltage (*I-V*) performance of vertical OFET (VOFET)

In enhancing the VTP-based LOFET, the device structure was modified to vertical arrangement, whereby the active layer (VTP) was sandwiched between S-D electrodes. Concurrently, the thickness of VTP was optimized to benefit from the best optimum transistor characteristics. The FESEM images in Figure 4.9 (a) display that the AgNW covered the whole substrate surface. Both the length and diameter of AgNWs determined from the FESEM exhibited in Figure 4.9 (b) are ~15 μm and ~20 nm, respectively. The AFM images in Figures 4.9 (c) and (d) portrays the rough surface morphology with surface roughness RMS of ~14 nm.

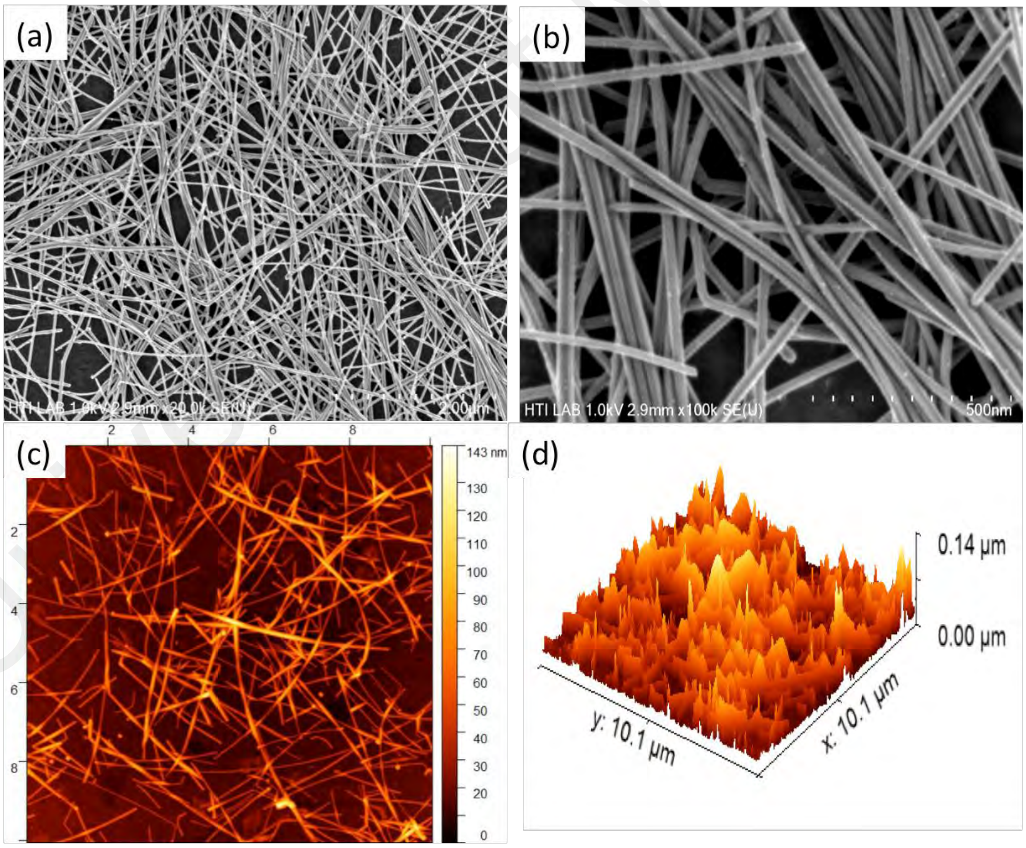

Figure 4.9: a) FESEM image of AgNWs at low magnification, (b) FESEM image of AgNWs at high magnification, (c) AFM image of AgNWs, and (d) AFM 3D cross-section image of AgNWs

Figure 4.10(a) illustrates the schematic diagram of the solution-processed VOFET that is composed of two connected cells, which are capacitor and active cells. The middle electrode sandwiched between these two cells is the source electrode, which has thin layer and rough morphology. The top and bottom electrodes function as the drain and gate electrodes, respectively. The polarization conditions were biased by using varied polarities to the gate and drain electrodes, thus resulting in negative bias for the *p*-type organic materials (Li et al., 2008). The source electrode, nevertheless, remained grounded throughout the operation. Yang and Wudl asserted that a nanometre-scale phenomenon called 'near field effect' could take place when the charge distribution length (λ) (at source interface) is comparable with the thickness (d) of the source electrode layer. They added that an electric field that exists at the organic/source interface modifies the current between S-D electrodes (Yang & Wudl, 2006).

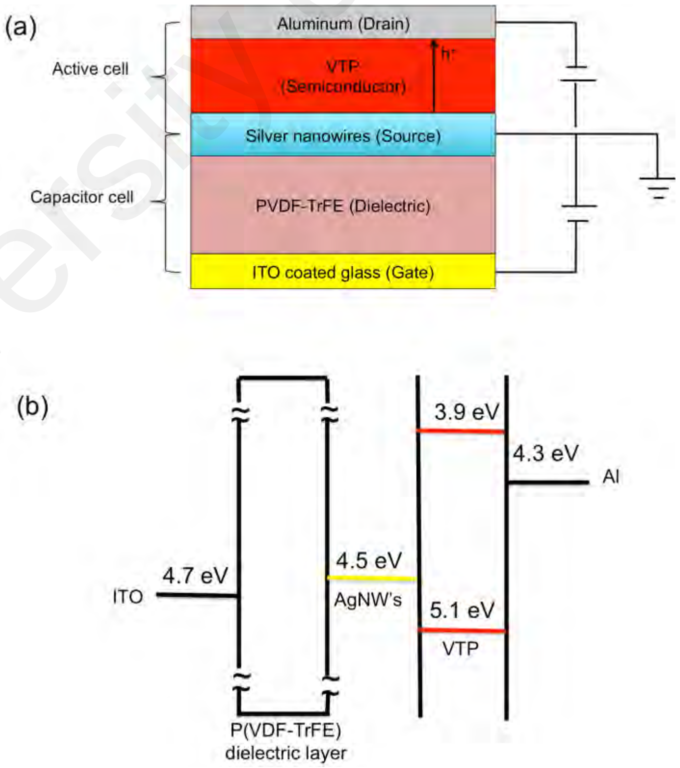

Figure 4.10: (a) A schematic diagram of the VOFET structure with the active and capacitor cells sandwiching the source electrode. (b) Energy-level diagram displaying the work function of certain elements and the HOMO-LUMO energy of each material

Figure 4.10(b) portrays the energy-level diagram based on the work functions of ITO, Al, and AgNWs, as well as the HOMO/LUMO of VTP determined earlier. A significant concept pertaining to the VOFET refers to the control of charge injection, particularly the hole injection from the source electrode to the organic active layer (Yang & Wudl, 2006). The ambipolar transport behavior, hence, may be achieved via VTP thin film due to similar injection barrier heights for both charge carriers at S-D electrodes, after weighing in the absence of interface polarization. The use of Pc derivative served as *p*-type material in fabricating the organic transistor as a hole injection or transport layer. This is due to the adsorbed oxygen that functioned as an acceptor on the band gap (Kvitschal et al., 2015). The hole transport is potentially more dominant in the devices when the drain is negatively biased.

The VTP layer in this study, which served as *p*-type organic semiconductor, was applied as the active cell. The current injection for the active cell was regulated by the amount of hole injected from the source electrode. Figure 4.11 portrays a schematic band diagram between source and organic interface.

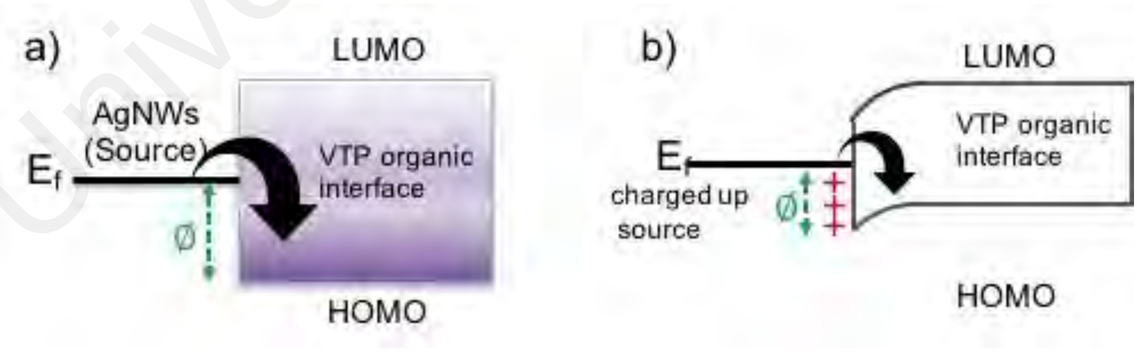

Figure 4.11: A schematic band diagram between source and VTP organic layer interface a) without bias, and b) with negative gate bias

As illustrated in Figure 4.11, prior to biasing the gate voltage ($V_G = 0\ V$), the large barrier height at the source/organic interface prevented the hole being injected into the organic layer efficiently. The capacitor cell had built up when the negative gate voltage was biased, which generated positive charge in the source electrode layer. Therefore, the barrier height between source and organic layers was lowered by a certain value, so as to allow the injection into the organic layer and to give rise to the S-D current upon the application of drain bias.

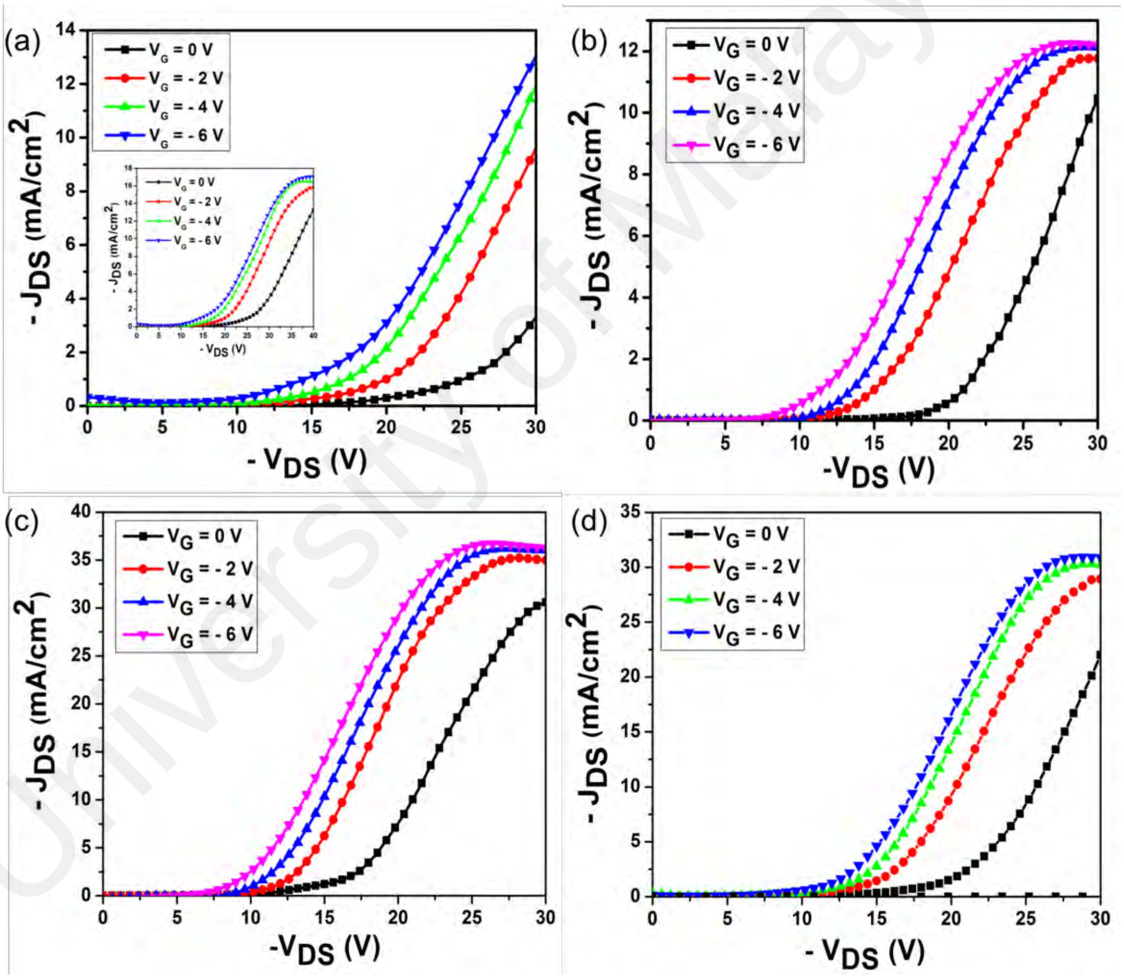

Figure 4.12: Output characteristics of VOFETs with varied VTP thicknesses at (a) 90 ± 5 nm, (b) 80 ± 5 nm, (c) 66 ± 5 nm, and (d) 52 ± 5 nm (Inset in (a) is the output characteristic of $-V_{DS} = 0 - 40\ V$)

Figure 4.12 illustrates the output characteristics ($-J_{DS}$ vs $-V_{DS}$) of VOFETs with varied channel lengths. The channel length between S-D electrodes was determined by the thickness of active layer measured using KLA Tencor surface profilometer. Table 4.1 summarizes the parameters retrieved from each device. Figure 4.12 discloses that the output current density, J_{DS}, was controlled by $-V_{GS}$, with J_{DS} within the $mAcm^{-2}$ range. The inset in Figure 4.12(a) portrays V_{DS} was swept from 0 to -40 V to reflect a small range of output current saturation, while Figures 4.12 (a-d) show that V_{DS} was swept from 0 to -30 V with varied negative gate voltages.

All curves signified similar output profiles that were composed of linear and saturation regions. The maximum output current density achieved from the plotted curves in Figure 4.12 (c) was indicated by VTP thickness of 66 ± 5 nm with value of 37.0 mA/cm^2. This value is relatively higher than the output current reported by Kudo et al., (2001). In comparison to devices with other thicknesses (90 ± 5 nm, 80 ± 5 nm, and 52 ± 5 nm) that are lower in both linear and saturation regimes, the active layer thickness potentially affected the field-effect current modulation.

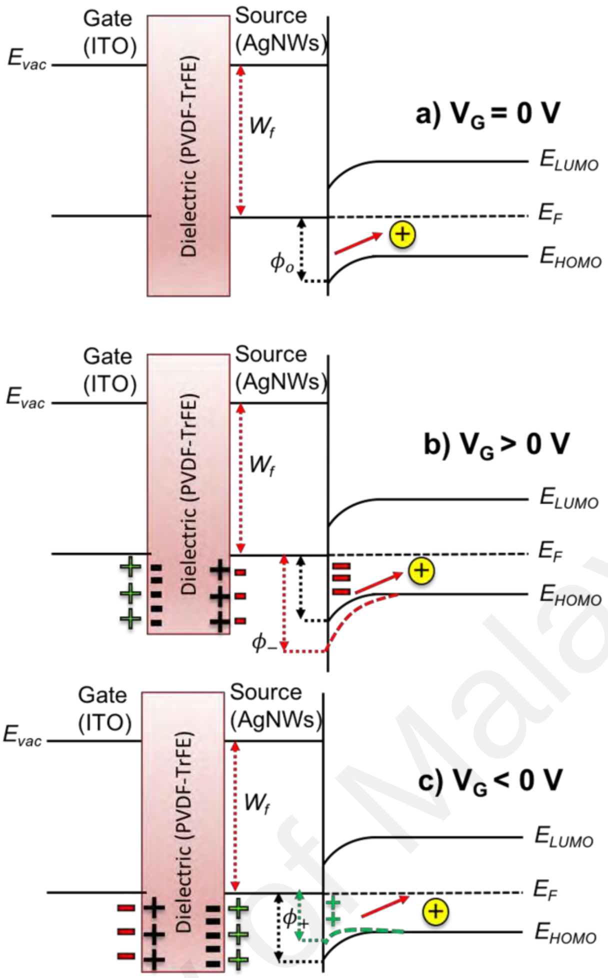

Figure 4.13: Schematic diagram of energy band diagram alignment at ITO/PVDF-TrFE/AgNWs/VTP VOFETs device at different biasing voltage at (a) $V_G = 0\ V$, (b) $V_G > 0\ V$ and (c) $V_G < 0\ V$

Figure 4.13 illustrates a schematic diagram of hole injection mechanism at the AgNWs/VTP interface with varying conditions of gate voltage, V_G, in which the mechanism is similar to a Schottky barrier transistor (Yang & Wudl, 2006). As mentioned above in Figure 4.11, when $V_G = 0\ V$, the high injection barrier height prevented efficient hole injection from the source electrode. When the gate was positively biased, $V_G > 0$, the capacitor cell was charged up. Negative charge was developed at the AgNWs/VTP interface, which increased the potential barrier height that decreased hole injection into the VTP layer. At $V_G < 0$, where the gate was biased with negative potential, positive charges accumulated at the AgNWs/VTP interface and lowered the potential barrier height, thus significantly enhancing hole injection from

AgNWs into VTP layer. This condition is reflected by the output characteristics portrayed in Figure 4.12. The generated output current is directly proportional to the amount of charge carrier accumulated in the VTP layer.

Figure 4.14 displays the transfer characteristics expressed as the output current (I_D) value against gate voltage (V_{GS}), which was swept from -10 to 10 V at a constant V_{DS} = -10 V. The VOFET with 66 ± 5 nm thickness (see Figure 4.14 (c)) gave the best I_{on}/I_{off} $\sim 10^5$, when compared with the other three thickness values.

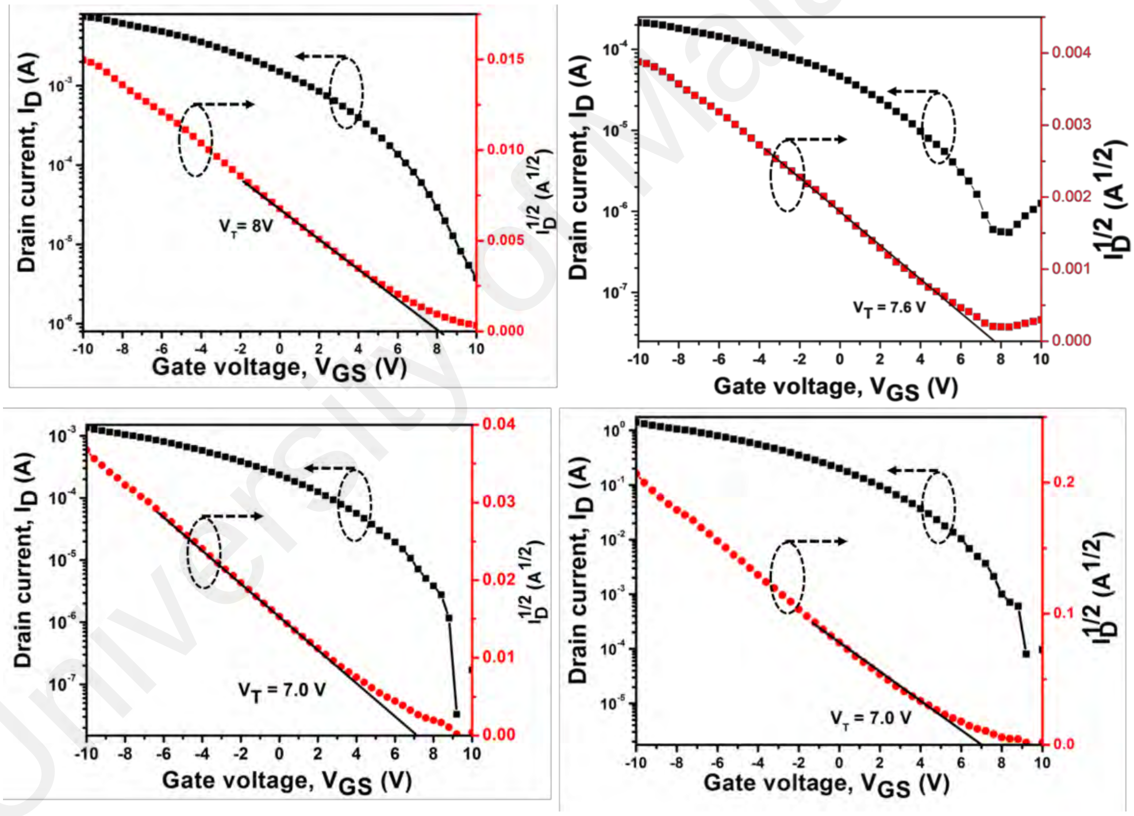

Figure 4.14: Transfer characteristics of VOFETs with varied VTP thicknesses at (a) 90 ± 5 nm, (b) 80 ± 5 nm, (c) 66 ± 5 nm, and (d) 52 ± 5 nm with applied D-S voltage at V_{DS} = -10 V

As depicted in Section 4.4.3, the threshold voltage (V_T) was determined from the intersection of the linear relation between the square root of output drain current and V_{GS}. The V_T, which was measured from the transfer characteristics, showed that both 66 ± 5 nm (7.0 ± 0.2 *V*) and 52 ± 5 nm (7.0 ± 0.2 *V*) were comparable, when compared to 90 ± 5 nm and 80 ± 5 nm thicknesses that recorded higher V_T of 8.0 ± 0.2 *V* and 7.6 ± 0.2 *V*, respectively. Table 4.1 summarizes the thickness, the output D-S current density, the saturation of drain current density, and the turn on-off current ratio for these devices.

Table 4.1: Transistor parameters retrieved from output, as well as transfer characteristics of LOFETs and VOFETs

OFET device structure	**Spin speed (rpm)**	**Channel length ± 5 nm**	**Output current density (mA/cm^2) at $-V_{DS}$ = 30 V**	**Threshold voltage (*V*) ± 0.2 *V***	**Saturation voltage (*V*)**	**ON/OFF ratio**
LOFET	2000	6000	2.5 x 10^{-4}	10.0	-	10^2
VOFET	500	90	12.6	8.0	35	10^3
	1000	80	12.2	7.6	27	10^3
	2000	66	37.0	7.0	25	10^5
	3000	52	32.2	7.0	25	10^4

Table 4.1 lists the extracted transistor parameters from the output and transfer characteristics of LOFET and VOFET. It is evident from Table 4.1 that the arrangements of devices and variations in channel length greatly influenced the transistor performances. As mentioned earlier, the channel length of OFET was evaluated as the gap of S-D (LOFET); while in VOFET, the thickness of VTP film determined the channel length. The channel length in LOFET was 100-fold longer than that of VOFET. The thickness of active layer (VTP) was decreased upon increment in

spin speed. It is observed that the lowest spin speed of 500 rpm formed the thickest VTP layer at 90 ± 5 nm, which gave relatively lower current density of 12.6 mA/cm^2. Despite the expectation that increased film thickness can enhance the morphology of the active layer, it failed to facilitate the flow of current, especially between S-D. Perhaps, the transport of charge carriers was restricted due to increased traps density as the thickness value was getting higher (Yi et al., 2014). When the spin speed was 2000 rpm, the thickness of VTP reduced to 66 ± 5 nm and produced higher output current density of 37 mA/cm^2. At 3000 rpm spin speed, the VTP thickness was further reduced to 52 ± 5 nm, but no increment was noted for output current that recorded ~ 32.2 mA/cm^2, which is slightly lower than the VOFET with 66 ± 5 nm of active channel thickness. This clearly indicates that VOFET with 66 ± 5 nm VTP layer displayed the optimum range of thickness by exerting the best electrical performance than the rest. VOFET with 2000 and 3000 rpm spin speeds displayed similar or approximate outcomes in their threshold and saturation voltages, except for the slight variance noted in the output current values. This minor difference is attributable to the change in the active VTP thickness that has been assumed to dictate the supply volume of charge carriers (Reséndiz et al., 2010).

4.5 Summary

The values of HOMO and LUMO, which were determined via CV measurement, resulted in -5.10 *eV* and -3.90 *eV*, respectively. The optical band gaps of the VTP were 1.39 *eV* and 1.42 *eV* for absorption spectra and Tauc plot, respectively. Two types of OFET arrangements were fabricated by using the simple solution spin coating process. As a result, the VOFET displayed high current, low voltage operational, and high turn on/off ratio, in comparison to LOFET. The results seem to correlate with the literature, whereby this condition is attributed to the short channel length between S-D electrodes in the device structure that eventually enhanced the device characteristics. Additionally, this chapter demonstrated the effect of channel thickness on the performance of VOFET. The best VOFET performance was attained with a VTP layer of 66 ± 5 nm that generated the maximum output current density of 37 mA/cm^2.

CHAPTER 5: VTP-BASED OPTICAL DEVICES

5.1 Introduction

The properties of VTP stand alone and its binary (VTP:$PC_{71}BM$) in utilizing the VTP-based optical devices had been investigated. That being said, this chapter is divided into two main sections; (i) the structural and optical properties of single-layer VTP and the binary blended films, as discussed in detail in the first section. Additionally, the charge transport behavior of single-layer VTP and its blend was assessed via *I-V* conventional method using diode analysis. In section (ii), the optimized optical properties of VTP:$PC_{71}BM$ were selected to evaluate the photovoltaic effect of VTP:$PC_{71}BM$. In optimizing the application of VTP in optical application, the device was utilized with light detector application. The *J-V* characteristics were assessed under dark and illumination conditions to extract the key parameters of photovoltaic effect and OPD. The device was characterized using external quantum efficiency (EQE) spectra to correlate the wavelength dependent sensitivity of the photoactive films.

5.2 Properties of Organic Electronics for Optical Devices

Over the past decades, organic materials have been widely assessed to overcome several shortcomings of the inorganic counterpart in optoelectronic applications. Some unique properties of organic materials are beneficial for the fabrication of OPVs due to enhanced sensitivity, cost effective, environment-friendly, and suitability of facile fabrication methods, such as spin coating, drop casting, dip coating, and spray coating directly from liquid solutions (Ahmad et al., 2011; Fakir et al., 2012). Over the years, bulk heterojunction organic solar cell (BHJ OSC) has been extensively investigated for application at high performance in BHJ OPVs and OPDs, whereby an acceptor and a donor are blended in the photoactive medium to develop D/A interface at the molecular level (Ahmad et al., 2013; Arbab et al., 2015; Koster et al., 2005).

Among the organic materials, MPcs with heterocyclic macrocyclic organic compounds, have been comprehensively evaluated for a range of applications (Abdullah et al., 2012; Roslan et al., 2018). Several MPcs were applied to assess OPVs and OPDs (Ahmad et al., 2013; Farooq et al., 2015; Hamdan et al., 2013; Zafar et al., 2017), including VOPcPhO (Abdullah et al., 2012; Ahmad et al., 2013; Zafar et al., 2014). Turning to this study, an MPc of vanadium metal complex, known as VTP, is proposed. The aromatic structure of VTP reflects that of VOPcPhO, except for its different extended ligands. Basically, the ligands in VTP can potentially alter this molecule photo-absorption sensitivity (Guo et al., 2002; Roslan et al., 2018). To date, VTP has not been applied as the active layer in any fabrication of OPVs and OPDs. This study incorporated a blend of two organic compounds; VTP and $PC_{71}BM$, by primarily focusing on the wavelength below 650 nm, based on the combination of their absorption properties. This blend formed a BHJ structure; a homogenous mixture of donor and acceptor materials with an inter-penetrating networks connection (Zafar et al., 2014). A network structure is bound to improve charge separation and transport of photo-generated charge carriers (Zafar et al., 2016).

Herein, VTP is introduced as a donor material with unique absorption properties, particularly at the lower visible region (Guo et al., 2014). A new composite of donor-acceptor blended system is initiated in this study by integrating VTP (donor) and $PC_{71}BM$ (acceptor). This combination had been selected owing to the electronic, solubility, and optical properties of the two materials. The VTP and $PC_{71}BM$ possess relatively exceptional holes transport and electron transport abilities (Ebenhoch et al., 2015), thus making them highly sought donor and acceptor components, respectively. Both organic materials, VTP and $PC_{71}BM$, display good solubility in most organic solvents, specifically chloroform, which endows to facile solution process-able approaches. This soluble property promotes facile fabrication process, primarily because the main active layer can be easily developed via spin-coating technique. The absorption of both materials that can cover a range of light has a significant function in capturing specific light wavelength within visible range. By virtue of synergic absorption profile of VTP and $PC_{71}BM$ matrix, light absorbance towards lower wavelength region has been expected to enhance in full visible spectrum. To the best of the author's knowledge, this blend system has not been reported elsewhere, thus the overarching aim of the thesis to introduce a novel BHJ system to assess photovoltaic response, besides contributing to the progression of highly sensitive photodetectors.

5.3 Experimental procedure

The materials, VTP and $PC_{71}BM$, were purchased from Sigma Aldrich (St. Louis, USA) and applied without further alteration. Each material was dissolved separately in chloroform to prepare 10 mg/mL solution and was continuously stirred for hours. Both VTP and $PC_{71}BM$ were mixed in three volume ratios (1.0:1.0, 1.0:1.2, and 1.0:1.4) prior to stirring for an hour in a nitrogen-filled glove box. The ITO-coated glass substrates (Ossila, UK) were cleaned thoroughly using acetone, isopropyl alcohol, and de-ionized water, and later dried using nitrogen stream. A PEDOT:PSS solution (PH1000 from H.C.Stack) that served as hole transport layer (HTL) was employed to facilitate efficient hole collection at the ITO electrode. The solution was filtered using 0.45 µm PTFE filter (Whatman, Germany), spin coated at 3000 rpm for 60 s to generate 40 nm thin layer on the surface of ITO and annealed for 30 min at 120 ºC. Next, the VTP:$PC_{71}BM$ blended solution was filtered with 0.20 µm PTFE filter and spin coated on PEDOT:PSS surface at 2000 rpm for 30 s to produce 65 ± 5 nm thick layer film. Later, it annealed at 70 ºC for 30 min to ascertain complete solvent evaporation. Finally, aluminum was thermally deposited in vacuum under 2×10^{-7} torr base pressure via shadow mask to produce 100 nm top-contacts that constituted 0.045 cm^2 photo-active areas for OSC and photodetector devices. The sample devices were encapsulated by epoxy glue and cured using UV light prior to electrical characterization using Keithley 236 Source Measure Unit equipped with Oriel 67005 (Xenon arc lamp) solar simulator. All characterizations were performed at 300 K. The thicknesses of all films were determined using KLA Tencor Surface Profilometer (model P-6 Stylus Profiler). All VTP, $PC_{71}BM$, and VTP:$PC_{71}BM$ films were characterized using photoluminescence spectroscope equipped with 325 nm wavelength laser source (Renishaw, Gloucestershire, UK) and UV-visible spectroscope (PerkinElmer LAMBDA 900). Surface roughness of the samples were characterized using Hitachi AFM5100N with SI-DF3 cantilever and 3 × 3 µm scan rate. The cross-section of the samples were analyzed using field emission scanning electron microscopy-energy dispersive X-ray spectroscope (FESEM-EDX) (JSM 7600-F, JEOL Ltd., Tokyo, Japan).

Figure 5.1 illustrates the (a) molecular structure of VTP and $PC_{71}BM$, (b) schematic diagram of OPVs and OPDs, (c) cross-section FESEM image of the prepared samples, and (d) device schematic diagram mechanism with energy values reported in the previous chapter (Roslan et al., 2018; Wang et al., 2015). Figure 5.1(c) discloses that the thickness of PEDOT:PSS, active layer (VTP:$PC_{71}BM$), and Al were 40 nm, 65 nm, and 75 nm, respectively. Next, Figure 5.1(d) portrays the principle of photo detection mechanism that incorporated the generation, the diffusion, the separation of excitons, and the transport of charge carriers to their respective electrodes. Initially, it began with light absorption and formation of photo-generated excitons. After that, the excitons were diffused to the D/A interface, where electron-hole pairs were dissociated into free electrons and holes to generate photocurrent. The electrons and holes were attracted to LUMO (acceptor) and HOMO (donor), respectively. Finally, these separated charges were transported to the electrodes to produce photocurrent in external circuit (Choy, 2012).

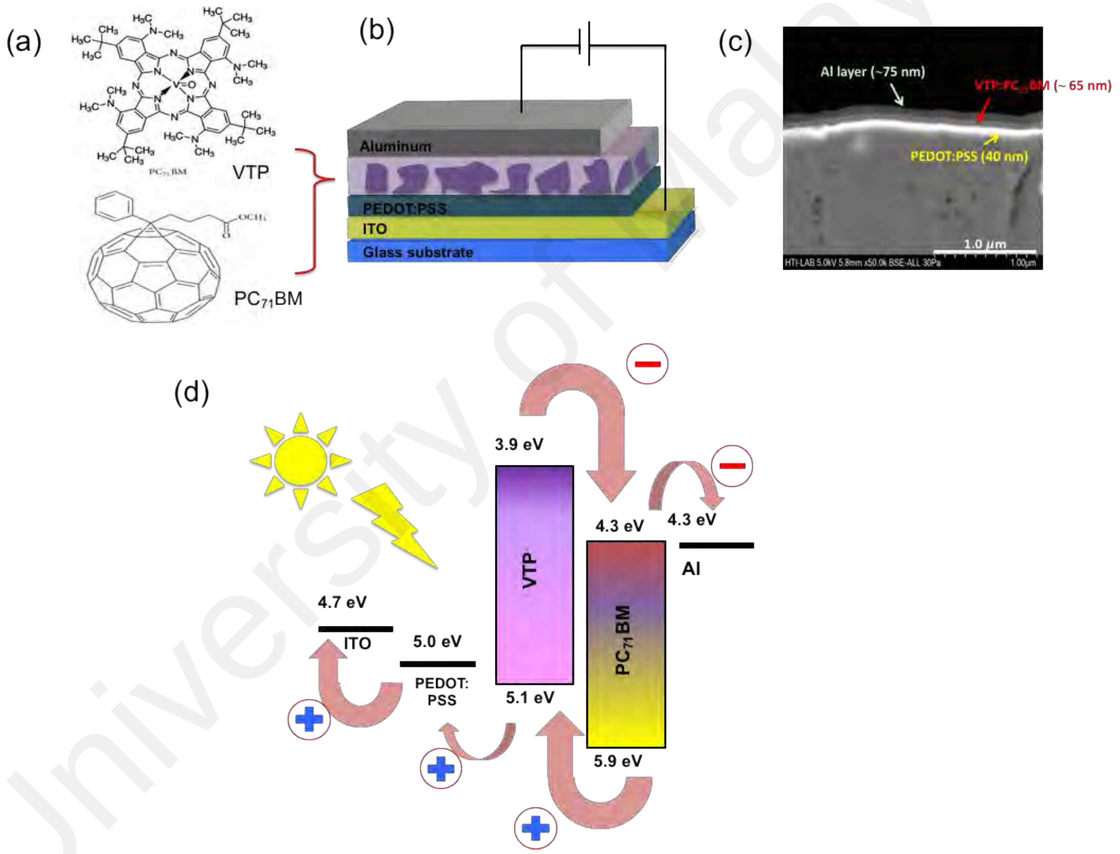

Figure 5.1: a) The molecular structure of VTP (Roslan et al., 2018) and $PC_{71}BM$ (Zafar et al., 2017), (b) a schematic diagram of organic photovoltaic and organic photodetector, (c) cross-section image of prepared sample, and (d)eEnergy diagram for ITO/PEDOT:PSS/VTP:$PC_{71}BM$/Al organic photovoltaic and organic photodetector

Figure 5.1(d) exemplifies a diagram on the device energy level. In ensuring efficient and unlimited charge separation at the D/A interface, appropriate photoactive donor acceptor pair has to be selected, wherein LUMO energy levels of acceptor must be placed below the donor. Additionally, the energy offset of the LUMO for both donor and acceptor energy level has to be sufficient for photo excitons dissociation.

5.4 Results and discussion

5.4.1 Structural properties using Raman spectrum of VTP and blended thin film ($VTP:PC_{71}BM$)

Raman characterization was executed with 514 nm wavelength of laser source. Figure 5.2 illustrate the micro-Raman spectra of independent VTP and $PC_{71}BM$, while Figure 5.3 portrays a variety of blended films using the two organic materials applied in this study.

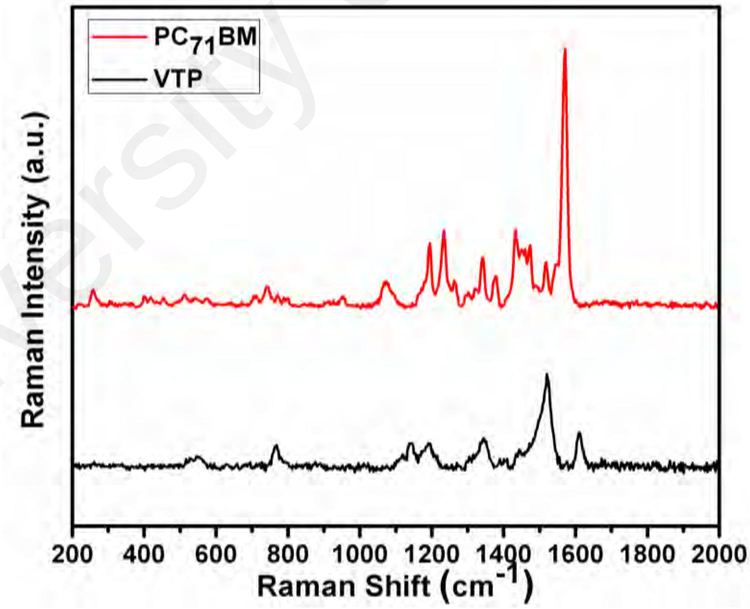

Figure 5.2: Raman spectra of VTP and $PC_{71}BM$ stand alone

As for the Raman shifts noted in VTP thin film, the strong peak at 1610 cm^{-1} is attributed to skeletal C=C stretching vibration. The band at 1520 cm^{-1} corresponds to the vibration of nitrogen bridging atoms, while the band at 1403 cm^{-1} is related to the isoindole stretching vibrations, and the band at 1341 cm^{-1} is linked with C-H deformation. Bands positioned at 1186 cm^{-1} and 1137 cm^{-1} are ascribed to CH bending, whereas peaks noted at 768 cm^{-1} and 545 cm^{-1} are related to ring vibration and ring deformation, respectively.

The Raman spectrum of PC$_{71}$BM thin film displayed significant peak at higher intensity protruding at 1572 cm^{-1} assigned to C=C stretching. The medium intensity noted at 1515 cm^{-1} is related to pyrrole stretching, whereas peaks at 1474 cm^{-1} and 1434 cm^{-1} are linked with ring stretching. Additional medium intensity peak at 1377 cm^{-1} is associated with CH$_3$ deformation, while 1342 cm^{-1} and 1263 cm^{-1} are attributed to C-H deformation. The peak positioned at 1234 cm^{-1} denotes ring vibration, whereas peaks noted at 1193 cm^{-1}, 1076 cm^{-1}, and 951cm^{-1} reflect CH bending. Band at 511 – 740 cm^{-1} range signify ring deformation, while band observed at 771 cm^{-1} and 399 cm^{-1} represent ring vibration and deformation, respectively.

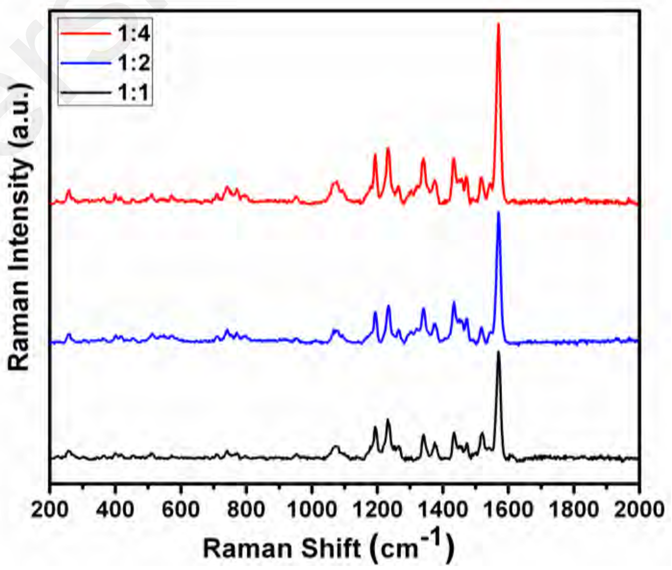

Figure 5.3: Raman spectra of binary blended films

Clearly, Figure 5.3 exhibits that incorporating $PC_{71}BM$ into VTP had significantly altered the molecular structure of VTP thin film. This is verified by the presence and absence of Raman peaks in VTP:$PC_{71}BM$ blended thin film, whereby some peaks noted in VTP thin film were absent, particularly at 545, 1186, and 1610 cm^{-1}. The Raman spectrum for blended film yielded bands almost similar to that of pure $PC_{71}BM$, except for some bands that shifted to lower wavenumber, namely 258, 509, 571, 1375, 1431, 1471, and 1569 cm^{-1}. This signifies that $PC_{71}BM$ functioned as a dominant material in the VTP:$PC_{71}BM$ blend, in which the impact of VTP on the Raman modes of $PC_{71}BM$ seemed almost negligible. The downward shifting of wavenumber revealed that the effective conjugation length of the structure was extended. The Raman shifts for VTP, $PC_{71}BM$, and VTP:$PC_{71}BM$ blended films are portrayed in Table 5.1.

Table 5.1: Raman shifts of VTP, $PC_{71}BM$ and VTP:$PC_{71}BM$ blended films

VTP	**$PC_{71}BM$**	**VTP:$PC_{71}BM$**	**Approximate assignment of vibrations**
-	261	258	Ring deformation
-	399	399	Ring deformation
-	451	451	C-C deformation
-	511	509	Ring deformation
545	542	-	Ring deformation
-	576	571	Ring deformation
-	707	709	Ring deformation
-	740	740	Ring deformation
768	771	770	Ring vibration
-	951	953	CH bending
-	1076	1076	CH bending

Table 5.1, continued

1137	1193	1193	CH bending
1186	-	-	CH bending
-	1234	1234	Ring vibration
-	1263	1265	C-H deformation
1342	1342	1341	C-H deformation
-	1377	1375	CH3 deformation
1403	1434	1431	Ring stretching
-	1474	1471	Ring stretching
1520	1516	1518	Pyrrole stretching
-	1572	1569	C=C stretching
1610	-	-	C=C stretching

5.4.2 Absorption properties of pristine VTP, $PC_{71}BM$ and its blended thin film (VTP:$PC_{71}BM$)

The BHJ system is beneficial in terms of its ability in tuning the optical properties of blended film, viz. wavelength-tunability. With this unique ability, the absorption properties of the photoactive blended film can be extended easily to a whole new visible range (Zafar et al., 2014). The absorption spectra of individual films (VTP and $PC_{71}BM$) and blended film (VTP:$PC_{71}BM$) are illustrated in Figures 5.4 and 5.5, respectively. Figure 5.4 portrays the pristine VTP absorption spectrum. Based on the UV-Vis absorption spectrum, the Pc thin films derived from MOs within aromatic 18π electron system and from overlapping orbitals on the central metal atoms. The VTP showcased two broad peaks; the first intense peak at B-band region of 342 nm, and the second broad peak at Q-band region of 810 nm with a shoulder at ~ 742 nm (Roslan et al., 2018). The weak band noted at 514 nm for VTP thin film is linked to $n \rightarrow \pi^*$ transition that derives from the nitrogen lone pair of electrons (Chen et al., 2016). In fact, most films generated by MPc family tend to display these three absorption peaks within the two well-known regions (Rao et al., 2011).

The B band is reflective of the electronic transitions that occur between molecules, whereas the Q band is attributable to the HOMO-LUMO ($\pi - \pi^*$) transition that takes place in Pc ring (Torre et al., 2004). The strongest absorption peak noted at the Q-band region represents the $\pi - \pi^*$ transition that seemed dominant in the second transition, instead of the initial transition for all rates of spin coating. The Q band displays maximum absorption peak at a remote wavelength region, primarily because of the coordination of ligand to metallic ion in Pc (Sanchez-Vergara et al., 2012). The red shift showcased in VTP absorption spectrum, in comparison to that of Pc, is associated to the expansion of extended π ligands within the molecular structure Sakamoto and Ohno (1997) revealed that shifting of absorption wavelength relies on the alteration that takes place in electron distribution within the Pc macro-ring substituents.

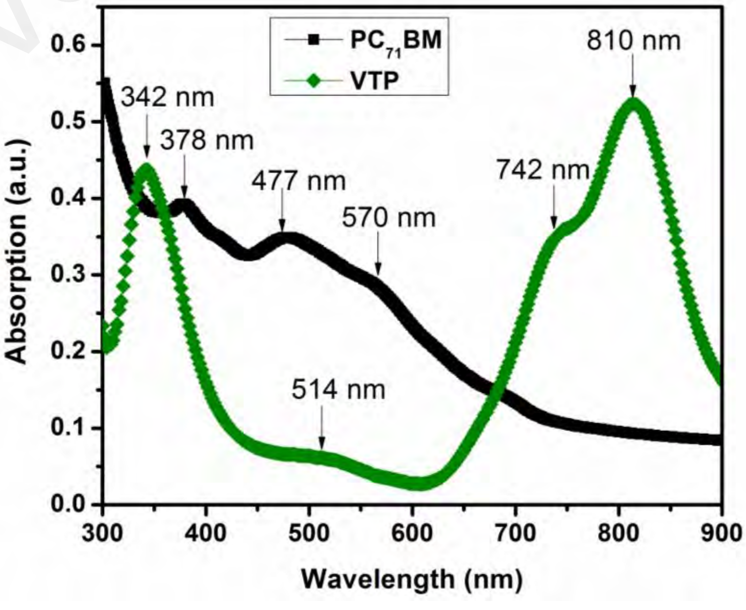

Figure 5.4: UV-Vis absorption spectra of VTP and $PC_{71}BM$ stand alone

The absorption of $PC_{71}BM$ enhanced the tendency towards a lower wavelength range (below 650 nm) with two absorption peaks noted at 378 and 477 nm, including a shoulder at 570 nm (Abdullah et al., 2015). Less absorption was also observed, particularly at the valley between B-band and Q-band of VTP, as well as beyond 650 nm in $PC_{71}BM$. The combination of VTP and $PC_{71}BM$ appears to broaden the absorption bandwidth to a longer wavelength across the red region. Figure 5.5 illustrates that the valley between B-band and Q-band, which corresponds to VTP, reduced due to the presence of $PC_{71}BM$. The blend of the two components enhanced the absorption of light at lower visible wavelength range, particularly below 650 nm. This optimal combination is highly sought for fabrication of exceptional optical devices.

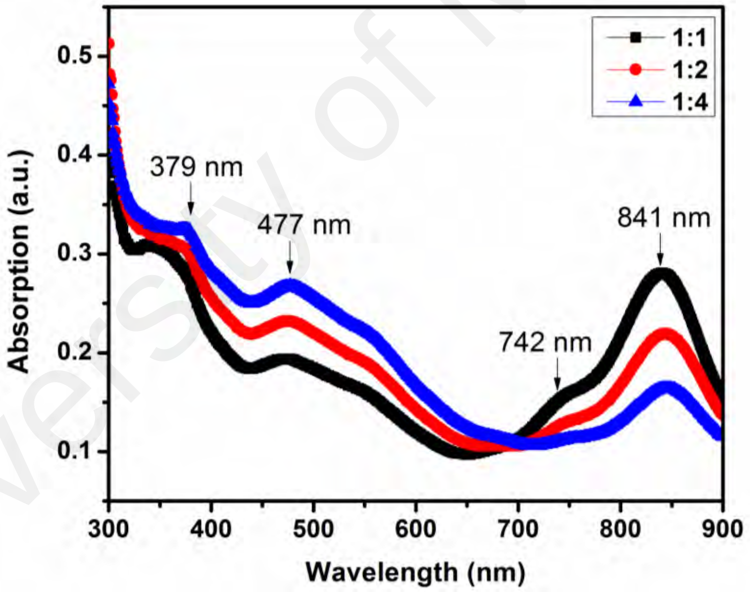

Figure 5.5: Absorption profiles of binary blended film (VTP:$PC_{71}BM$) with varied volumetric ratios

5.4.3 Photoluminescence spectra of pristine VTP, $PC_{71}BM$ and its quenching effect of blended thin film (VTP:$PC_{71}BM$)

The photoluminescence spectra were examined to determine the photophysical properties, which correlate to the dissociation of excitons produced in the photoactive film. Theoretically, the decrease in PL intensity (increased quenching effect) enhanced the efficiency of electron-hole pair dissociation. The PL spectra of pristine VTP, $PC_{71}BM$, and blended films were assessed at room temperature using 325 nm excitation wavelength that ranged between 600 and 900 nm.

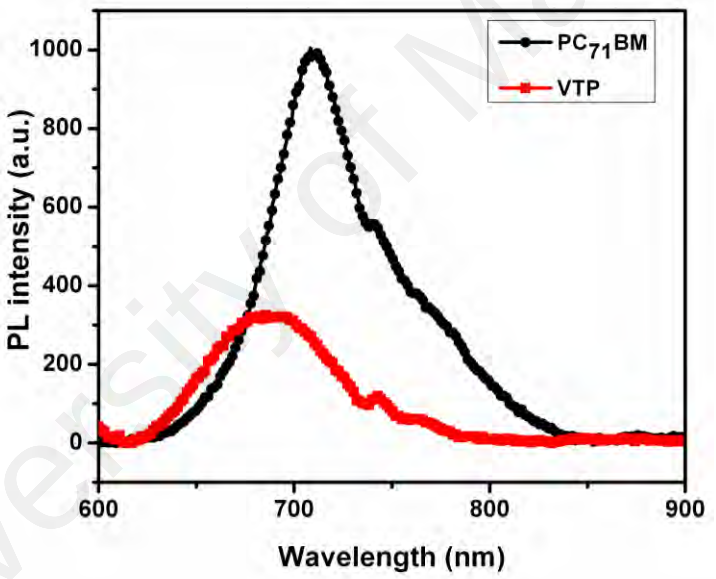

Figure 5.6: PL spectra of pristine VTP and $PC_{71}BM$

A broad peak of VTP photoluminescence emission (see Figure 5.6) was noted at 687 nm in correspondence to the red region, whereas the emission of PL spectrum for $PC_{71}BM$ was observed around the same region (711 nm) with a shoulder at longer wavelength region ~ 740 nm. The outcomes of $PC_{71}BM$ are in agreement with those depicted in the literature (Zafar et al., 2015; 2017). After the process of photoexcitation, the generated excitons in interpenetrating the D/A matrix are diffused to the D/A interface and experience dissociation. The excitons may either undergo charge transfer (charges diffuse to their respective electrodes and generate photocurrent) or energy transfer, and followed by radiative recombination (Dittmer et al., 2000). The PL quenching in solid state PL spectra appears to be an integral cue that signifies efficient non-radiative channel for charge transfer between the phases of donor and acceptor (Zafar et al., 2017).

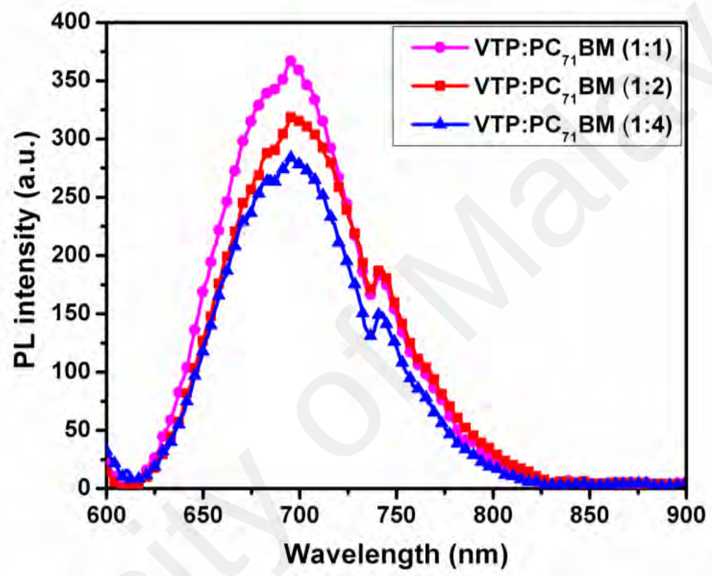

Figure 5.7: PL spectra of binary VTP:$PC_{71}BM$ at different volume ratios to investigate the quenching effect

Based on the PL spectra elucidated in Figure 5.7, increment of $PC_{71}BM$ portion within the blend films showed that the PL peaks were significantly quenched, particularly for the blend film of 1:4 volumetric ratio. The PL quenching indicated photo induction in the separation phase for 1:4 stoichiometric composition of D/A blend, which occurred closer to the exciton diffusion length (Motaung et al., 2009). Hence, the VTP:$PC_{71}BM$ blend in 1:4 volumetric ratio was applied for further analysis to fabricate OPV and OPDs.

5.4.4 AFM morphology of VTP and blended film

The AFM analyses via tapping mode were executed to assess surface morphology and surface roughness of the deposited films with 3 × 3 µm scan size for pristine materials (VTP and $PC_{71}BM$), as well as VTP:$PC_{71}BM$ blended thin film with ratios of 1:1, 1:2, and 1:4. Surface morphology has a significant function in dictating the electrical characteristics of a device. The roughness parameters that involve peak-to-valley (P-V) and root mean square (RMS) were retrieved from the AFM analysis (see Table 5.2). Based on the AFM outcomes portrayed in Figure 5.8, which denote pristine VTP and $PC_{71}BM$, the values of P-V were 1.02 and 1.43, while the RMS roughness were 0.24 nm and 0.32 nm, respectively. The RMS values were relatively low; indicating that both the organic materials possess exceptional solubility in organic solvent, particularly chloroform (Ochiai et al., 2013).

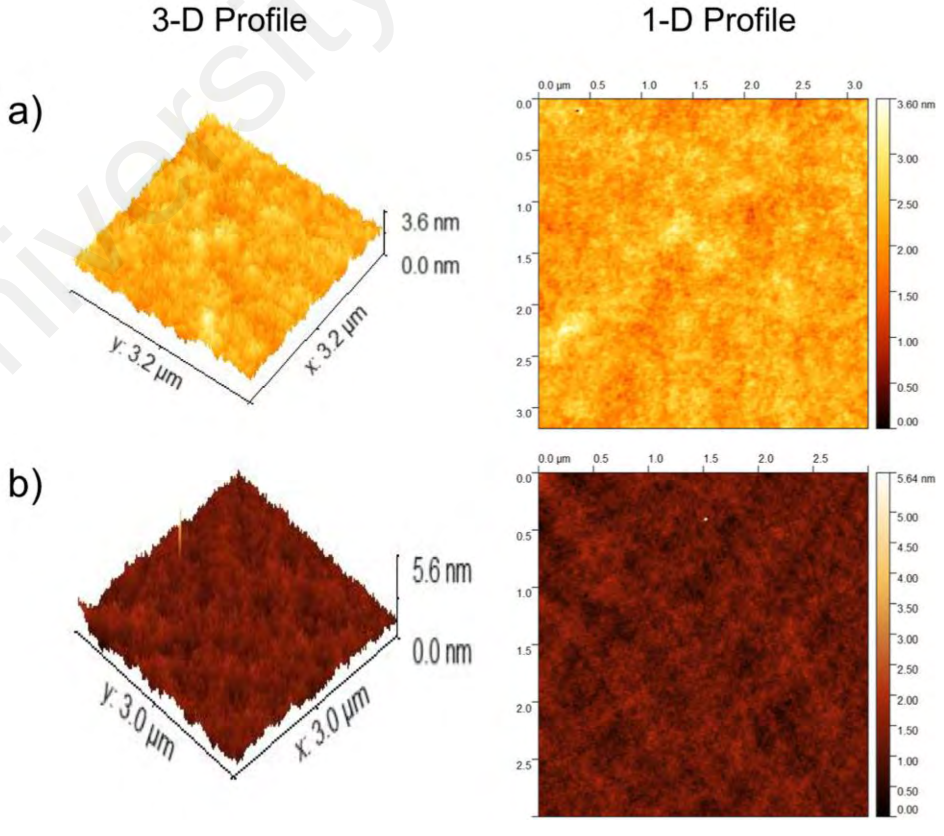

Figure 5.8: AFM images of pristine (a) VTP and (b) $PC_{71}BM$

Figure 5.9 exemplifies the surface morphology of VTP:$PC_{71}BM$ blended thin film at varied loadings of $PC_{71}BM$, which are 1:1, 1:2, and 1:4. Clearly, at lower $PC_{71}BM$ loading (1:1), the blend displayed very fine features and smoother surface than the rest, which corresponds to high miscibility that generates homogeneous films (Kannappan et al., 2012). Upon increasing the $PC_{71}BM$ loadings (1:2 and 1:4), the surfaces of the blended films appeared to be increasingly uneven, mainly due to relatively lower dispersibility that increased the P-V and RMS values (see Table 5.2) (Murugesan et al., 2015). The presence of $PC_{71}BM$, thus, may have a major role in surface roughness to result in BHJ of VTP:$PC_{71}BM$.

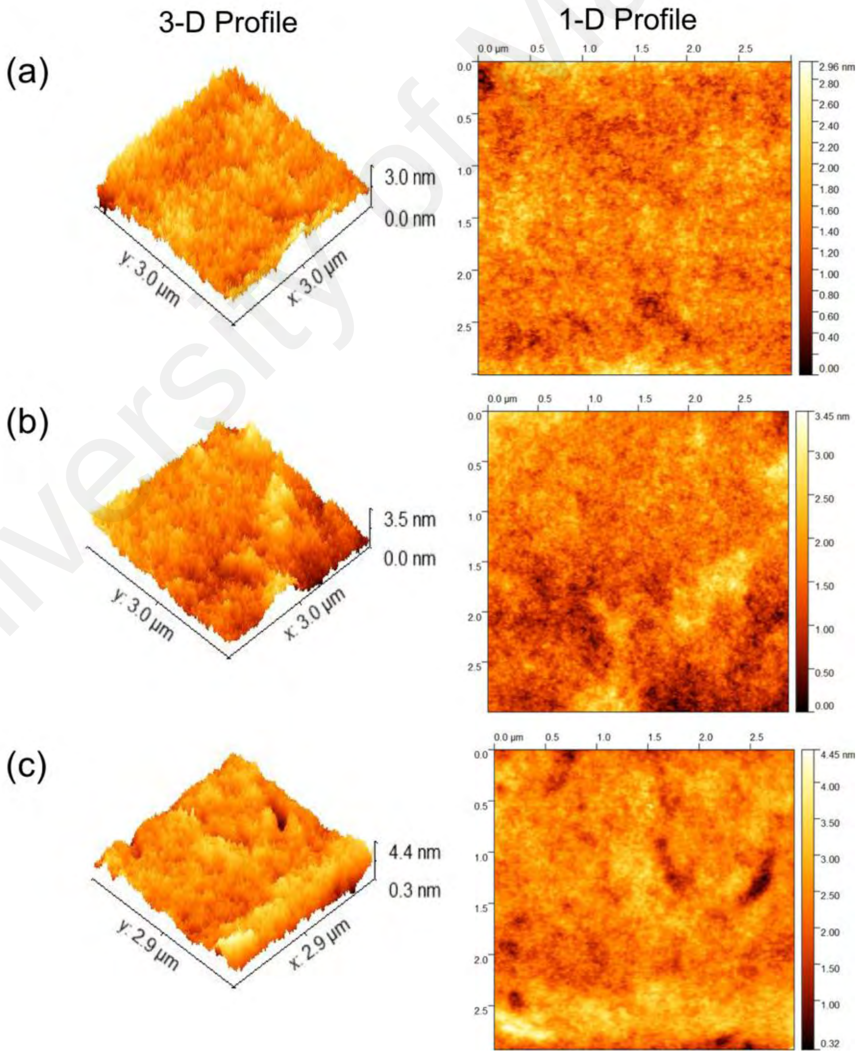

Figure 5.9: AFM analyses of (a) blend in 1:1 ratio (d) blend 1:2 ratio and (c) blend 1:4 ratio.

Table 5.2: Surface roughness parameters obtained from AFM analysis

Active layer	Peak-to-valley (nm)	Root mean square, RMS (nm)
VTP	0.31	0.24
$PC_{71}BM$	1.43	0.32
1:1	1.61	0.40
1:2	2.35	0.46
1:4	2.47	0.62

Table 5.2 displays the surface roughness parameters for pristine VTP, $PC_{71}BM$, and blended thin films with varied ratios in light of P-V and RMS. Smaller P-V and RMS values dignify thin film with smoother surface and nanomorphology. The surface roughness is closely linked with device performance, wherein higher roughness contributes to higher device efficiency. The increased contact area between organic material thin film and metal electrode may affect the charge collection at the interface of metal and organic materials (Ahmad et al., 2016; Ito et al., 2014; Wang et al., 2015).

5.4.5 Dark current-Voltage (*I-V*) characteristics of VTP and blended film of (VTP:$PC_{71}BM$)

The measurement of *I-V* characteristics in dark setting is invaluable to assess the junction properties. The crucial parameters retrieved from this analysis include ideality factor, rectification ratio (RR), reverse saturation current, barrier height, as well as shunt and series resistance. The illumination setting was excluded due to the minor fluctuations in light intensity that may generate a significant amount of noise to the device, thus the difficulty for production. As for dark *I-V* measurement, injection of charge carriers is performed using current, instead of light-generated carriers into the circuit.

Upon evaluating the stand alone VTP diode properties, Figure 5.10 showcases the semi-logarithmic plot of *I-V* curves of ITO/PEDOT:PSS/VTP/Al device, which was analyzed in dark condition and at room temperature. Based on Figure 5.10, the device displayed a rectifying behavior, which reflected non-linear and asymmetric-like diode at room temperature (300 K). The RR refers to the ratio of forward current to reverse current (I_F/I_R) at certain applied voltage. Its value relies on the bias applied, which then reflects the increased charge injection into the active layer. The RR value of the tested device was 1.6 at $\pm$ 0.5 V, which is attributable to the formation of space charge layer at the interface (Ahmad et al., 2013). The recorded RR value is comparable with MPc group, as reported in past studies (Aziz et al., 2015; Benhaliliba et al., 2014; Zafar et al., 2016).

Predominantly, as for the Schottky barrier diode, the thermionic emission theory predicts that the *I-V* characteristics at forward bias is given as follows:

$$I = I_o \exp\left(\frac{qV}{nkT}\right)\left[1 - \exp\left(\frac{-qV}{nkT}\right)\right] \tag{5.1}$$

where, I_o given as follow:

$$I_o = AA^{*}T^{2} \exp\left(\frac{-q\Phi_b}{k_B T}\right) \tag{5.2}$$

I_o denotes saturation current, V refer to forward bias voltage, Φ_b reflects zero-bias barrier height, k_B exemplifies Boltzmann constant, T represents temperature in Kelvin,

A depicts active area, and n is ideality factor of diode device. A^* signifies effective Richardson constant, which is attainable from Richardson-Dushman correlation ($A = 4\pi emk^2/h^3$) where m is the mass of electron, e is elementary charge, and h is Plank's constant. Scott and Malliaras (1999) asserted that most organic semiconductor materials are ideally found at 10^{-2}A/cm^2 K^2 (Scott et al., 1999). The reverse saturation current is obtained from the y-intercept of semi log *I-V* curve, which resulted in 0.2 nA upon weighing in its natural log.

$$\Phi_b = \frac{k_B T}{q} \ln(\frac{AA^*T^2}{I_o}) \tag{5.3}$$

The effective barrier height of junction Φ_b was obtained from Equation 5.3, which refers to the contact present between the metal and semiconductor interface. This was calculated using Equation 5.2 with the value of reverse saturation current at 0.673 *eV*.

The conformity of diode device to pure thermionic emission was determined by incorporating the ideality factor, n, by using the same semi log *I-V* characteristics. For an ideal diode, the n value reflects unity, despite it deviating from its ideal value at times, wherein the observed value is greater than unity. The value of ideality factor in this study was obtained from the slope of the linear region in forward bias of semi-log *I-V* curves using the following equation:

$$n = \frac{q}{kT} \frac{dV}{d(\ln I)} \tag{5.4}$$

The ideality factor recorded in this study is 2.93. The n value exceeded ‘2’ due to the following reasons: non-homogeneous barrier, non-homogeneous thickness of organic film, temperature (Al-Ta’ii et al., 2016), and the prevalent current in single junction photovoltaic device because of recombination (Yakuphanoglu, 2007). Prior studies reported that the ideality factor of Pc derivatives, such as CuPc, MgPc, and AlPc, is massive primarily due to recombination issues (Benhaliliba et al., 2014; Rajaputra et al., 2007).

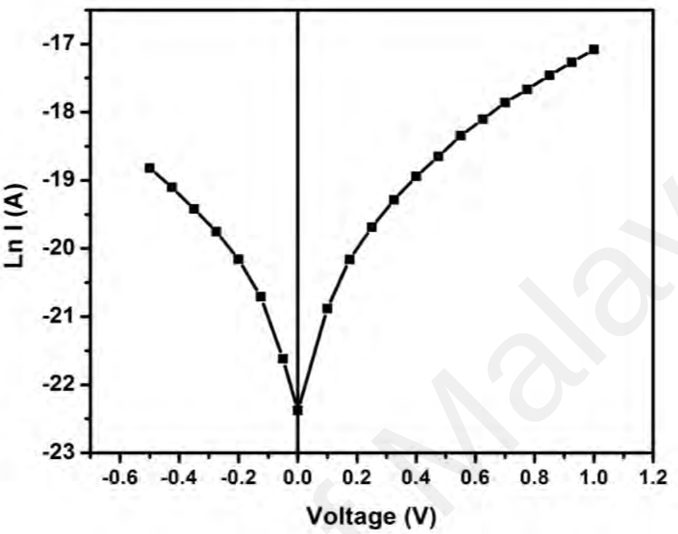

Figure 5.10: Current-voltage characteristics of VTP-based solar cell in semi-logarithmic scale

The shunt and series resistance (*R_{sh}* and *R_s*, respectively) are essential factors that dictate the performance of a device. These resistance values are obtained from the plot of junction resistance, R_J, versus voltage, *V*; $R_J = \frac{dV}{dJ}$. Massive shunt resistance is required to decrease leakage of current via cells (e.g. pinholes), apart from suppressing the recombination of charge carrier at the device interface (Ito et al., 2014; Murugesan et al., 2015; Servaites et al., 2011). This scenario, however, contradicts the low series resistance that reflects internal resistance, which allows and enhances high current to flow through the device, whereby low R_s denotes low resistivity of the organic material (Khan et al., 2011; Lim et al., 2016).

Figure 5.11 illustrates that the values of shunt resistance, R_{sh}, and series resistance, R_s, can be retrieved from the graph of junction resistance (R) versus voltage (V). Obviously, the resistance decreased exponentially with increment in forward bias. The R_{sh} corresponded to the resistance within the vicinity of zero bias, thus resulting in 745 Ω/cm^2. The R curve was saturated upon continuous supply of forward bias. Therefore, the applied external electric field compensated for the rectifying potential barrier between cathode and anode, whereby the current that flowed through the device was restricted by R_s. Hence, the R_s value was deduced by extrapolating the saturated part of the R curve towards the interception with resistance axis, in which the result was recorded at 32 Ω/cm^2 (Brus et al., 2016).

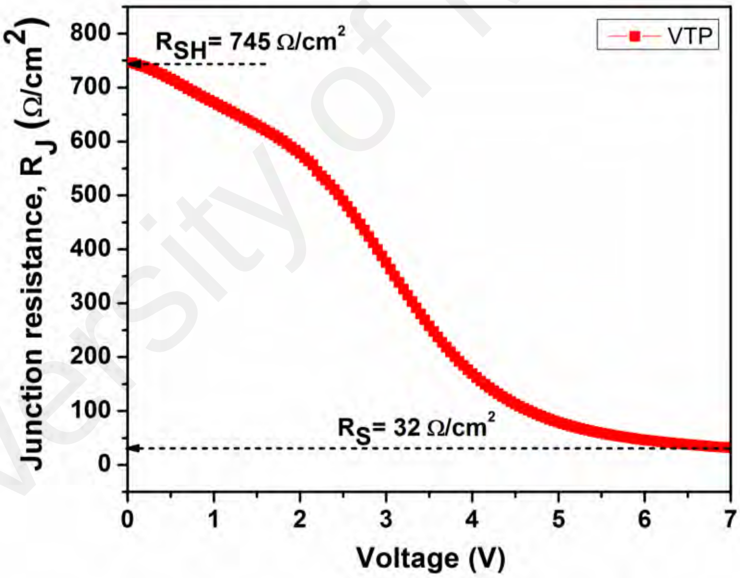

Figure 5.11: Junction resistance versus biased voltage for single junction VTP device

A similar analysis was executed for the blended film to determine its R_{sh} and R_s, as exhibited in Figure 5.12. Meanwhile, Table 5.3 tabulates the estimated values of both shunt and series resistance values of all diode devices. As a result, the value of R_s decreased from 19.40 to 10.47 and to 7.42 Ω/cm^2 by increasing the concentrations of PC$_{71}$BM, respectively. This reduction reflects the increasing surface roughness morphology of the highest doping $PC_{71}BM$ (see Figure 5.8), mainly because the R_s value is closely related to active layer morphology, intrinsic resistance, and thickness of active layer (Murugesan et al., 2015). The processing additives improved the device performance by dissolving the aggregates of $PC_{71}BM$ in VTP:$PC_{71}BM$ matrix. This facilitates the integration of $PC_{71}BM$ molecule into the VTP, thus resulting in a greater donor-acceptor interface. The enhanced surface interface between D/A in the active layer contributes to improved migration of exciton between the interface, and favorable charge separation. It is noteworthy to highlight here that R_{sh} is correlated with pin holes and traps that are present in the thin film morphology, hence causing charge carrier recombination and current leakage. Based on Table 5.3, the R_{sh} value increased from 1636.12 to 1724.40, and finally, to 3838.74 Ω/cm^2 with increment of $PC_{71}BM$. The increase noted in R_{sh} value reflects that the incorporation of $PC_{71}BM$ in the active layer generated additional percolating pathways that helped the charge carriers to diffuse at a longer distance, and finally, minimize PL activity (see Figure 5.5) (Muhammad et al., 2017; Murugesan et al., 2015).

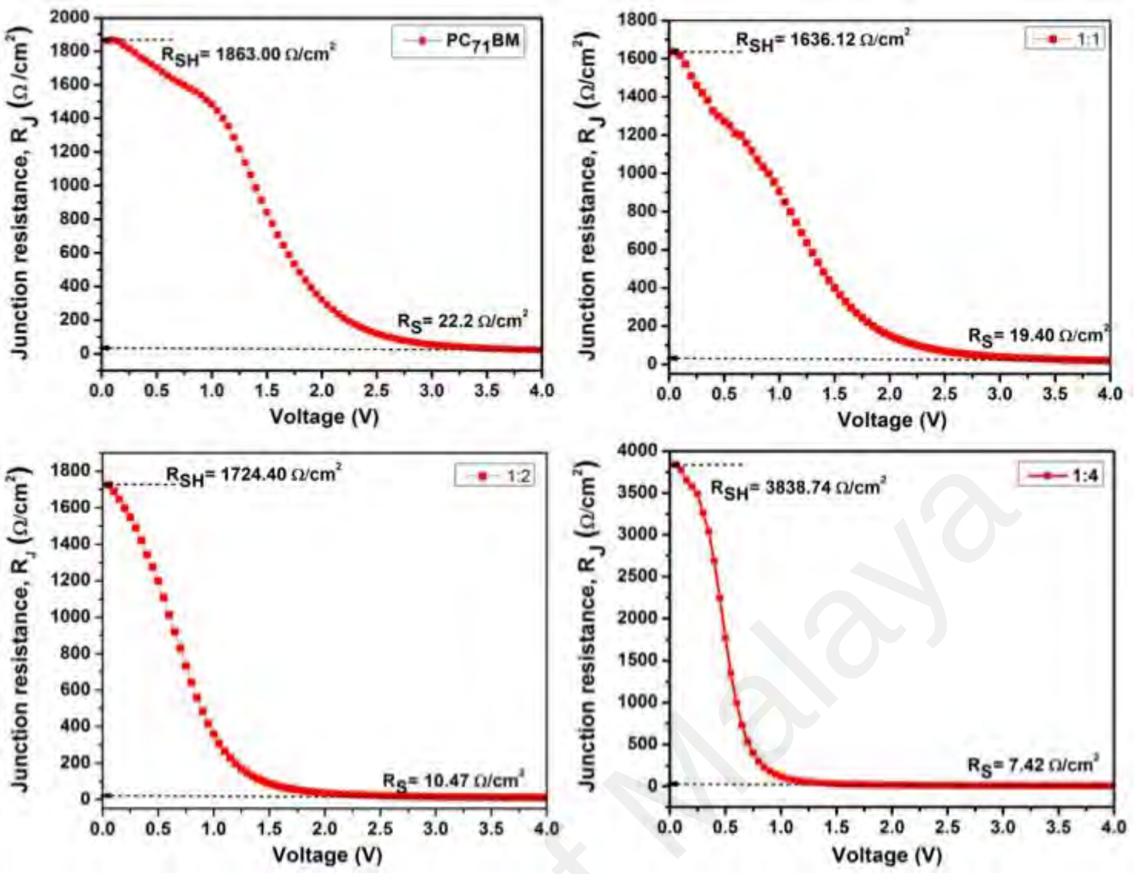

Figure 5.12: Junction resistance versus biased voltage for $PC_{71}BM$ and blended thin films of diode devices

Table 5.3: Extracted R_s and R_{sh} values from junction resistance versus biased voltage

Resistance (Ω/cm^2)	VTP	$PC_{71}BM$	1:1	1:2	1:4
R_{series}, R_S	32.00	22.20	19.40	10.47	7.42
R_{shunt}, R_{SH}	745.00	1863.00	1636.12	1724.40	3838.74

Studies pertaining to charge transport in organic thin film devices can be classified into two types: charge carrier injection at the interface, and charge carrier transport in the bulk system. The characterization of the forward bias *I-V* curves in dark condition yielded significant characteristics in light of transport mechanism, which is responsible for the conduction process that took place at the electrode interface. Here, the effective carrier mobility for all devices had been determined by adopting the space charge-limited conduction (SCLC) approach with positive voltage up to 10 *V* in dark condition. Figure 5.13 displays current density versus voltage curves excluding illumination, which was re-plot in double logarithmic scale to identify the mechanism that dominates the transport charge in VTP diode. It is common for the double log forward bias *J-V* to reveal the power law behavior of $J \sim V^m$, where m denotes the slope of each region. The *m* value varies with the injection level and is linked with the distribution of trapping centres. The $m = 1$ region reflects the ohmic region, while $m = 2$ is SCLC region, and $m > 2$ represents trapped charge limited current region (Chiguvare et al., 2003).

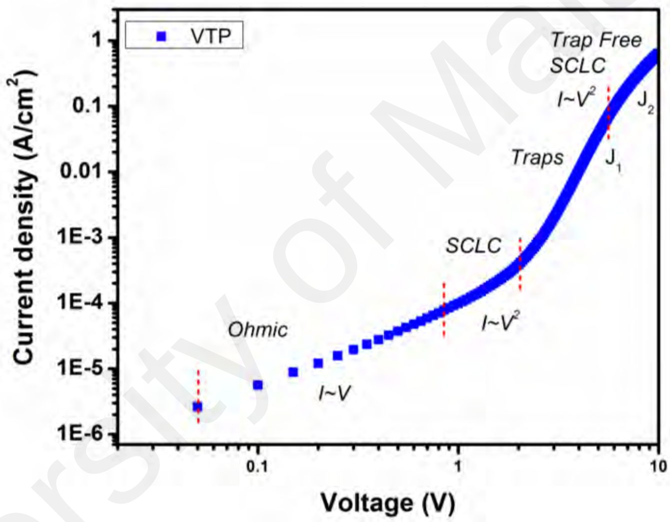

Figure 5.13: The double log scale of *J-V* characteristics of VTP-based diode device measured in dark condition

Figure 5.13 illustrates the characteristics of VTP-based diode device to comprehend the conduction mechanism. The double logarithmic graph is distributed in four regions (marked with dotted red lines) with various regions having varied slopes; ohmic, SCLC, traps, and trap-free SCLC regions (TF-SCLC). At low voltage region, the slope was ~1.2; signifying ohmic conduction mechanism. Here, the current increased slowly with the applied voltage as the injected effective charge carrier density was lower than the background thermal carrier density (Missoum et al., 2016). In region 2 (intermediate voltage range), the conduction mechanism of the device was dominated by SCLC, wherein the slope was ~2.08. In this scenario, the voltage was more significant than that of region 1. The density of injected free charge in this region was higher than the thermally-generated free charge carrier density, hence the increment in current. Typically, the formation of SCLC is attributed to the low mobility of charge carriers in organic thin film, thus localizing the injected carriers by the trap states to limit the carrier conduction of the device (Shang et al., 2006). The presence of traps was due to structural defects that derived from non-uniformity and sub-atomic structure of the VTP layer. Under such conditions, the mobility of charge carriers for VTP diode devices was determined using the following equation:

$$J = \frac{9}{8}\varepsilon\varepsilon_O\mu(\frac{V^2}{d^3}) \tag{5.5}$$

where, J reflects current density, V is voltage, d denoted active cell thickness, ε represents permittivity of free space, ε_O signifies relative dielectric constant ($\varepsilon_O = 8.854 \times 10^{-12}\ Fm^{-1}$), and μ stands for charge carriers mobility. Table 5.4 shows the estimated charge carrier mobility.

Next, the exponential increase of current in region 3 at higher voltages gave the slope ~5.6. This condition was dominated by the TFL mechanism, whereby all deep traps were completely filled by the injected electrons, hence making the existing trap sites fully occupied. As for region 4, where high voltage was applied, the slope of the plot decreased sharply (~3.5) as the diode device approached the TFL at high injection level. At high injection level, the conduction mechanism was similar to that in TF-SCLC. Here, the injected carriers occupied most of the traps and accumulation of space charge near the interface electrode culminated in the generation of a field that hindered further rejection. The VTP diode between the interfaces contact functioned as if there was no trap in it and the current varied with the square of the voltage (Gullu et al., 2008; Janardhanam et al., 2014; Jomaa et al., 2006). The estimated current density in this region is expressed via Child's law (Khan et al., 2011; Najeeb et al., 2016):

$$J = \frac{9}{8}\varepsilon\varepsilon_O\mu\theta(\frac{V^2}{d^3}) \tag{5.6}$$

where, θ denotes the trapping factor defined as (J_1/J_2), in which J_1 and J_2 are the initial and final values of current density in TF-SCLC region, as portrayed in Figures 5.13 and 5.14, respectively. Figure 5.14 portrays the similar analyses applied for the rest of the thin films, while Table 5.4 summarized the estimated values of charge mobility for all the diode devices.

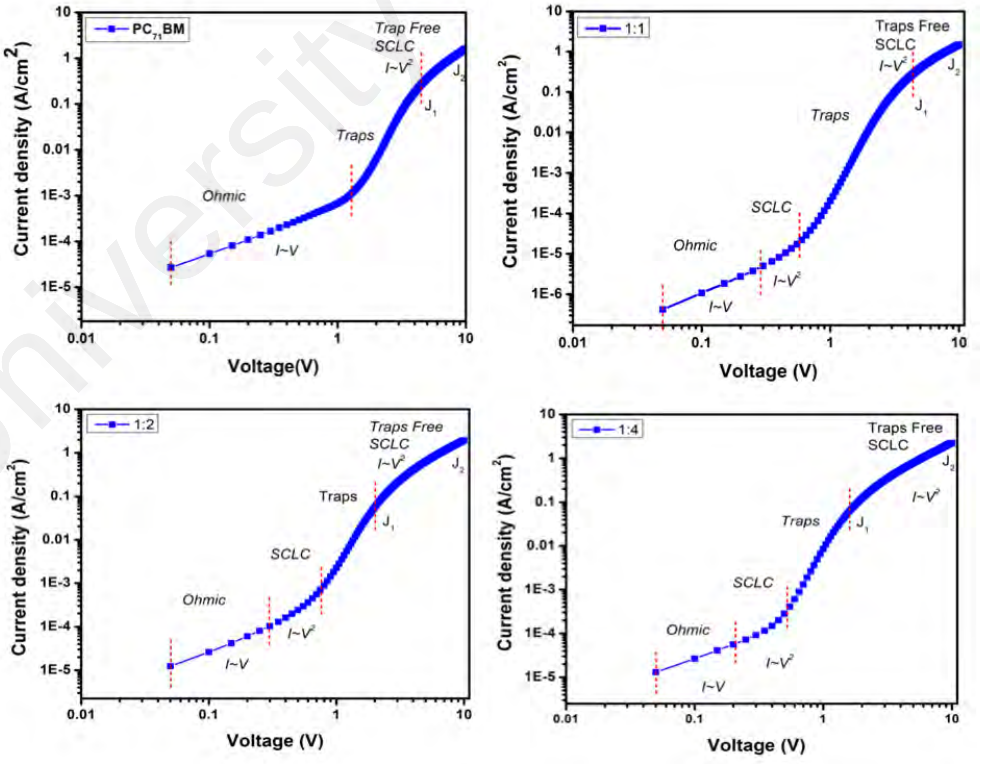

Figure 5.14: The double log of *J-V* characteristics of $PC_{71}BM$ and blended film measured in dark condition

Table 5.4: Extracted mobility (cm^2/Vs) values for VTP, $PC_{71}BM$ and its varied ratios from diode measurements

REGIME / OPVs	SCLC	TF-SCLC
	Mobility (cm^2/V.s)	Mobility (cm^2/V.s)
VTP	4.24×10^{-7}	5.00×10^{-5}
$PC_{71}BM$	–	1.20×10^{-4}
1:1 (VTP:$PC_{71}BM$)	2.02×10^{-7}	7.06×10^{-5}
1:2	1.07×10^{-6}	7.55×10^{-5}
1:4	2.38×10^{-6}	7.63×10^{-5}

5.4.6 Current-Voltage (*I-V*) performance of VTP-based optical devices

Figure 5.15 shows the *I-V* performance in dark and under light settings for ITO/PEDOT:PSS/VTP:$PC_{71}BM$/Al photovoltaic device. The photovoltaic characteristics, such as J_{SC}, V_{OC}, *FF*, and PCE (η), are portrayed in Figure 5.15.

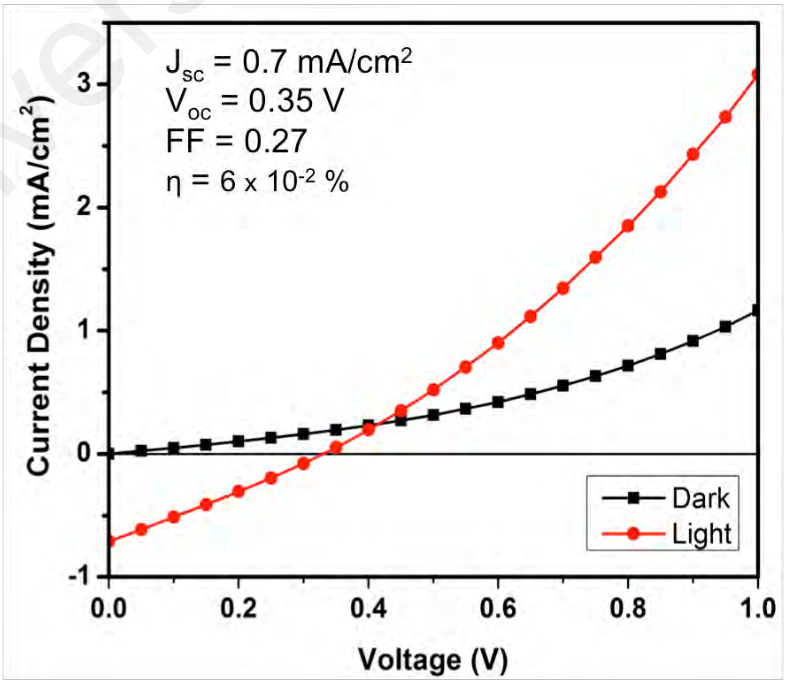

Figure 5.15: The *J-V* characteristics of ITO/PEDOT:PSS/VTP:$PC_{71}BM$/Al photovoltaic device under 100 $mWcm^{-2}$ illumination

The efficiency displayed by the device is attributable to the increased charge generation that relies on the broader absorption range. Another factor that contributed to the efficiency in performance is the dissociation of excitons in VTP:$PC_{71}BM$ device due to the BHJ system. This condition limits the single layer and bilayer solar cells, primarily because the typical travel path of carriers is below 20 nm prior to recombination (Cai et al., 2010). This particular blend system yielded efficiency up to ~0.06 %. This is perhaps due to low absorption intensity (see Figure 5.5) within the visible range spectrum, which is insufficient to enhance charge separation, thus contributing to the low conversion from light energy to electrical energy. This corresponds to the low charge carrier mobility displayed by the device. In studying the potential use of VTP in optical device, the VTP:$PC_{71}BM$ was extended and this resulted in the OPD device. The presence of extended ligands in the macrocycle of VTP was expected to improve the sensitivity of the photodetector to yield a good device.

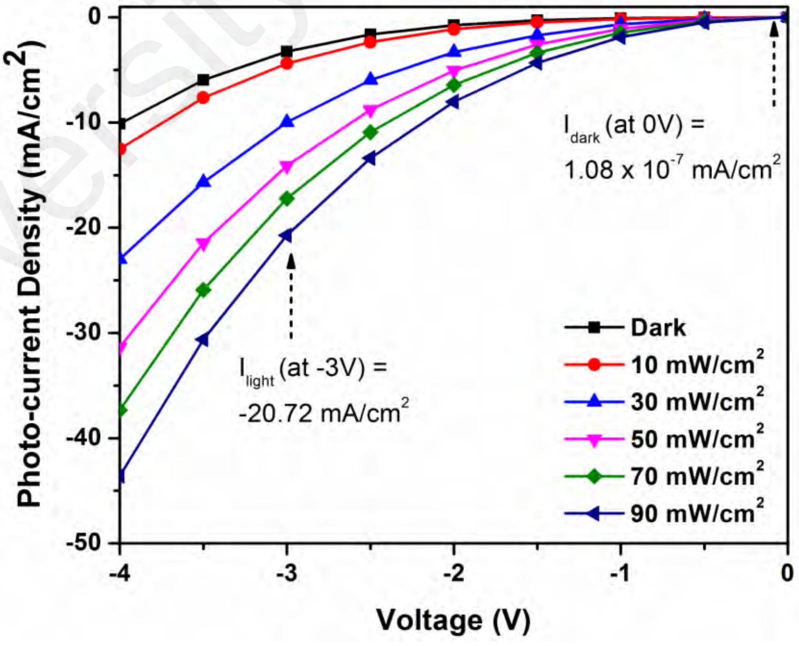

Figure 5.16: Photocurrent density-voltage characteristics of ITO/PEDOT:PSS/VTP: $PC_{71}BM$/Al photodetector device

The electrical performance of ITO/PEDOT:PSS/VTP:$PC_{71}BM$/Al photodetectors was characterized using varied light intensities. Figure 5.16 discloses that the photocurrent density in dark condition (I_{dark}) was relatively low, while more pronounced with increasing simulated light illumination (I_{light}). Increment in photocurrent appeared to be concomitant to the increasing change in photon density at varied light intensities. Meanwhile, the dark current was governed by the charge injection from the contacts into photoactive layer, as well as thermally-generate charge carriers in D/A interface (Wang et al., 2014). Based on Figure 5.16, the photocurrent value (I_{light}) under 90 mW/cm^2 at -3 V was -20.72 mA/cm^2, while the dark current (I_{dark}) was 1.08×10^{-7}mA/cm^2. Hence, the I_{light} / I_{dark} parameter was calculated as 1.91×10^5. The -3 V was selected to compare the value of I_{light} / I_{dark} with past studies, whereby VTP:$PC_{71}BM$ has been proven to possess higher I_{light} / I_{dark} value than the rest (Zafar et al., 2015; Zafar et al., 2015). As depicted in Section 2.4.2 (see Chapter Two) in the characteristics of organic photodetector, higher value of photo to dark current ratio is required for better noise rejection ability.

Figure 5.17 illustrates the alterations of photocurrent for varied voltages in VTP:$PC_{71}BM$-based photodetectors. The reverse biased photocurrent density displayed a distinct upsurge in the negative direction along y-axis, which increased the short circuit current under illumination. The photocurrent-illumination correlation portrayed a good linearity for each applied voltage. The alteration in photocurrent relies on the illumination, which is expressed as follows:

$$I_{light} = AF^{\alpha} \tag{5.7}$$

where, I_{light} refers to photocurrent, F denotes light intensity, A represents constant, and α is an exponent. The α value can be retrieved from the slope of photocurrent against light intensity graph. The expression of the change in photocurrent depends on light illumination: $J \propto F^{\alpha}$ where J_{light} signifies current density under illumination, F denotes light intensity, and α is an exponent, as determined from the slope of log photocurrent versus log of light intensity curves. For instance, the exponent value at 0.5 shows that the photocurrent increases in a sublinear manner to indicate bimolecular recombination of independent and oppositely charged carriers. When the exponent is 1, the correlation between photocurrent and light intensity is linear; reflecting monomolecular recombination (Zafar et al., 2015). The detector may exert exceptional sensitivity at higher voltage bias due to two possible reasons; i) the extended absorption bandwidth held by composite blend thin film improves the charge generation, and ii) the external field offers efficient charge transport to the respective electrodes prior to recombination (Zafar et al., 2016).

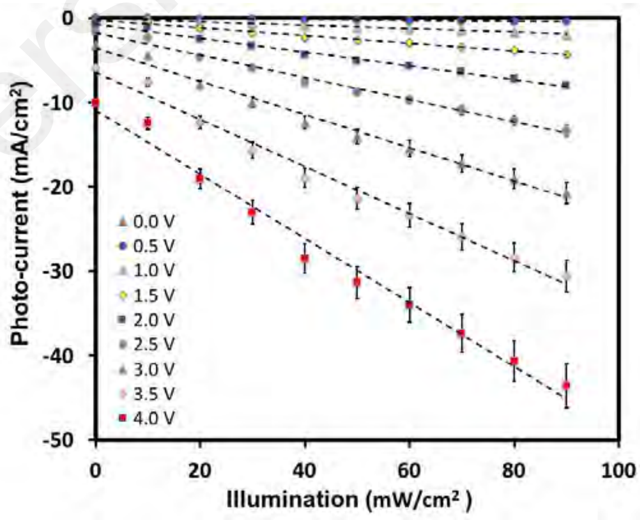

Figure 5.17: Photocurrent vs. illumination intensity under various applied voltage for ITO/PEDOT:PSS/VTP:PC$_{71}$BM/Al photodetector device

Figure 5.17 displays improvement in photon absorption and dissociation of exciton due to the BHJ blend system. The migration of separated charge carriers to the respective electrode relies on the external force. This external force serves as a transport to drive the charges via interpenetrating D/A networks. Figure 5.17 portrays enhanced photoresponse due to the efficiency of charge carriers at higher order potential bias. The mobile charge carries, at lower potential bias, undergo recombination or get trapped, instead of being collected at the electrodes.

The present case of OPD at unbiased condition showed that the exponent value was 1.18, which reduced to 0.77 and 0.55 at 2 and 4 *V*, respectively (see Figure 5.18). The decrease in the exponent value portrays enhanced hole/electron mobility at higher degree of bias, as depicted by (Hamwi et al., 2011).

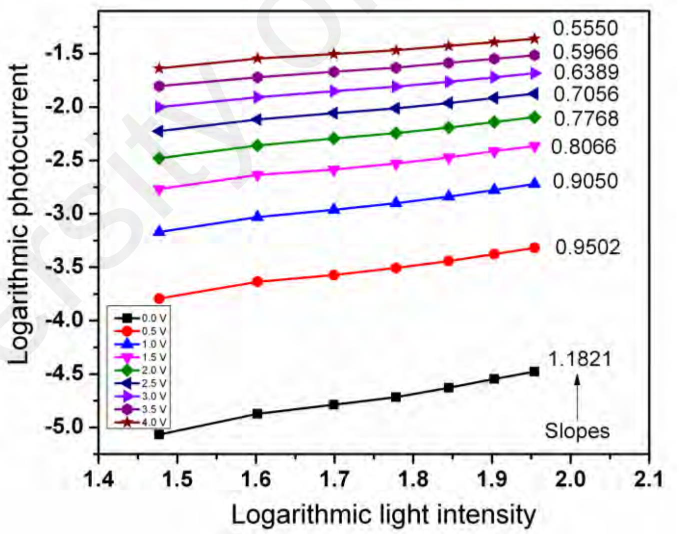

Figure 5.18: Estimation of 'α' exponent by logarithmic photocurrent density vs log scale optical power density at varied forward biased conditions

Figure 5.19 illustrates the photoresponse behavior of the photodetector when the light was controlled to be periodically turned in 'ON' and 'OFF' states. Characterization was performed by recording the changes in photocurrent as a function of time with the presence (ON) and absence (OFF) of light at 100 mW/cm^2 under 1*V* bias voltage. A four-cycle plot was recorded under ON/OFF illumination to reveal that the sensor exhibited exceptional photoresponsivity with consistent response, good repeatability, and rapid change of states. The photoresponsivity of the sensor was calculated by using the following equation:

$$R = \frac{J_{ph}}{P} \tag{5.8}$$

where R denotes responsivity, J_{ph} is photocurrent density at -3 V (see Figure 5.16), and P reflects the power of incident light intensity. The sensor responsivity value was 2.07×10^{-1} A/W.

The rise time, t_r (time for which device response rises from 10 to 90%) and fall time, t_f (time for which device response decreases from 90 to 10%) at ~350 ms and ~400 ms, respectively, appeared similar for all six tested devices.

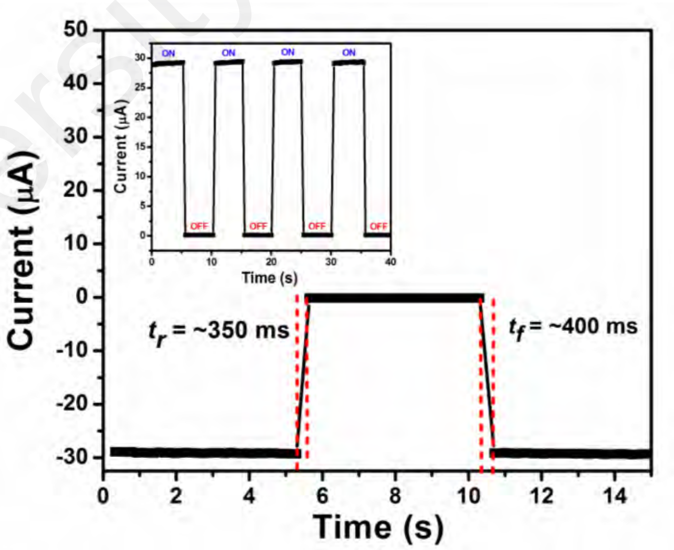

Figure 5.19: The change of photocurrent response under light (ON) and in the dark (OFF)

To date, the EQE values of OPDs have been reported to be lower than unit, which adheres to the photovoltaic working mechanism. Hence, the potential application of photodiode type photodetector is restricted by low EQE. Figure 5.20 portrays EQE versus wavelength, which reveals the wavelength-dependent gain of the device (An et al., 2009; Li et al., 2015). This was measured by adopting the IPCE system. This characterization coincides with the absorption profile of the composite film. This can be cross-referenced, as the EQE spectrum of VTP:PC$_{71}$BM OPD covers detection ranging from 300 nm to 600 nm; making it a promising candidate for photodetector application, in comparison to its VTP counterpart.

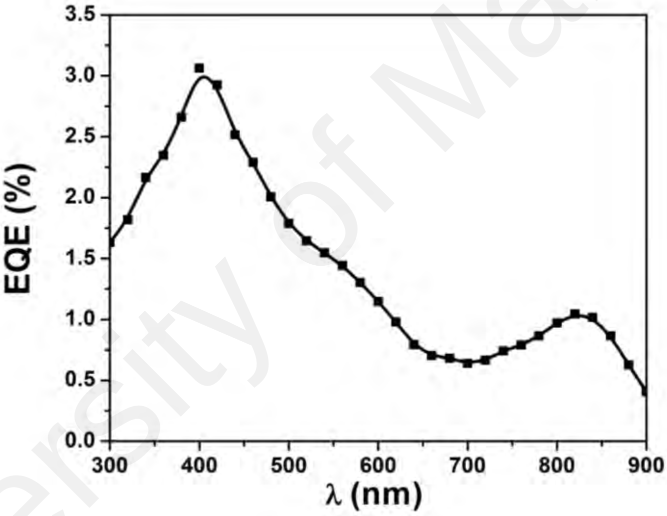

Figure 5.20: The external quantum efficiency (EQE) of the ITO/PEDOT:PSS/VTP:PC$_{71}$BM/Al photodetector

Table 5.5 presents the comparison of key photosensing parameters of the fabricated OPD with those reported in the literature. The fabricated OPD device displayed more significant performance than those reported in prior works. The outcomes are attributed to the extended ligands on the molecular structure of VTP that may enhance the sensitivity of photodetector.

Table 5.5: Comparison of the sensor parameters at -3 *V* biasing

Type of organic photodetector	I_{ph} / I_{dark}	Responsivity	Response and recovery	Reference
MEH-PPV:VoPcPhO	1.08	5×10^{-4} mA/W	~4 s both	(Zafar et al., 2014)
PFO-DBT:MEHPPV: $PC_{71}BM$	3.5×10^{4}	3.9 mA/W	~800 and ~500 ms	(Zafar, Ahmad, et al., 2015)
VTP:$PC_{71}BM$	1.91×10^{5}	2.30×10^{-1}A/W	~350 and ~400 ms	Current work

5.5 Summary

A new composite blend of VTP:$PC_{71}BM$ is proposed in this study to assess the potential application of optical devices; OPV and OPD. Nevertheless, considering its achievement in light of efficiency (0.06%), the device failed to meet the sufficient power conversion amount for real energy harvesting application as a commercial solar cell. The organic photodetector device displayed enhanced sensing performance, which is attributable to the suitable selection of donor and acceptor components, represented by VTP and $PC_{71}BM$, respectively. In addition, this significant performance might be due to the extended ligands that presence on the VTP molecular structure which makes it has high photosensitivity. The result showed photoresponsivity of 2.30×10^{-1}A/W and fast response time of 350 ms, which appear practical for light sensing application. The study outcomes are expected to pave the path for the use of VTP in photo-sensing application below 650 nm. Nonetheless, further enhancement is demanded on the architecture of the detector in light of practical use in vast applications.

CHAPTER 6: VTP BASED ORGANIC HUMIDITY SENSOR DEVICES

6.1 Introduction

This chapter presents the effects of various active layer thicknesses (66 ± 5 nm, 80 ± 5 nm, and 90 ± 5 nm) on the electrical properties of VTP-based capacitive humidity sensor. In doing so, characterization of structural and film wettability was executed to ascertain that the mechanism of humidity sensing properties in the sensor is well understood, as well as to establish a controlled production situation. Lastly, by employing the solution processed spin coating, the sensor devices were fabricated in the planar geometry of Al/VTP/Al, with capacitance as a function of relative humidity levels of $1V$ input to determine the key performance of the organic humidity sensor (viz. sensitivity, hysteresis plot, and response & recovery).

6.2 General review on organic semiconductor-based humidity sensors

At present, much emphasis has been given on the application of organic semiconductors in electronic devices. This is due to the promising benefits of their cost efficiency, lightweight, simple fabrication (via spin coating and drop casting), and non-toxic nature. These advantages have urged researchers to investigate a wide range of potential applications in place of the ubiquitous conventional inorganic semiconductors in electronic devices, such as OLEDs, OPVs, OFETs, junction diodes, and sensors (Azmer et al., 2016; Raza et al., 2016; Rittersma et al., 2002; Roslan et al., 2018; Wang et al., 2013; Zhou et al., 2013).

Based on the extensive evaluation depicted in the literature, humidity sensors hold an imperative role in a plethora of domains. Studies pertaining to potential organic humidity sensor applications have been undertaken by several groups to offer indication of moisture levels and air temperature in the environment. A range of aspects have been studied; detecting and monitoring the applied humidity in medical equipment, agriculture stations, and meteorology stations to report and predict the weather. The excessive amount of water vapor or humidity in the surrounding can affect a number of chemical, biological, and physical processes in industries or in one's daily life. Therefore, humidity sensor is pivotal to monitor the environment and for industrial purposes, due to its impact on production cost, health, and personnel safety. Useful capabilities of humidity sensors to work efficiently in a wide range of applications have been noted and have opened a new spectrum, depending on certain alluring factors, such as low fabrication cost, fast response and recovery time, good humidity sensing range, good durability over a long lifespan period, chemical and physical stability, as well as resistance against contamination. Low power utilization in humidity sensor enhances efficiency and performance (Ahmad et al., 2008; Lee et al., 2004).

Humidity sensor can be broadly classified based on the parameters applied in measuring humidity. For instance, one may employ capacitive sensing principle, while another may use resistive effects. The capacitive-based humidity sensors are most widely used, when compared to resistance-based sensors. This is mainly due to low power consumption (Rittersma, 2002), better linearity, and good stability at higher humidity and temperature (Ahmad et al., 2008) exerted by the capacitive-based humidity sensors. As such, this study fabricated capacitive-based humidity sensors made of organic materials to serve as the active layer. The sensors adhered to the principle that the thin organic film was sandwiched between a pair of metallic electrodes to generate a small capacitor.

Of the vast types of organic materials, particularly for humidity sensor application, MPcs with a range of macro-ring substituents and derivatives have been extensively studied (Aziz et al., 2010; Ho et al., 2001; Roslan et al., 2018). The MPcs have been recorded to possess good thermal and chemical stability, as well as being non-toxic. The sensing performance of MPc-based humidity sensors relies on a number of conditions, namely sensing film thickness, film synthesis method, film morphology, sensing film temperature, and film annealing (Lee et al., 2004). A well-known MPc derivative refers to VOPcPhO, which is a *p*-type organic semiconducting material, in which its electrical properties can alter in a humid setting. The conductivity of such organic materials can be influenced by the generation of hole carriers induced by the formation of charge transfer complexes at Pc surfaces (Karimov et al., 2017). Aziz et al., (2010) proposed the VOPcPhO thin film for humidity sensors application and successfully fabricated Ag/VOPcPhO/Ag capacitive humidity sensors. The study reported the effects of various sensing film thicknesses on the device performance, wherein the sensitivity of the device performance depended on the thickness of the VOPcPhO film.

This present study builds on prior experience, as depicted above, to assess the use of another type vanadium derivative, namely VTP, in capacitive-based humidity sensor. The novelty of this present study lies in investigating the varied substituents in the macro-ring of the main Pc body, in comparison to that of VOPcPhO. The identified thickness of the VTP as the active layer of film is a significant feature by fabricating and analysing its properties. That being mentioned, an exploratory investigation was executed in light of humidity sensor application.

6.3 Experimental procedures

Commercial VTP powder (empirical formula: $C_{56}H_{68}N_{12}OV$) was purchased from Sigma Aldrich (St. Louis, CA, USA). Figure 6.1 illustrates the variances between the molecular structures of (a) VTP with extended ligands on the macro cycle ring, in comparison to that of (b) VOPcPhO.

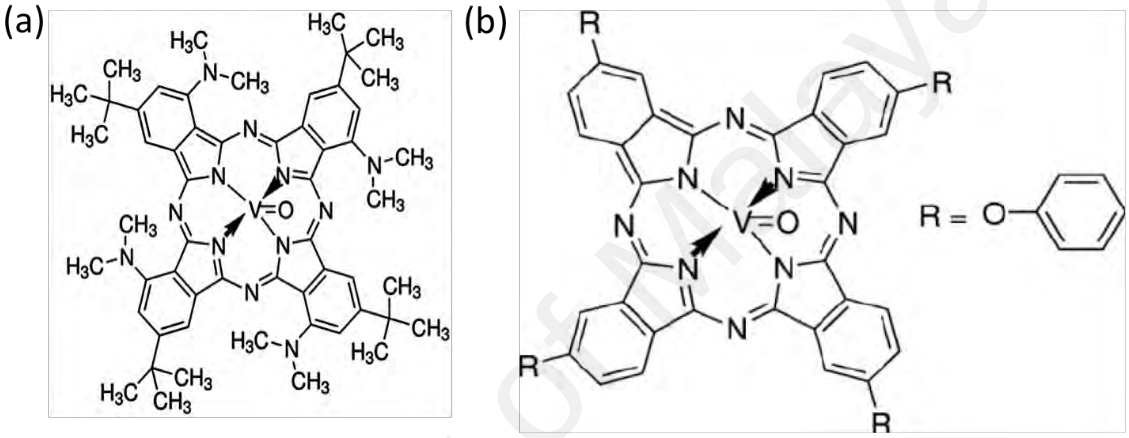

Figure 6.1: Variation in the molecular structures of (a) VTP (Roslan et al., 2018), and (b) VOPcPhO (Abdullah et al., 2012)

Prior to the fabrication process, 25 × 25 mm glass substrates were thoroughly cleaned in acetone, ethanol, and deionized water (15 min for each step) via sonication. After the cleaning process, the glass substrates were dried in a dust-free environment by passing nitrogen gas. The VTP solution (10 mg/mL) was prepared by dissolving 10 mg of VTP powder in 1 mL of chloroform. Prior to deposition of VTP thin film, a 100 nm Al electrode distanced by 40 μm gap was thermally-deposited onto a glass substrate in an Edward AUTO 306 thermal evaporator. The pressure within the vacuum chamber was retained at 10^{-5} mbar during the evaporation process. The VTP thin film was spin coated at three spin speeds (500, 1000, and 2000 rpm) for 30 s on the prepared Al thin film to assess the impact of thicknesses on the structure and performance of the sensors.

Figure 6.2 illustrates the cross-section of the fabricated capacitive-based humidity sensors.

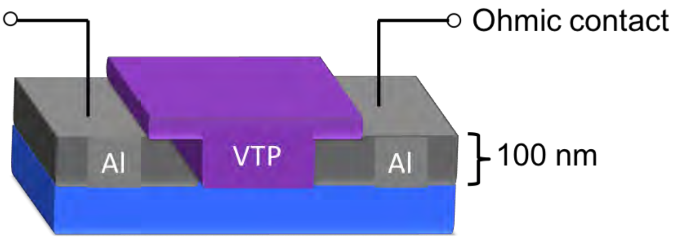

Figure 6.2: A cross-sectional view of the thin-film humidity sensor

The elemental composition of VTP thin film was assessed with XPS (PHI Quantera II) system, along with PES beamline BL3.2 in SLRI located at Thailand. A Thermo VG Scientific CLAM2 electron spectrometer was equipped with PES system and operated at a maximum photon energy of 600 *eV* with an energy step of 0.1 *eV* setting. The binding energy spectra were calibrated against C1s peak at 284.6 *eV*, which is attributable to the adventitious carbon that displays unavoidable presence in all air-exposed materials.

The structural properties of VTP thin film were examined using Raman spectroscopy (RENISHAW Raman Microscope) instrument with 514 nm laser source wavelength. Additional to and isolated from this investigation, the wetting behavior of VTP thin films was evaluated at ambient temperature using contact angle (C_A) measurement system in the air, where 1 μL of water droplets were carefully dropped onto the surface of the thin film. The average C_A value was retrieved at three positions on the same sample using SCA20U software program.

Next, the performance of the device was examined using a custom-made humidity chamber with controlled RH value. A commercially available Testo 625 thermohygrometer and Rossmax NB80 humidifier were employed to measure the RH levels and the water vapor content in the chamber, respectively. The sensing output was determined by using an LCR meter (GW Insterk LCR-829). The humidifier introduced humidity in the chamber, which was later removed by passing nitrogen gas to provide a dry environment in the chamber. Electrical characterization of the humidity sensors was carried out under a constant frequency of 0.5 kHz with a constant voltage bias of 1 *V*. All measurements were recorded at room temperature (27 °C). Figure 6.3 illustrates the set-up of custom-made humidity chamber. The thicknesses of all films were measured using a KLA Tencor Surface Profilometer (model P-6 Stylus Profiler). Both surface roughness and grain size of the samples were characterized using Atomic Force Microscopy Hitachi AFM5100N (SI-DF3 cantilever) with 3 × 3 µm scan rate.

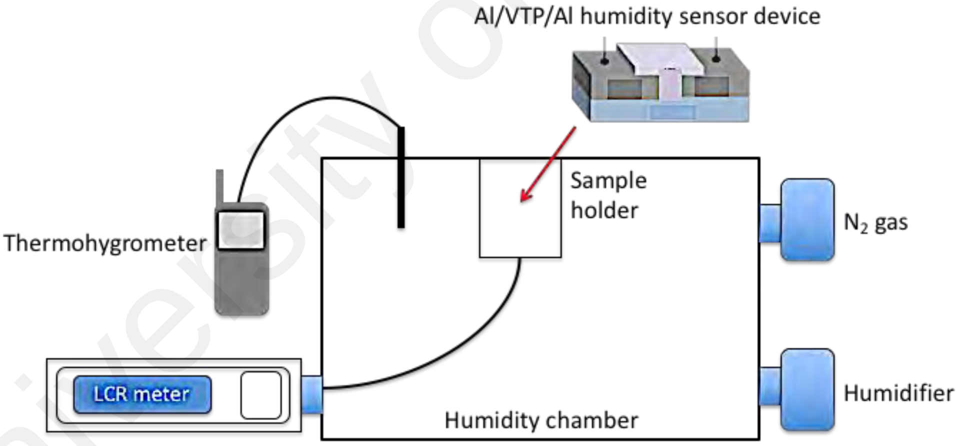

Figure 6.3: The set-up of custom-made humidity sensor

6.4 Results and Discussion

6.4.1 Elemental study of VTP molecular arrangement

Figure 6.4 illustrates the schematic diagram of a VTP molecule, where the C sites are marked as C_1 to C_4; three C sites represent benzene ring, while one C site reflects the inner pyrrole ring. The XPS was applied to assess the elemental composition of the electronic structure of the VTP thin film (see Figure 6.4). Figure 6.5(a) displays the wide-scan spectra of the VTP thin film, which detected the expected elements, namely vanadium (V), nitrogen (N), oxygen (O), and carbon (C). Figures 6.5(b-d) portray a typical narrow-scan spectrum with its respective deconvoluted elements. The C 1s element was deconvoluted into four components found at 284.3 *eV* and 285.6 *eV*, and two small peaks at 286.2 e*V* and 288.3 *eV*. The highest intensity of C 1s at 284.3 *eV* denotes the 24-ring C sites (C_1, C_2, and C_3), while the peak at 285.6 *eV* signifies eight pyrrole C sites (C_4). The two low binding energy peaks noted at 286.2 *eV* and 288.3 *eV* reflect the $\pi - \pi^*$ shake-up satellite peaks, as reported for other Pc molecules (Park et al., 2003; Zhang et al., 2007).

Figure 6.5(c) showcases the electronic structure of vanadyl species in VTP, as well as the core-level spectra for O 1s and V 2p states that contain V $2p_{3/2}$ core level, V $2p_{1/2}$, and O 1s at 513.8 *eV*, 521.2 *eV*, and 528.9 *eV*, respectively. The main feature observed at 399 *eV* is attributable to N 1s state, which is present in the VTP molecular structure.

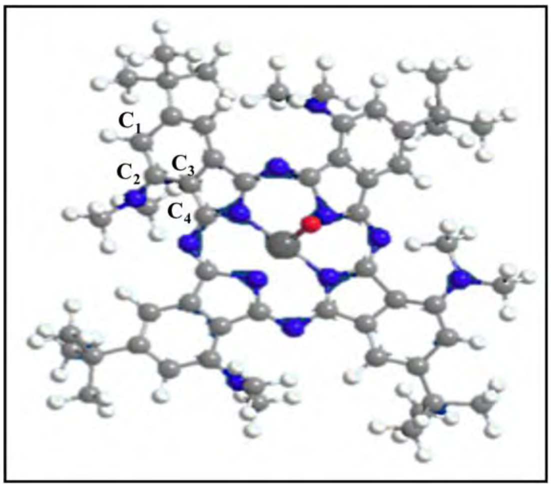

Figure 6.4: Schematic drawing of a VTP molecule with carbon sites labelled as C_1, C_2, C_3, and C_4

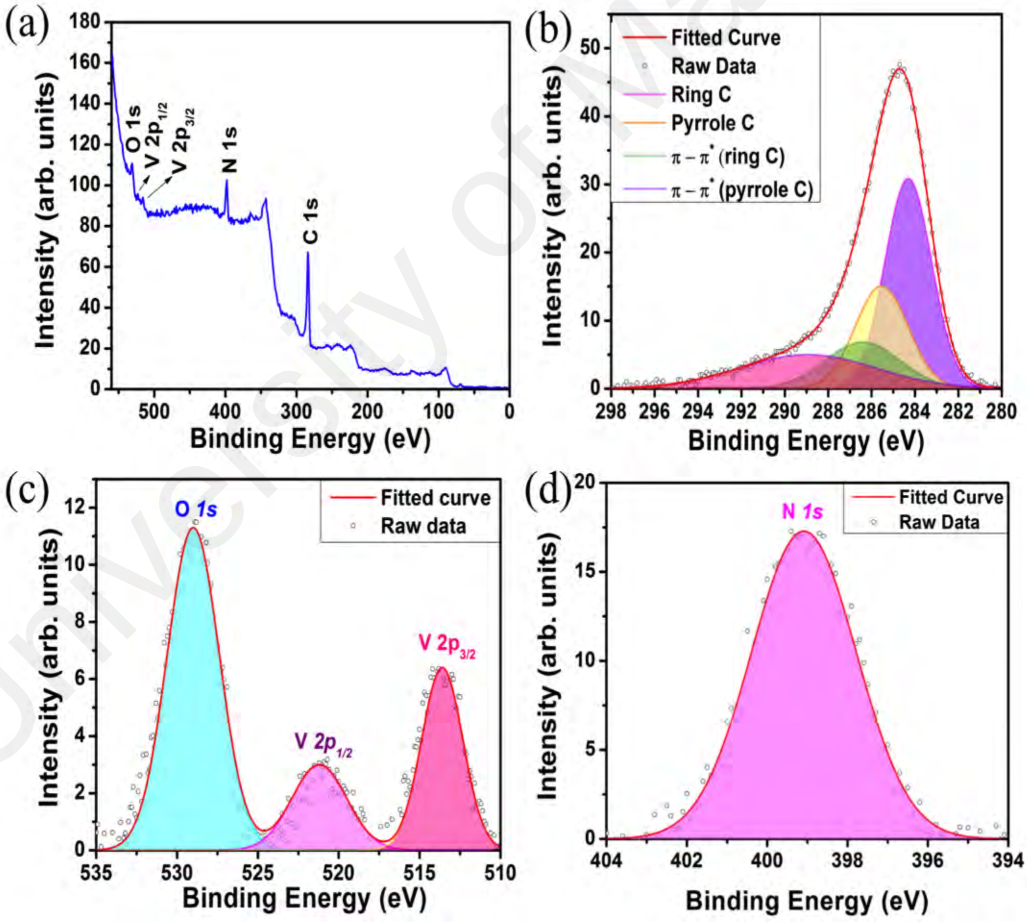

Figure 6.5: (a) Wide-scan XPS spectra of VTP structure. High-resolution XPS spectra of (b) C 1s (c) O 1s, V 2p, and (d) N 1s spectra of VTP thin film

6.4.2 Structural properties of VTP varied in spin speed

The structure of VTP thin films at three spin speed (500, 1000 and 2000 rpm) was assessed using micro-Raman spectroscopy. Figure 6.6 illustrates the Raman spectra of VTP thin films. The spectra signified that the VTP thin films did not experience any significant Raman shift, but exhibited varying intensities. The band observed at 1608 cm^{-1} is linked with carbon-carbon stretching in benzene ring, while the absorption peaks attributed to ring stretching were located at 1398 and 1516 cm^{-1}. Peaks noted at 550, 760, and 1137, along with 1181 and 1339 cm^{-1}, are attributable to ring deformation, ring vibration, C-H bending, and pyrrole stretching, respectively (Ahmad Makinudin & Supangat, 2016). The VTP thin films that displayed intense peaks revealed efficient moisture adsorption at spin speed below 2000 rpm, which seems to be in line with other findings (Abdullah et al., 2012). Table 6.1 tabulates the Raman shift and the respective assignments as the spin coating rotations speed had been varied.

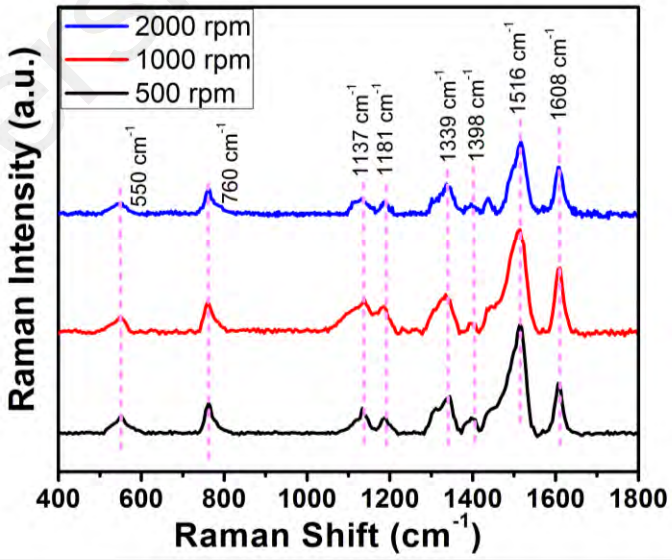

Figure 6.6: Raman spectra of VTP thin film

1x

Table 6.1: Raman shift and assignments of VTP thin film

Raman shift (cm^{-1})			
500 rpm	**1000 rpm**	**2000 rpm**	**Assignments**
551	548	545	Ring deformation
761	763	760	Ring vibration
1138	1138	1137	CH bending
1186	1188	1186	
1340	1337	1337	CH deformation
1399	1398	1403	Ring stretching
1516	1514	1516	
1608	1608	1608	C=C stretching

6.4.3 Wettability test of VTP thin films

In order to determine the behavior of VTP thin films based on the presence of hydrophilic or hydrophobic surfaces, a wettability test via contact-angle measurement was conducted. Hydrophilic surface generated an angle of $\theta_w < 90°$, while the hydrophobic surface resulted in an angle of $\theta_w > 90°$ (Ahmad Kamal et al., 2015). Figure 6.7 displays the water contact angle (C_A) with a static water droplet image. No huge impact was noted on the surface behavior of VTP thin films, even with increased rate of spin coating, thus verifying that the VTP thin films exerted hydrophilic surface behavior with $C_A \sim 82.5°$. With increment in the spin coating rate, the water C_A slightly decreased to ~ 80° and 77° for 1000 rpm and 2000 rpm, respectively. The wetting behavior of VTP thin films remained unchanged, and the hydrophilic surfaces were maintained. The wettability test is correlated with the sensitivity of Al/VTP/Al-based capacitive sensor device. Despite the slight variance noted in C_A, an impact was observed on the performance of the sensor device.

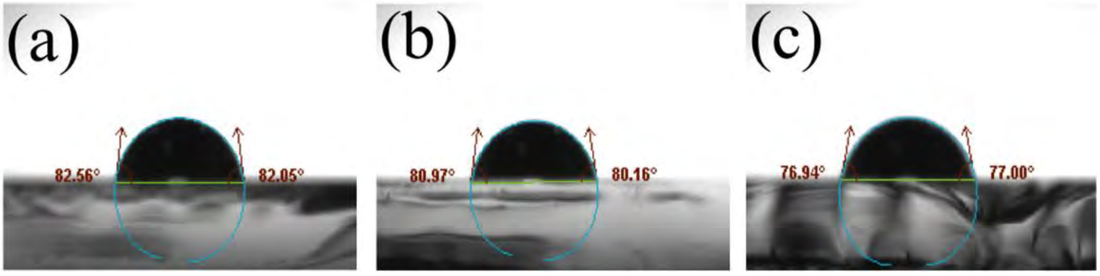

Figure 6.7: Water contact angle of the VTP thin film with a different spin coating rates of (a) 500 rpm, (b) 1000 rpm, and (c) 2000 rpm

6.4.4 Characterization of VTP-based humidity sensor devices

Figure 6.8(a) illustrates the normalized capacitance measurement outcomes of the Al/VTP/Al-based capacitive humidity sensors as a reference to delineate the correlation between the capacitance as a function of %RH at varying operating frequencies. The capacitance response of the sensor was normalized by the reference when the %RH was at its minimum as a function of %RH to uniform offset vertically for clarity (Islam et al., 2014). At lower operating frequency (500 Hz), the capacitance output increased significantly with increment in relative humidity; while at higher operating frequencies (1 kHz and 10 kHz), a small change was noted in the capacitance range and it is almost flat with the increasing relative humidity. As for the electrical characterization of the humidity sensors, it has been suggested to avoid using a frequency of <100 Hz, as this is bound to introduce the interface-trapped charge carrier that generates excess capacitance due to the polarization phenomenon. This greatly affects the stability and repeatability performance, despite being exceptionally sensitive (Al-Sehemi et al., 2016; Azmer et al., 2017). Zhang et al., (2014) applied an AC operational bias frequency at 40 Hz and discovered an unsteady humidity response. Therefore, this study employed an operational frequency of 500 Hz to determine the sensing parameters of the humidity sensors.

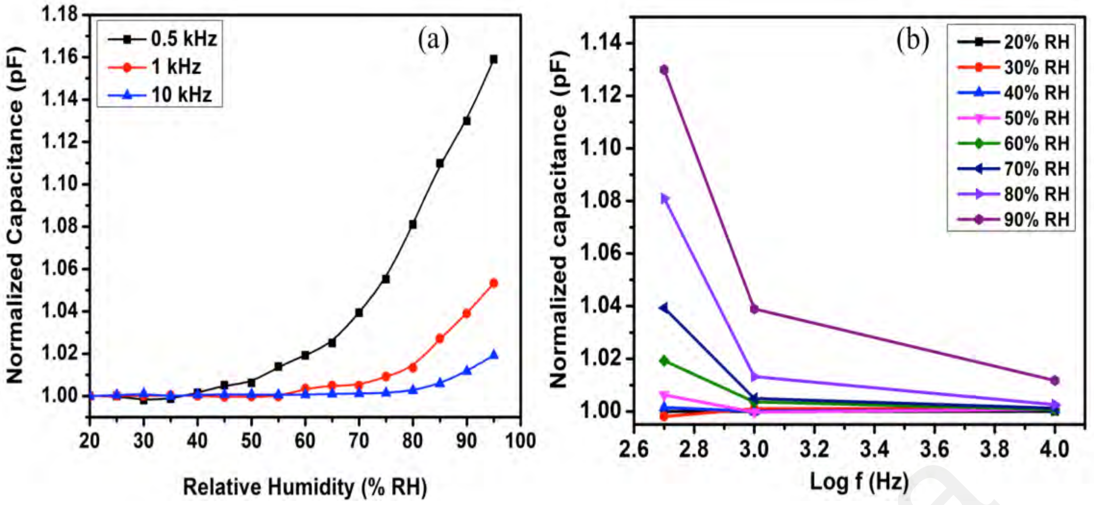

Figure 6.8: (a) Capacitance-relative humidity correlation of the Al/VTP/Al humidity sensor at 0.5 kHz, 1 kHz, and 10 kHz operational frequencies, (b) capacitance-frequency correlation at different values of relative humidity

Based on Figure 6.8(b), frequency clearly has a significant function in light of capacitive response, whereby the capacitance changed with logarithmic change for frequencies ranging between 0.5 kHz and 10 kHz. Figure 6.8 (b) illustrates the sharp decrease in capacitance with increment in frequency, although the decrease in capacitance is smaller at lower humidity, when compared to that of higher humidity. Increment of capacitance response at higher humidity is attributed to the adsorption of water molecules on the film surface, which promotes capillary condensation inside the pores of the film (Islam & Rahman., 2016).

The expression for capacitance of the device sensor (see Equation 6.1) reflects the relative dielectric permeability of the sensing film, the area of parallel electrodes (*A*), and the distance between the electrodes (*d*).

$$C = \frac{\varepsilon_o \varepsilon_d A}{d}, \tag{6.1}$$

Figure 6.8 (a) shows that the capacitive sensor is highly sensitive to RH variations. The presence of water uptake is highly sought to increase the net dielectric permeability of the sensing film due to the huge variance of dielectric permittivity between water and organic semiconductors. Increment of RH levels enhanced the permeability of sensing film, which further improved the electrical capacitance of the device. The expression between dielectric constant and capacitance is given as follows:

$$\frac{C_S}{C_O} = (\frac{\varepsilon_w}{\varepsilon_d})^n, \tag{6.2}$$

where, ε_w and ε_d refer to dielectric permittivity constant of the sensing film at wet and dry states, respectively, while n denotes the factor linked to the morphology of dielectric. The %RH was measured in the range of 20–95%, which was gradually increased by 5%. The capacitive humidity sensors exhibited non-linear response as a function of %RH. At lower %RH, the curves were almost flat; signifying that the capacitance is independent of humidity at low %RH (see Figure 6.10(a-c)). The coverage of the absorbed humidity on the sensing layer was discontinuous and constricted the immobile monolayer at %RH <20%. At this phase, water adhesion on the sensing film is characterized by weak Van Der Waals forces between water vapor and sensing film molecules (Matsuguchi et al., 1998).

Based on Equation 6.2, water displays high relative permittivity at ~ 80, and organic material exerts low dielectric at ~ 5. The capacitance is enhanced when more water molecules are absorbed by the active layer with increasing %RH. Therefore, the VTP-based capacitive sensor has the ability to detect the variations in humidity due to the enormous difference between relative permittivity and VTP layer (Karimov et al., 2011).

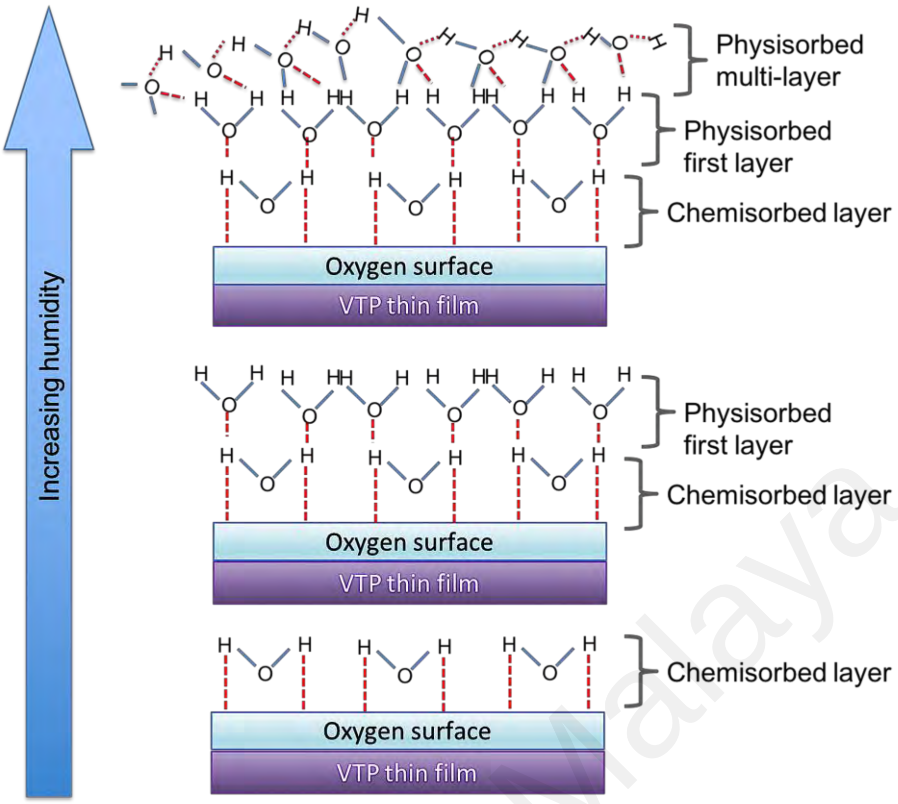

Figure 6.9: Schematic diagram of the humidity sensing mechanism of VTP thin film at varied humidity levels

Adsorption of water molecules onto a solid surface is attributable to chemisorption and physisorption, as shown in Figure 6.9. At low %RH, a molecule layer is generated due to chemisorption. Upon increment in adsorption, the first physisorption immobile layer transforms the mobile multilayers. The first two layers of water molecules are immobile due to the presence of double bonds. The other physisorption layers have single bonds, hence the ability to easily move and polarize. At this stage, the monotonically increasing capacitance reflects the changes in capacitance, which correlate with the amount of adsorbed water molecules (Aziz et al., 2010).

The sensitivity of humidity sensor can be calculated using the following equation:

$$Sensitivity, S = \frac{(C_{max} - C_{min})}{(RH_{max} - RH_{min})} \times 100\% \qquad (6.3)$$

C_{max} & C_{min} and RH_{max} & RH_{min} represent maximum & minimum capacitance and relative humidity values, respectively. The sensitivities were estimated within 20% and 95% bandwidths at 500 Hz operational frequency.

Figures 6.10 (a–c) display the capacitance-relative humidity correlation of Al/VTP/Al humidity sensor in three spin speeds; 500, 1000, and 2000 rpm, respectively. The thinnest VTP film sensor, which was deposited by 2000 rpm. had a capacitance of 17.5 pF and a sensitivity of ~ 9.2 pF/%RH. In comparison, the thickest VTP film sensor, which was produced at 500 rpm, exerted a capacitance of 9.39 pF and a sensitivity of 2.55 pF/%RH. This is attributable to the effect of the spin coating rates that can influence both the thickness and the contact-angle properties. Upon applying a higher spin coating rate, the centrifugal force generated by the spin coater spins off more particles from the substrate, hence the formation of a thinner film (Jayamurugan et al., 2015). Reducing the thickness and contact angle enables more chemisorption of the water molecules. Reduction in sensitivity due to increasing sensing film thickness in the range studied seems to be in line with past reported results (Aziz et al., 2010; Harrey et al., 2002).

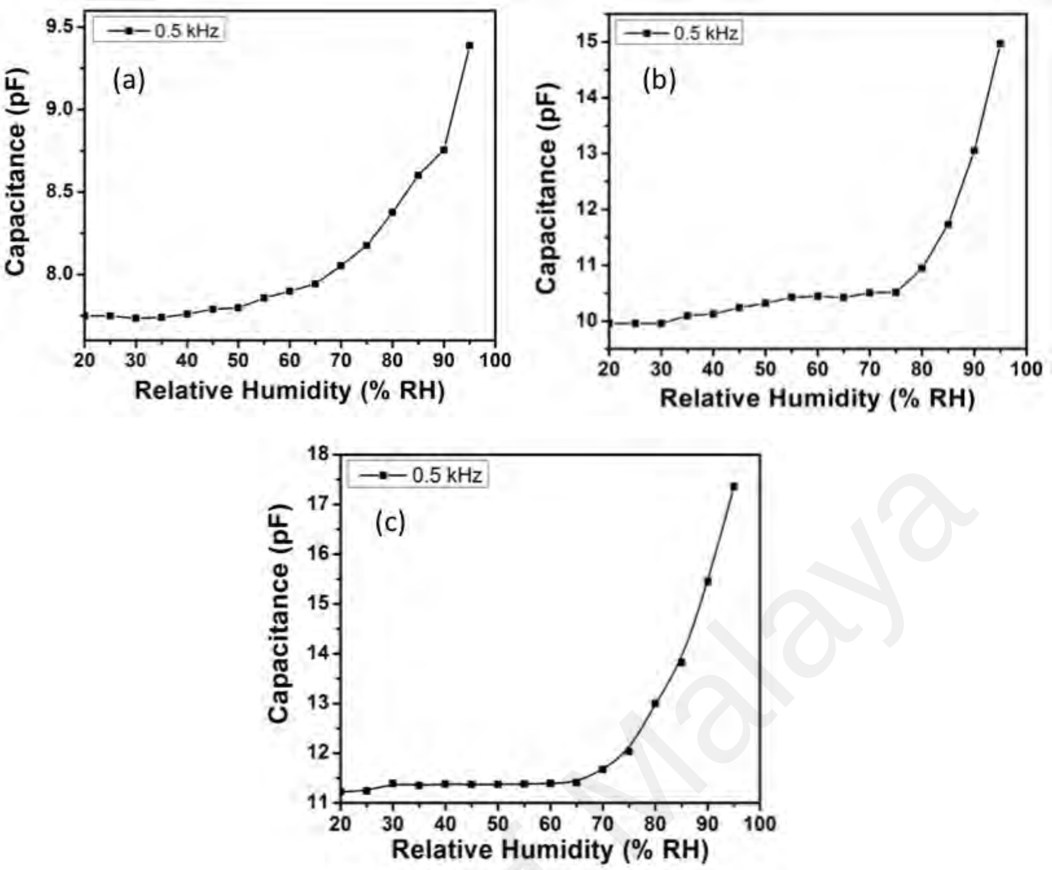

Figure 6.10: Capacitive-relative humidity correlation of device at a) 500 rpm, b) 1000 rpm, and c) 2000 rpm at 500 Hz operational frequency

Hysteresis is a common issue that occurs in humidity sensors due to pore size, pores geometry, and dielectric sensing layer thickness (Islam et al., 2014). A good sensor should possess exceptional reversibility or hysteresis with small deviation error. The hysteresis effect refers to the percentage of deviation in the measured capacitance during the absorption cycle from that during the desorption cycle. Hysteresis can be determined by observing the capacitive response of the sensor at a fixed frequency for full scale in increasing and decreasing of RH values. Hysteresis can be calculated by using the following equation:

$$Hysteresis, H = average\left[\frac{C_{desorption} - C_{adsorption}}{C_{adsorption}}\right] \times 100\% \qquad (6.4)$$

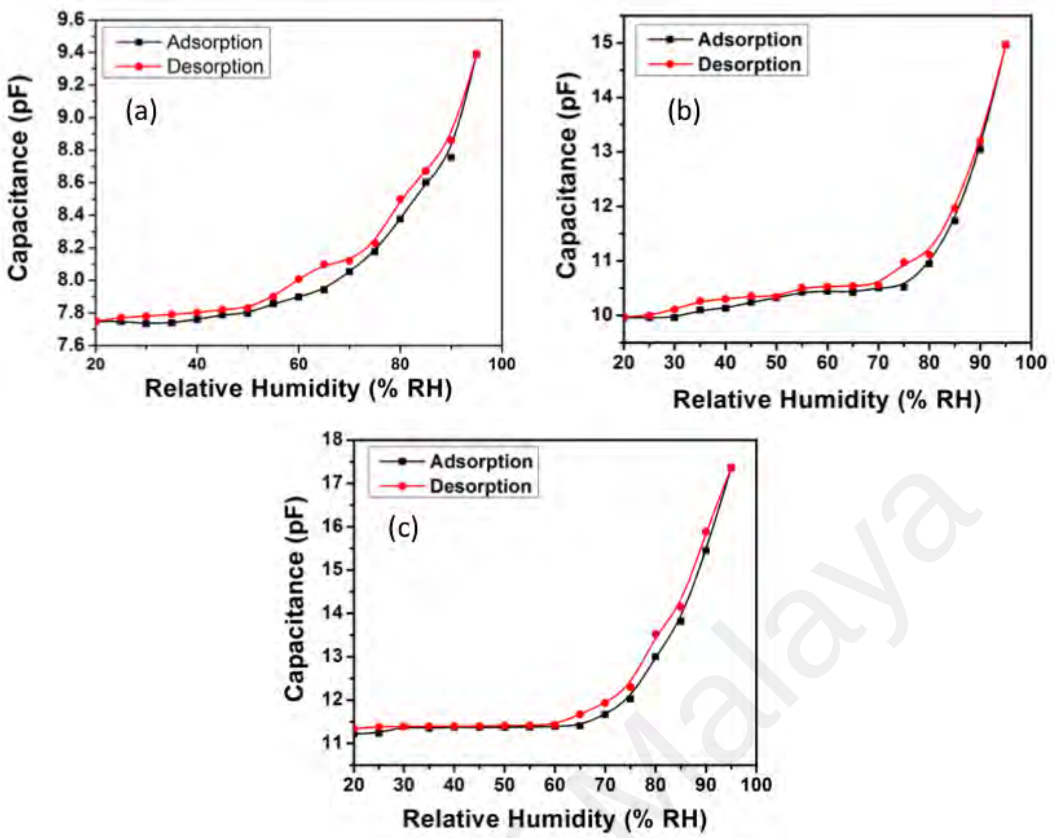

Figure 6.11: Hysteresis curve of device at a) 500 rpm, b) 1000 rpm, and c) 2000 rpm

The graphs displayed in Figures 6.11 (a–c) reveal the minor occurrence of hysteresis in response to the increasing and decreasing of RH steps analyzed at 0.5 kHz under 1 V. The smallest hysteresis signifies the efficient adsorption and desorption processes. Meanwhile, Figure 6.11 (a–c) exhibits that hysteresis is bound to grow bigger with increasing spin speed. The device with 2000 rpm spin speed recorded a recovery time of 15 s with slightly higher hysteresis (1.26%), when compared to the devices exposed to 500 rpm (0.70%) and 1000 rpm (1.16%). Perhaps, this is due to the presence of a thinner film that has less pores than those in thicker film. Figure 6.14 portrays the presence of pores in the VTP thin film. A small hysteresis gap determines the presence of abundant nanopores in the active layer (Qi et al., 2009).

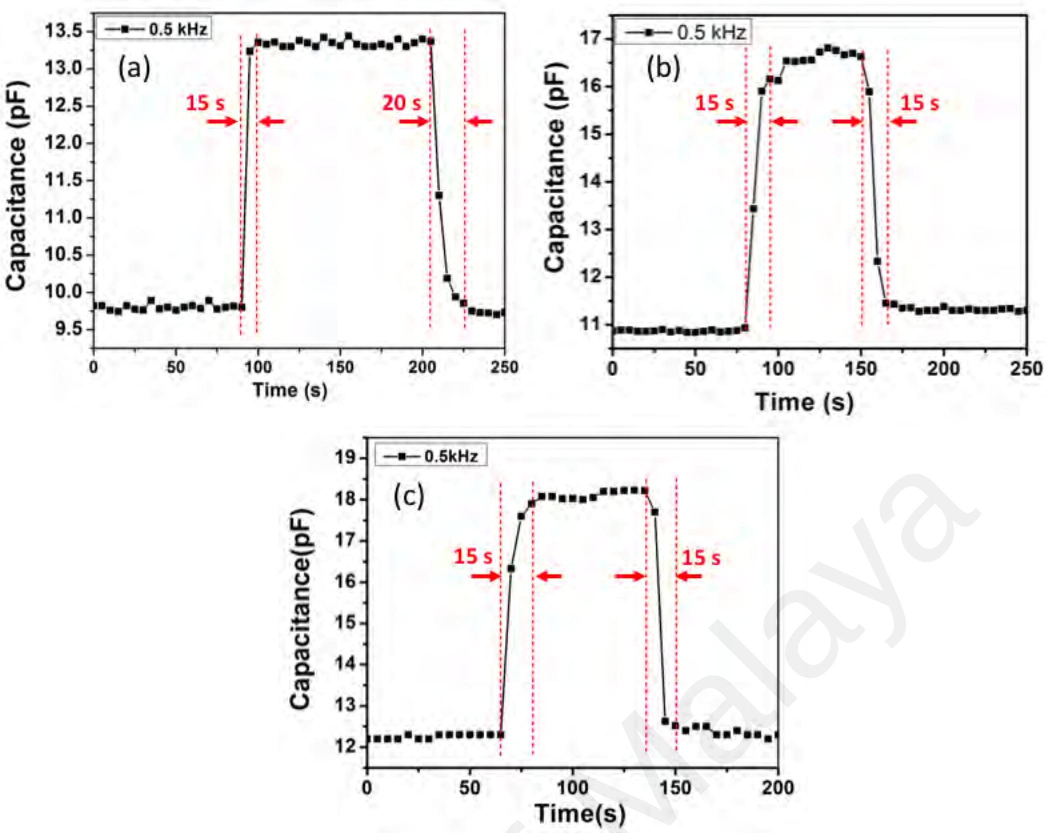

Figure 6.12: Capacitive response-recovery curves of device at a) 500 rpm, b) 1000 rpm, and c) 2000 rpm

While assessing the performance of humidity sensors, the response and recovery time have an imminent function. Both these values can be measured by changing the alternate humidity between 60 and 95%RH. The response or recovery time refers to the time taken by a sensor to achieve 90% of the total change in capacitance (Tripathy et al., 2014). Response time can be determined during the increasing adsorption from 60 to 95%RH, while recovery time is determined during desorption when relative humidity quickly drops from 95 to 60%RH. Figures 6.12 (a-c) illustrate the response and recovery graphs of varied spin speeds of VTP thin film. The thinnest device sensor with 2000 rpm (66 ± 5 nm) exhibited 15-s response and recovery time, which seemed similar to that for 1000 rpm, when compared to 500 rpm device sensor. This signifies the effect of spin coating rate that eases desorption, mainly because the contact between water molecules and sensing film becomes less than that observed in the other two device sensors. Table 6.2 tabulates the sensing parameters of the three sensors at varied spin speeds for the similar 20–95% RH range.

Table 6.2: Sensing parameters of VTP-based capacitive sensors

Humidity sensor	**Thickness (nm) ± 5 nm**	**Sensitivity, S (pF/%RH)**	**Hysteresis, H (%)**	**Response Time (s)**	**Recovery Time (s)**
500 rpm	90	2.55	0.70	15	20
1000 rpm	80	7.70	1.16	15	15
2000 rpm	66	9.20	1.26	15	15

It is vital to study the drift for the sensor output due to temperature and aging (Islam et al., 2015). Figure 6.13(a) portrays the impact of temperature on output characteristics of the humidity sensor. The capacitance value of the device was recorded at 500 Hz frequency with increment of temperature from 27 ℃ to 100 ℃. Figure 6.13(a) illustrates that the output capacitance displayed exceptional stability as the temperature rose until ~60 ℃. Further increment of temperature (60 ℃ − 100 ℃) showed that the output sensor displayed increased value on the capacitance response. The capacitance response increased by ~1.2-fold from the initial value when temperature was elevated from 60 ℃ − 100 ℃. The increased capacitance response with temperature is attributable to the polarization mechanism. It is common to have trap states at the interface of metal semiconductor (Chiu, 2014). With increased temperature, sufficient energy is provided to the trapped charge carriers to overcome the energy barriers of the trap states, thus increasing the space charge polarization. This phenomenon escalates the dielectric constant of the semiconductor film, which consequently enhances the capacitance of the device at elevated temperature (Al-Sehemi et al., 2016; Dokme et al., 2010; Islam et al., 2012). In fact, these reported outcomes correlate well with other studies, in which the device sensors exhibited significant thermal drift at elevated temperature. It is noteworthy to highlight that thermal drift is negligible with operating temperature below 60 °C (Azmer et al., 2016; Raza et al., 2016). Figure 6.13(b) displays the stability over time at varying humidity levels. The same device was tested over five-day interval, whereby the capacitance response was nearly constant even at the highest humidity. This finding signified no significant drift on the aging effect.

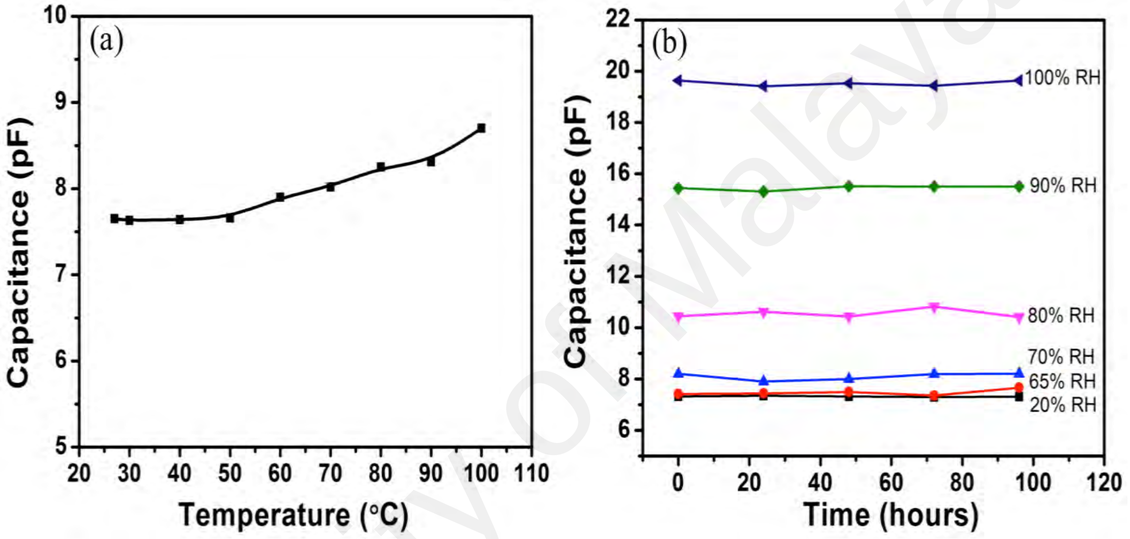

Figure 6.13: Drift in sensor output with (a) variation of working temperature at 60% RH, (b) variation of relative humidity at different working time (hours)

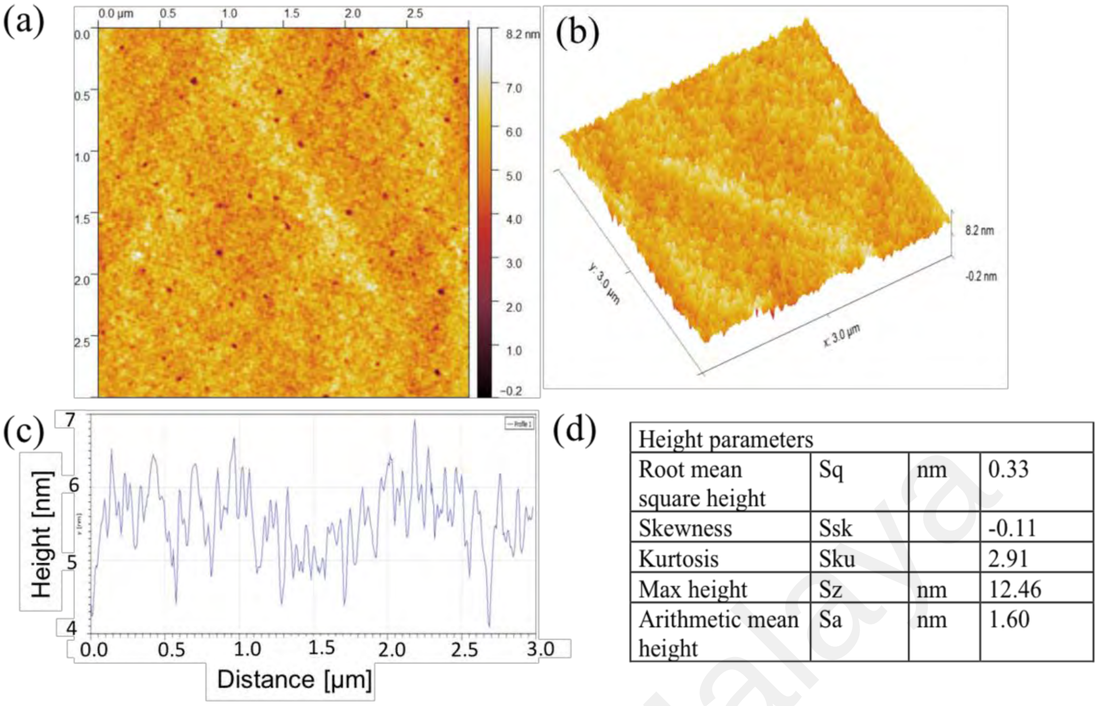

Height parameters			
Root mean square height	Sq	nm	0.33
Skewness	Ssk		-0.11
Kurtosis	Sku		2.91
Max height	Sz	nm	12.46
Arithmetic mean height	Sa	nm	1.60

Figure 6.14: (a) 2D AFM micrograph (b) 3D AFM micrograph (c) cross-section analysis and (d) surface morphology data of VTP thin film with a spin speed of 2000 rpm

The VTP thin film on glass substrate with 2000 rpm spin coating rate was further characterized via AFM (3×3 µm scan rate) to assess its surface morphology and roughness. The AFM images, which were acquired from tapping mode, had been analyzed using the Gwyddion 2.48 data visualization and analysis tool software. Figures 6.14(a) and (b) display the 2D and 3D AFM micrographs of VTP thin film with 2000 rpm spin coating rate. The diameter and the depth of the pores were approximately estimated from the cross-sectional analysis of the thin film (see Figure 6.14(c)). Figure 6.14(d) shows the tabulated key data in relation to their morphological surfaces, as processed using the Gwyddion software package. The AFM images reveal the presence of non-uniform and rough surfaces with peaks. The RMS roughness value was ~ 0.33 nm. The film topography hinted the formation of interpenetrating networks, which suggests that the VTP thin film is indeed a potential material for humidity sensing (Aziz et al., 2010).

Table 6.3 presents the comparison of key sensing parameters of the proposed VTP-based humidity sensor with humidity sensors reported in the literature. The sensing performance of the VTP-based humidity sensor seems to outperform the rest with higher frequency and better stability. It obviously shown that the sensing performance of the VTP based humidity sensor is much higher with higher in frequency and better stability.

Table 6.3: Comparison table of performances of humidity sensors reported in the literature

Type of organic humidity sensor	Sensitivity at 100 Hz	Hysteresis	Response and recovery	Reference
MEH-PPV:PVP	114 fF/ %RH	~ 2%	18 s and 8 s	(Azmer et al., 2016)
$PBObzT_2$	5 pF/ %RH	2.76%	10 s and 4 s	(Raza et al., 2016)
$VoPcPhO:AlQ_3$	0.325 pF/ %RH	-	4 s and 3 s	(Fatima et al., 2017)
Al_2O_3	2.24 pF/ppm	0.33%	47 s and 118 s	(Tarikul Islam et al., 2012)
VTP	~9.2 pH/%RH (500 Hz)	1.26%	15 s and 15 s	Current work

6.5 Summary

This study determined the thickness of VTP-based capacitive sensors by employing a simple and cost-efficient method. The optimization of capacitive humidity sensor design relied heavily on the fabrication method applied and on accurate characterization of the sensitivity of VTP active layer film thicknesses. The sensor performance has been proven to depend on the sensing film thickness. The thinnest film (66 ± 5 nm) device sensor exhibited greater sensitivity than that of thicker (80 ± 5 nm and 90 ± 5 nm) film devices. This is attributed to the enhanced chemisorption of water in light of thickness and contact angle. The AFM images portrayed that the VTP thin film had rough surface, which indicated the existence of an inter-penetrating VTP molecular network. These results enhance one's understanding regarding the influence of the thickness variation on VTP-based sensor, as well as the crucial parameters that control the device performance of the media under investigation in meeting the potentiality to function as viable humidity sensors.

CHAPTER 7: CONCLUSIONS AND FUTURE WORKS

7.1 Conclusions

Organic electronic devices place an escalating demand in the current market. That being mentioned, the urge to seek a new organic material that ascertains the progression of organic electronic applications and improvement of the device performance is one that is undeniable. In pursuing such an aim, this present study is geared towards this objective. In this final chapter, summary of the study findings can be categorized into three major sections. A number of experimental shortcomings that were encountered are also discussed, and finally, suggestions for future work are outlined.

Initially, investigations pertaining to the VTP as the active layer for fabrication of electrical devices are discussed. Prior to the fabrication process, the VTP thin film was characterized to determine the values of HOMO/LUMO and energy band gap. The HOMO and LUMO energy levels of VTP were determined from CV, which resulted in -5.10 *eV* and -3.90 *eV*, respectively. The energy band gap, which was evaluated by using absorption spectra and Tauc plot methods, resulted in 1.39 *eV* and 1.42 *eV*, respectively. Two types of OFET arrangements, lateral and vertical, were fabricated and their performances were assessed. As a result, the VOFET displayed better performance in terms of output current, threshold voltage, and turn on/off ratio with values of 37 mA/cm^2, 7 *V*, and 10^5, in comparison to LOFET that recorded 2.5 x 10^{-4} mA/cm^2, 10 *V*, and 10^2, respectively. The primary reason for this scenario is attributed to the reduction in the channel length between S-D electrodes, which has improved the transport of the current drift between the electrodes. The optimization of the active layer thickness was performed, in which 2000 rpm had successfully displayed an optimized performance, in comparison to other spinning speeds. The main shortcoming in this section was confronted during the characterization of LOFET, whereby the saturation region could not be achieved due to the limitation in SMU power supply that occurred at the laboratory. This study investigated the performance of VTP in lateral and vertical OFET, apart from optimizing the active layer thickness in VOFET devices.

In the second section of the experimental work, the performance of VTP was further studied by fabricating organic optical devices. Initially, both VTP and VTP:$PC_{71}BM$ blended thin films were optimized for the best photovoltaic effect performance. Next, the VTP was utilized as a single component in the fabrication of semiconductor diode to determine several electrical parameters. This investigation looked into the nature of charge transport in VTP applied in real device. It is evident from the outcomes that the diode parameters, such as barrier height, ideality height, series and shunt resistance, as well as mobility, are indeed comparable with other reckoned organic materials. This makes the VTP a promising candidate to be used in optoelectronic applications. Next, the best ratio concentration was selected and applied as the active layer to assess the photovoltaic effect of the blended film. As a result, the device failed to satisfy sufficient power conversion for the conventional energy harvest. The photovoltaic response of the VTP:$PC_{71}BM$ only yielded efficiency up to 0.06%, which could be due to low absorption intensity in the visible range, as well as relatively low effective mobility at 7.63 x 10^{-5} $cm^2/V.s$. The outcomes were inadequate to increase the charge separation, which resulted in extremely low energy conversion from light energy to electrical energy. The VTP:$PC_{71}BM$ was employed in OPD and surprisingly, the device displayed exceptional photoresponsivity towards variations in light intensity; 2.30×10^{-1}A/W. This is attributed to the extended ligands that belong to the VTP, which are responsible for enhancing the sensing layer of the OPD device. Overall, in this particular work, the

VTP was integrated with $PC_{71}BM$ to form a BHJ system in order to study photovoltaic response and OPD performance. Nevertheless, the VTP:$PC_{71}BM$ blend gave low photovoltaic response, despite acquiring good photoresponsivity in OPD.

In the final section, the VTP was employed as the active layer for the fabrication of organic humidity sensor. Prior to that, the physical properties of VTP thin films were studied and characterized to ensure that the correlation between film thickness and device performance is well understood. As a result, the VTP seemed suitable for application in humidity sensor due to its porous surface and its hydrophilic feature. The device with the thinnest film displayed better performance in capacitance response at 9.2 pF/%RH, when compared to thicker films in 1000 rpm and 500 rpm with 7.7 and 2.2 pF/%RH, respectively. This refers to an optimized thickness, as it is unfeasible to further increase the spin speed. Otherwise, all the solutions would splash off and no solution would remain on the gap of the electrode.

Overall, this study focused into VTP-based organic semiconductor devices, which covered OFET, OPV, OPD, and organic humidity sensor. The first mentioned refers to VTP-based OFET that displayed a noticeable upsurge in its current output, threshold voltage, and turn on/off ratio when the VOFET arrangement was applied instead of the LOFET arrangement. Next, the VTP was applied in the photovoltaic device and OPD by mixing with $PC_{71}BM$ to form the BHJ system. As a result, the VTP:$PC_{71}BM$ exhibited low photovoltaic response, but very high photoresponsivity in OPD. The last mentioned is the study of VTP-based organic humidity sensor by varying the thicknesses for the active layer. The results revealed significant improvement in device performance, especially when thinner active layer VTP is applied, instead of thicker ones.

7.2 Future works

The VTP seems to display promising properties as a small molecule material and suitable to be employed as an active layer in the fabrication of organic devices. Nevertheless, a number of challenges need to be addressed to accomplish this present work, wherein the following endeavors were not possible within the stipulated time frame of this study.

1. The characterization and optimization of the dielectric and source electrode layers should be further assessed in-depth, especially the fabrication of VOFET. Several essential points that should be addressed pertaining to device stability and current leakage.

2. The use of transition metal oxides (TMOs), such as vanadium pentaoxide (V_2O_5), as HTL in the fabrication of OPD may be investigated. This will probably enhance the photoresponse of the present performance and contribute to a device with better stability.

3. The utilization of metal oxide nanoparticles, such as TiO_2, in the fabrication of Al/VTP:TiO_2/Al organic-inorganic hybrid humidity sensor may be assessed. This will, in turn, enhance the humidity sensing film, particularly towards enhancing the film morphology by devising a highly desirable nano-porous structure.

REFERENCES

Abdullah, S. M., Ahmad, Z., Aziz, F., & Sulaiman, K. (2012). Investigation of VOPcPhO as an acceptor material for bulk heterojunction solar cells. *Organic Electronics, 13*(11), 2532-2537.

Abdullah, S. M., Ahmad, Z., & Sulaiman, K. (2015). The impact of thermal annealing to the efficiency and stability of organic solar cells based on PCDTBT: $PC_{71}BM$. *Procedia - Social and Behavioral Sciences, 195*, 2135-2142.

Aernouts, T., Aleksandrov, T., Girotto, C., Genoe, J., & Poortmans, J. (2008). Polymer based organic solar cells using ink-jet printed active layers. *Applied Physics Letters, 92*(3), 22-24.

Agmon, N. (1995). The grotthuss mechanism. *Chemical Physics Letters, 244*(5-6), 456-462.

Ahmad Kamal, S. A., Ritikos, R., & Abdul Rahman, S. (2015). Wetting behaviour of carbon nitride nanostructures grown by plasma enhanced chemical vapour deposition technique. *Applied Surface Science, 328*, 146-153.

Ahmad Makinudin, A. H., & Supangat, A. (2016). Improving the properties of VTP by incorporating fullerene. *RSC Advances, 6*(37), 30963-30971.

Ahmad, Z., Abdullah, S. M., & Sulaiman, K. (2013). Bulk heterojunction photodiode: To detect the whole visible spectrum. *Measurement, 46*(7), 2073-2076.

Ahmad, Z., Sayyad, M. H., Saleem, M., Karimov, K. S., & Shah, M. (2008). Humidity-dependent characteristics of methyl-red thin film-based Ag/methyl-red/Ag surface-type cell. *Physica E: Low-dimensional Systems and Nanostructures, 41*(1), 18-22.

Ahmad, Z., Sayyad, M. H., Wahab, F., Sulaiman, K., Shahid, M., Chaudry, J. A., . . . Aziz, F. (2013). Enhancement of electronic and charge transport properties of NiPc by potassium-tetrasulpho group. *Physica B: Condensed Matter, 413*, 21-23.

Ahmad, Z., Sayyad, M. H., Yaseen, M., Aw, K. C., M-Tahir, M., & Ali, M. (2011). Potential of 5,10,15,20- Tetrakis (3′ ,5′ -di-tertbutylphenyl) porphyrinatocopper(II) for a multifunctional sensor. *Sensors and Actuators B: Chemical, 155*(1), 81-85.

Ahmad, Z., Suhail, M. H., Muhammad, I. I., Al-Rawi, W. K., Sulaiman, K., Zafar, Q., ... Shaameri, Z. (2013). MEH-PPV/Alq3-based bulk heterojunction photodetector. *Chinese Physics B, 22*(10), Article#100701.

Ahmad, Z., Touati, F., Shakoor, R., & Al-Thani, N. (2016). Study of a ternary blend system for bulk heterojunction thin film solar cells. *Chinese Physics B, 25*(8), Article#080701.

Al-Sehemi, A. G., Al-Assiri, M. S., Kalam, A., Zafar, Q., Azmer, M. I., Sulaiman, K., & Ahmad, Z. (2016). Sensing performance optimization by tuning surface morphology of organic (D-π-A) dye based humidity sensor. *Sensors and Actuators B: Chemical, 231*, 30-37.

Al-Ta'ii, H. M. J., Amin, Y. M., & Periasamy, V. (2016). Humidity influenced capacitance and resistance of an Al/DNA/Al Schottky diode irradiated by alpha particles. *Scientific Reports, 6*, Article#25519.

An, K. H., O'Connor, B., Pipe, K. P., & Shtein, M. (2009). Organic photodetector with spectral response tunable across the visible spectrum by means of internal optical microcavity. *Organic Electronics, 10*(6), 1152-1157.

Arbab, E. A., Taleatu, B. A., & Mola, G. T. (2015). Ternary molecules blend organic bulk heterojunction solar cell. *Materials Science in Semiconductor Processing, 40*, 158-161.

Aziz, F., Ahmad, Z., Abdullah, S., Sulaiman, K., & Sayyad, M. (2015). Photovoltaic effect in single-junction organic solar cell fabricated using vanadyl phthalocyanine soluble derivative. *Pigment & Resin Technology, 44*(1), 26-32.

Aziz, F., Sayyad, M. H., Karimov, K. S., Saleem, M., Ahmad, Z., & Khan, S. M. (2010). Characterization of vanadyl phthalocyanine based surface-type capacitive humidity sensors. *Journal of Semiconductors, 31*(11), Article#114002.

Azmer, M. I., Ahmad, Z., Sulaiman, K., Touati, F., Bawazeer, T. M., & Alsoufi, M. S. (2017). VOPcPhO:P3HT composite micro-structures with nano-porous surface morphology. *Applied Surface Science, 399*, 426-431.

Azmer, M. I., Aziz, F., Ahmad, Z., Raza, E., Najeeb, M. A., Fatima, N., . . . Sulaiman, K. (2017). Compositional engineering of VOPcPhO-TiO_2 nano-composite to reduce the absolute threshold value of humidity sensors. *Talanta, 174*, 279-284.

Azmer, M. I., Zafar, Q., Ahmad, Z., & Sulaiman, K. (2016). Humidity sensor based on electrospun MEH-PPV:PVP microstructured composite. *RSC Advances, 6*(42), 35387-35393.

Bagher, A. M. (2014). Comparison of organic solar cells and inorganic solar cells. *International Journal of Renewable and Sustainable Energy, 3*(3), 53-58.

Bakar, N. A., Supangat, A., & Sulaiman, K. (2015). Formation of PCDTBT:$PC_{71}BM$ p–n junction composite nanotubes via a templating method. *RSC Advances, 5*(124), 102689-102699.

Banerjee, G., & Sengupta, K. (2002). Pore size optimisation of humidity sensor—a probabilistic approach. *Sensors and Actuators B: Chemical, 86*(1), 34-41.

Ben-Sasson, A. J., Azulai, D., Gilon, H., Facchetti, A., Markovich, G., & Tessler, N. (2015). Self-assembled metallic nanowire-based vertical organic field-effect transistor. *ACS Applied Material Interfaces, 7*(4), 2149-2152.

Benhaliliba, M., Ocak, Y., & Benouis, C. (2014). Effect of metal on characteristics of MPc organic diodes. *Journal of Nano and Electronic Physics, 6(4)*, Article#04009-1.

Brabec, C. J., Cravino, A., Meissner, D., Sariciftci, N. S., Fromherz, T., Rispens, M. T., . . . Hummelen, J. C. (2001). Origin of the open circuit voltage of plastic solar cells. *Advanced Functional Materials, 11*(5), 374-380.

Braga, A., Moreira, S., Zampieri, P., Bacchin, J., & Mei, P. (2008). New processes for the production of solar-grade polycrystalline silicon: A review. *Solar Energy Materials and Solar Cells, 92*(4), 418-424.

Bredas, J., Marder, S., & Salaneck, W. R. (2002). Alan J. Heeger, Alan G. MacDiarmid, and Hideki Shirakawa-Tribute. *Macromolecules, 35*(4), 1137-1139.

Bredas, J.-L., Beljonne, D., Coropceanu, V., & Cornil, J. (2004). Charge-transfer and energy-transfer processes in π-conjugated oligomers and polymers: a molecular picture. *Chemical Reviews, 104*(11), 4971-5004.

Brus, V. V., Proctor, C. M., Ran, N. A., & Nguyen, T. Q. (2016). Capacitance spectroscopy for quantifying recombination losses in nonfullerene small‐molecule bulk heterojunction solar cells. *Advanced Energy Materials, 6*(11), Article#1502250.

Cai, W., Gong, X., & Cao, Y. (2010). Polymer solar cells: recent development and possible routes for improvement in the performance. *Solar Energy Materials and Solar Cells, 94*(2), 114-127.

Chen, Y., Fang, W., Wang, K., Liu, W., & Jiang, J. (2016). Nonperipheral tetrakis (dibutylamino) phthalocyanines. New types of 1, 8, 15, 22-Tetrakis (substituted) phthalocyanine isomers. *Inorganic Chemistry, 55*(18), 9289-9296.

Chiguvare, Z., Parisi, J., & Dyakonov, V. (2003). Current limiting mechanisms in indium-tin-oxide/poly3-hexylthiophene/aluminum thin film devices. *Journal of Applied Physics, 94*(4), 2440-2448.

Chiu, F.-C. (2014). A review on conduction mechanisms in dielectric films. *Advances in Materials Science and Engineering, 2014.* Article#578168.

Choy, W. C. H. (2012). *Organic solar cells: Materials and device physics*. New York: Springer Verlag London.

Claessens, C. G., Hahn, U., & Torres, T. (2008). Phthalocyanines: From outstanding electronic properties to emerging applications. *The Chemical Record, 8*(2), 75-97.

Collins, R., Krier, A., & Abass, A. (1993). Optical properties of lead phthalocyanine (PbPc) thin films. *Thin Solid Films, 229*(1), 113-118.

Cosseddu, P., & Bonfiglio, A. (2007). A comparison between bottom contact and top contact all organic field effect transistors assembled by soft lithography. *Thin Solid Films, 515*(19), 7551-7555.

Dahlen, M. A. (1939). The phthalocyanines a new class of synthetic pigments and dyes. *Industrial & Engineering Chemistry, 31*(7), 839-847.

De La Torre, G., Claessens, C. G., & Torres, T. (2007). Phthalocyanines: old dyes, new materials. Putting color in nanotechnology. *Chemical Communications (Camb) 38*(20), 2000-2015.

De La Torre, G., Vazquez, P., Agullo-Lopez, F., & Torres, T. (2004). Role of structural factors in the nonlinear optical properties of phthalocyanines and related compounds. *Chemical Reviews, 104*(9), 3723-3750.

Di Natale, C., Macagnano, A., Repole, G., Saggio, G., D'Amico, A., Paolesse, R., & Boschi, T. (1998). The exploitation of metalloporphyrins as chemically interactive material in chemical sensors. *Materials Science and Engineering: C, 5*(3), 209-215.

Dimitrov, A. S., Kralchevsky, P. A., Nikolov, A. D., Noshi, H., & Matsumoto, M. (1991). Contact angle measurements with sessile drops and bubbles. *Journal of Colloid and Interface Science, 145*(1), 279-282.

Dittmer, J. J., Lazzaroni, R., Leclère, P., Moretti, P., Granström, M., Petritsch, K., . . . Holmes, A. B. (2000). Crystal network formation in organic solar cells. *Solar Energy Materials and Solar Cells, 61*(1), 53-61.

Dokme, I., Altındal, Ş., Tunç, T., & Uslu, I. (2010). Temperature dependent electrical and dielectric properties of Au/polyvinyl alcohol (Ni, Zn-doped)/n-Si Schottky diodes. *Microelectronics Reliability, 50*(1), 39-44.

Ebenhoch, B., Thomson, S. A. J., Genevičius, K., Juška, G., & Samuel, I. D. W. (2015). Charge carrier mobility of the organic photovoltaic materials PTB7 and $PC_{71}BM$ and its influence on device performance. *Organic Electronics, 22*, 62-68.

El Nhass, M., Soliman, H., Metwally, H., Farid, A., Farag, A., & El Shazly, A. (2001). Optical properties of evaporated iron phthalocyanine (FePc) thin films. *Journal of Optics, 30*(3), 121-129.

Fakir, M. S., Ahmad, Z., & Sulaiman, K. (2012). Modification of optical band gap and surface morphology of NiTsPc thin films. *Chinese Physics Letters, 29*(12), Article#126802.

Farahani, H., Wagiran, R., & Hamidon, M. N. (2014). Humidity sensors principle, mechanism, and fabrication technologies: a comprehensive review. *Sensors (Basel), 14*(5), 7881-7939.

Farooq, A., Karimov, K. S., Ahmed, N., Ali, T., Khalid Alamgir, M., & Usman, M. (2015). Copper phthalocyanine and metal free phthalocyanine bulk heterojunction photodetector. *Physica B: Condensed Matter, 457*, 17-21.

Fatima, N., Aziz, F., Ahmad, Z., Najeeb, M., Azmeer, M., Karimov, K. S.,...Sulaiman, K. (2017). Compositional engineering of the pi-conjugated small molecular VOPcPhO: Alq3 complex to boost humidity sensing. *RSC Advances, 7*(32), 19780-19786.

Forrest, S. R. (1997). Ultrathin organic films grown by organic molecular beam deposition and related techniques. *Chemical Reviews, 97*(6), 1793-1896.

Frost, R. L. (2006). A Raman spectroscopic study of selected minerals of the rosasite group. *Journal of Raman Spectroscopy. 37*(9), 910-921.

Garnett, E., & Yang, P. (2010). Light trapping in silicon nanowire solar cells. *Nano Letters, 10*(3), 1082-1087.

Geng, S., Zhang, S., & Onishi, H. (2002). XPS applications in thin films research. *Materials Technology, 17*(4), 234-240.

Giovannetti, R. (2012). The use of spectrophotometry UV-Vis for the study of porphyrins. In *Macro to nano spectroscopy.* IntechOpen, Croatia.

Gouterman, M. (1959). Study of the effects of substitution on the absorption spectra of porphin. *The Journal of Chemical Physics, 30*(5), 1139-1161.

Gouterman, M. (1961). Spectra of porphyrins. *Journal of Molecular Spectroscopy, 6*, 138-163.

Güllü, Ö., Aydoğan, Ş., & Türüt, A. (2008). Fabrication and electrical characteristics of Schottky diode based on organic material. *Microelectronic Engineering, 85*(7), 1647-1651.

Guo, L., Ma, G., Liu, Y., Mi, J., Qian, S., & Qiu, L. (2002). Optical and non-linear optical properties of vanadium oxide phthalocyanine films. *Applied Physics B, 74*(3), 253-257.

Guo, L., Ma, G., Liu, Y., Mi, J., Qian, S., & Qiu, L. (2014). Optical and non-linear optical properties of vanadium oxide phthalocyanine films. *Applied Physics B, 74*(3), 253-257.

Gupta, D. (2007). Organic Electronics II. In *Reach symposium* (pp. 111-117). Kanpur.

Halizan, M. Z. M., Roslan, N. A., Abdullah, S. M., Halim, N. A., Velayutham, T. S., Woon, K. L., & Supangat, A. (2017). Improving the operational voltage of vertical organic field effect transistor (VOFET) by altering the morphology of dielectric layer. *Journal of Materials Science: Materials in Electronics, 28*(16), 11961-11968.

Hamdan, K. S., Abdullah, S. M., Sulaiman, K., & Zakaria, R. (2013). Effects of silver nanoparticles towards the efficiency of organic solar cells. *Applied Physics A, 115*(1), 63-68.

Hamwi, S., Riedl, T., & Kowalsky, W. (2011). An organic pin homojunction as ultra violet light emitting diode and visible-blind photodiode in one. *Applied Physics Letters, 99*(5), 151-153.

Harrey, P. M., Ramsey, B. J., Evans, P. S. A., & Harrison, D. J. (2002). Capacitive-type humidity sensors fabricated using the offset lithographic printing process. *Sensors and Actuators B: Chemical, 87*(2), 226-232.

Ho, K.-C., & Tsou, Y.-H. (2001). Chemiresistor-type NO gas sensor based on nickel phthalocyanine thin films. *Sensors and Actuators B: Chemical, 77*(1), 253-259.

Hohnholz, D., Steinbrecher, S., & Hanack, M. (2000). Applications of phthalocyanines in organic light emitting devices. *Journal of Molecular Structure, 521*(1-3), 231-237.

Hong-Tao, S., Ming-Tang, W., Ping, L., & Xi, Y. (1989). Porosity control of humidity-sensitive ceramics and theoretical model of humidity-sensitive characteristics. *Sensors and Actuators, 19*(1), 61-70.

Hooper, R. W., Zhang, A., Koszelewski, D., Lewtak, J. P., Koszarna, B., Levy, C. J.,... Stillman, M. J. (2018). Differential quenching of the angular momentum of the B and Q bands of a porphyrin as a result of extended ring π-conjugation. *Journal of Porphyrins and Phthalocyanines, 22*(12), 1111-1128.

Horowitz, G. (1998). Organic field ‐ effect transistors. *Advanced Materials, 10*(5), 365-377.

Hu, Z., Tian, M., Nysten, B., & Jonas, A. M. (2009). Regular arrays of highly ordered ferroelectric polymer nanostructures for non-volatile low-voltage memories. *Nature Materials, 8*(1), 62-67.

Huang, J.-S., Hsiao, C.-Y., Syu, S.-J., Chao, J.-J., & Lin, C.-F. (2009). Well-aligned single-crystalline silicon nanowire hybrid solar cells on glass. *Solar Energy Materials and Solar Cells, 93*(5), 621-624.

Ishikawa, Y., Wada, Y., & Toyabe, T. (2010). Origin of characteristics differences between top and bottom contact organic thin film transistors. *Journal of Applied Physics, 107*(5), Article#053709.

Islam, T., Khan, A. U., Akhtar, J., & Rahman, M. Z. U. (2014). A Digital Hygrometer for Trace Moisture Measurement. *IEEE Transactions on Industrial Electronics, 61*(10), 5599-5605.

Islam, T., Kumar, L., & Khan, S. A. (2012). A novel sol–gel thin film porous alumina based capacitive sensor for measuring trace moisture in the range of 2.5–25ppm. *Sensors and Actuators B: Chemical, 173*, 377-384.

Islam, T., Mittal, U., Nimal, A. T., & Sharma, M. U. (2014). A nanoporous thin-film miniature interdigitated capacitive impedance sensor for measuring humidity. *International Journal of Smart and Nano Materials, 5*(3), 169-179.

Islam, T., Nimal, A., Mittal, U., & Sharma, M. (2015). A micro interdigitated thin film metal oxide capacitive sensor for measuring moisture in the range of 175–625 ppm. *Sensors and Actuators B: Chemical, 221*, 357-364.

Islam, T., & Rahman, M. Z. U. (2016). Investigation of the electrical characteristics on measurement frequency of a thin-film ceramic humidity sensor. *IEEE Transactions on Instrumentation and Measurement, 65*(3), 694-702.

Ito, M., Palanisamy, K., Kumar, A., Murugesan, V. S., Shin, P.-K., Tsuda, N.,... Ochiai, S. (2014). Characterization of the organic thin film solar cells with active layers of PTB7/$PC_{71}BM$ prepared by using solvent mixtures with different additives. *International Journal of Photoenergy, 2014*, Article#687678.

Jaisutti, R., Yamwong, W., Atthi, N., Pratontep, S., & Osotchan, T. (2010). *Organic thickness dependence of organic field-effect transistor devices based on pentacene.* Paper presented at the Nanoelectronics Conference (INEC), 2010 3rd International, Hong Kong, China.

Janardhanam, V., Jyothi, I., Lee, J.-H., Kim, J.-Y., Reddy, V. R., & Choi, C.-J. (2014). Electrical properties and carrier transport mechanism of Au/n-GaN schottky contact modified using a copper pthalocyanine (CuPc) interlayer. *Materials Transactions, 55*(5), 758-762.

Jayamurugan, P., Ponnuswamy, V., Subba Rao, Y. V., Ashokan, S., & Meenakshisundar, S. (2015). Influence of spin coating rate on the thickness, surface modification and optical properties of water dispersed PPy composite thin films. *Materials Science in Semiconductor Processing, 39*, 205-210.

Jiang, H., Ye, J., Hu, P., Wei, F., Du, K., Wang, N.,... Kloc, C. (2014). Fluorination of metal phthalocyanines: single-crystal growth, efficient N-channel organic field-effect transistors, and structure-property relationships. *Scientific Reports, 4*, 7573-7579.

Jomaa, T. B., Beji, L., Ltaeif, A., & Bouazizi, A. (2006). The current–voltage characteristics of heterostructures formed by MEH-PPV spin-coated on n-type GaAs and n-type porous GaAs. *Materials Science and Engineering: C, 26*(2-3), 530-533.

Kannappan, S., Palanisamy, K., Tatsugi, J., Shin, P.-K., & Ochiai, S. (2012). Fabrication and characterizations of PCDTBT: $PC_{71}BM$ bulk heterojunction solar cell using air brush coating method. *Journal of Materials Science, 48*(6), 2308-2317.

Karimov, K., Ahmed, M. M., Noshin, F., Saleem, M., Mahroof-Tahir, M., Moiz, S. A., ... Rashid, A. (2015). Nickel phthalocyanine based organic photo transistor: effect of semiconductor film thickness. *The European Physical Journal Applied Physics, 72*(2), 20202-20208.

Karimov, K. S., Ahmad, Z., Fatima, N., Ahmed, M. M., & Abid, M. (2017). Effect of humidity on copper phthalocyanine films deposited at different gravity conditions. *Pigment & Resin Technology, 46*(1), 64-70.

Karimov, K. S., Saleem, M., Qasuria, T. A., & Farooq, M. (2011). Surface-type humidity sensor based on cellulose-PEPC for telemetry systems. *Journal of Semiconductors, 32*(1), Article#015005.

Khan, S. M., Sayyad, M. H., & Karimov, K. S. (2011). Investigation of temperature-dependent electrical properties of p-VOPc/n-si heterojunction under dark conditions. *Ionics, 17*(4), 307-313.

Khanna, V. K., & Nahar, R. K. (1986). Carrier-transfer mechanisms and Al_2O_3 sensors for low and high humidities. *Journal of Physics D: Applied Physics, 19*(7), Article#L141.

Kietzke, T. (2007). Recent advances in organic solar cells. *Advances in OptoElectronics, 2007*, Article#40285.

Kim, C. H., Bonnassieux, Y., & Horowitz, G. (2011). Fundamental benefits of the staggered geometry for organic field-effect transistors. *IEEE Electron Device Letters, 32*(9), 1302-1304.

Korotcenkov, G. (2016). *Porous Silicon: From Formation to Application: Formation and Properties, Volume One: Formation and Properties*. Boca Raton: CRC Press.

Koster, L. J. A., Smits, E. C. P., Mihailetchi, V. D., & Blom, P. W. M. (2005). Device model for the operation of polymer/fullerene bulk heterojunction solar cells. *Physical Review B, 72*(8), Article#085205.

Krebs, F. C. (2009). Fabrication and processing of polymer solar cells: A review of printing and coating techniques. *Solar Energy Materials and Solar Cells, 93*(4), 394-412.

Krier, A., Abass, A., & Collins, R. (1993). The influence of chlorine on the optical properties of monoclinic lead phthalocyanine thin films. *Advanced Functional Materials, 2*(6), 289-293.

Kudo, K., Iizuka, M., Kuniyoshi, S., & Tanaka, K. (2001). Device characteristics of lateral and vertical type organic field effect transistors. *Thin Solid Films, 393*(1-2), 362-367.

Kudo, K., Takano, T., Yamauchi, H., Iizuka, M., & Nakamura, M. (2010). High-speed operation of step-edge vertical-channel organic transistors with pentacene and 6, 13-Bis (triisopropyl-silylethynyl) pentacene. *Japanese Journal of Applied Physics, 49*(4S), Article#04DK03.

Kudo, K., Wang, D. X., Iizuka, M., Kuniyoshi, S., & Tanaka, K. (1998). Schottky gate static induction transistor using copper phthalocyanine films. *Thin Solid Films, 331*(1-2), 51-54.

Kvitschal, A., Cruz-Cruz, I., & Hümmelgen, I. A. (2015). Copper phthalocyanine based vertical organic field effect transistor with naturally patterned tin intermediate grid electrode. *Organic Electronics, 27*, 155-159.

Kymissis, I. (2008). *Organic Field Effect Transistors: Theory, Fabrication and Characterization*. United States: Springer Science & Business Media.

Lai, S., Viola, F., Cosseddu, P., & Bonfiglio, A. (2018). Floating gate, organic field-effect transistor-based sensors towards biomedical applications fabricated with large-area processes over flexible substrates. *Sensors (Basel), 18*(3), 688-700.

Lee, Y.-L., Hsiao, C.-Y., & Hsiao, R.-H. (2004). Annealing effects on the gas sensing properties of copper phthalocyanine films. *Thin Solid Films, 468*(1-2), 280-284.

Leonat, L., Sbarcea, G., & Branzoi, I. V. (2013). Cyclic voltammetry for energy levels estimation of organic materials. *U.P.B. Scientific Bulletin Series B, 75(3)*, 111-118.

Leznoff, C. C., Lever, A. B. P. (1989). *Phthalocyanines: Properties and Applications.* Germany: Wiley.

Li, L., Tang, Q., Li, H., Hu, W., Yang, X., Shuai, Z., . . . Zhu, D. (2008). Organic thin-film transistors of phthalocyanines. *Pure and Applied Chemistry, 80*(11), 2231-2240.

Li, L., Zhang, F., Wang, J., An, Q., Sun, Q., Wang, W., . . . Teng, F. (2015). Achieving EQE of 16,700% in P3HT:$PC_{71}BM$ based photodetectors by trap-assisted photomultiplication. *Scientific Reports, 5*, 9181-9188.

Li, M., Meng, G., Huang, Q., & Zhang, S. (2014). Improved sensitivity of polychlorinated-biphenyl-orientated porous-ZnO surface photovoltage sensors from chemisorption-formed ZnO-CuPc composites. *Scientific Reports, 4*, 4284-4290.

Li, S.-H., Xu, Z., Yang, G., Ma, L., & Yang, Y. (2008). Solution-processed poly (3-hexylthiophene) vertical organic transistor. *Applied Physics Letters, 93*(21), 426-429.

Lim, L. W., Aziz, F., Muhammad, F. F., Supangat, A., & Sulaiman, K. (2016). Electrical properties of Al/PTB7-Th/n-Si metal-polymer-semiconductor Schottky barrier diode. *Synthetic Metals, 221*, 169-175.

Liqiang, J., Yichun, Q., Baiqi, W., Shudan, L., Baojiang, J., Libin, Y., . . . Jiazhong, S. (2006). Review of photoluminescence performance of nano-sized semiconductor materials and its relationships with photocatalytic activity. *Solar Energy Materials and Solar Cells, 90*(12), 1773-1787.

Liu, J., Herlogsson, L., Sawatdee, A., Favia, P., Sandberg, M., Crispin, X., . . . Berggren, M. (2010). Vertical polyelectrolyte-gated organic field-effect transistors. *Applied Physics Letters, 97*(10), 197-200.

Ma, L., & Yang, Y. (2004). Unique architecture and concept for high-performance organic transistors. *Applied Physics Letters, 85*(21), 5084-5086.

Mahdi, R., Gan, W., & Majid, W. (2014). Hot plate annealing at a low temperature of a thin ferroelectric P(VDF-TrFE) film with an improved crystalline structure for sensors and actuators. *Sensors (Basel), 14*(10), 19115-19127.

Mao, D., Gnade, B. E., & Quevedo-Lopez, M. A. (2011). Ferroelectric properties and polarization switching kinetic of poly(vinylidene fluoride-trifluoroethylene) copolymer. In *Ferroelectrics-Physical Effects*. IntechOpen, London, United Kingdom.

Matsuguchi, M., Umeda, S., Sadaoka, Y., & Sakai, Y. (1998). Characterization of polymers for a capacitive-type humidity sensor based on water sorption behavior. *Sensors and Actuators B: Chemical, 49*(3), 179-185.

Meixner, R., Göbel, H., Yildirim, F., Bauhofer, W., & Krautschneider, W. (2006). Wavelength-selective organic field-effect phototransistors based on dye-doped poly-3-hexylthiophene. *Applied Physics Letters, 89*(9), Article#092110.

Melville, O. A., Lessard, B. H., & Bender, T. P. (2015). Phthalocyanine-based organic thin-film transistors: A review of recent advances. *ACS Applied Material Interfaces, 7*(24), 13105-13118.

Missoum, I., Ocak, Y., Benhaliliba, M., Benouis, C., & Chaker, A. (2016). Microelectronic properties of organic Schottky diodes based on MgPc for solar cell applications. *Synthetic Metals, 214*, 76-81.

Mittal, P., Kumar, B., Negi, Y. S., Kaushik, B. K., & Singh, R. (2012). Channel length variation effect on performance parameters of organic field effect transistors. *Microelectronics Journal, 43*(12), 985-994.

Mohammadian-Kohol, M., Asgari, M., & Shakur, H. (2016). A detailed investigation of the gamma-ray radiation effects on the optical properties of polyvinyl butyral film. *Optic-International Journal for Light and Electron Optics, 127*(19), 7459-7468.

Morris, J. E., & Iniewski, K. (2017). *Nanoelectronic device applications handbook*. Boca Raton: CRC Press.

Motaung, D. E., Malgas, G. F., Arendse, C. J., Mavundla, S. E., & Knoesen, D. (2009). Structural and photo-physical properties of spin-coated poly(3-hexylthiophene) thin films. *Materials Chemistry and Physics, 116*(1), 279-283.

Muhammad, F. F., & Sulaiman, K. (2011). Effects of thermal annealing on the optical, spectroscopic, and structural properties of tris (8-hydroxyquinolinate) gallium films grown on quartz substrates. *Materials Chemistry and Physics, 129*(3), 1152-1158.

Muhammad, F. F., Yahya, M. Y., & Sulaiman, K. (2017). Improving the performance of solution-processed organic solar cells by incorporating small molecule acceptors into a ternary bulk heterojunction based on DH6T:Mq3:PCBM (M = Ga, Al). *Materials Chemistry and Physics, 188*, 86-94.

Murugesan, V. S., Ono, S., Tsuda, N., Yamada, J., Shin, P.-K., & Ochiai, S. (2015). characterization of organic thin film solar cells of PCDTBT:$PC_{71}BM$ prepared by different mixing ratio and effect of hole transport layer. *International Journal of Photoenergy, 2015*, 1-8.

Najeeb, M. A., Abdullah, S. M., Aziz, F., Ahmad, Z., Shakoor, R., Mohamed, A., . . . Sulaiman, K. (2016). A comparative study on the performance of hybrid solar cells containing ZnSTe QDs in hole transporting layer and photoactive layer. *Journal of Nanoparticle Research, 18*(12), 384-392.

Nanai, N., Yudasaka, M., Ohki, Y., & Yoshimura, S. (1995). Structures of vanadyl phthalocyanine in bilayers of vanadyl phthalocyanine and perylenetetracarboxylic dianhydride. *Thin Solid Films, 265*(1-2), 1-2.

Nappa, M., & Valentine, J. S. (1978). The influence of axial ligands on metalloporphyrin visible absorption spectra. Complexes of tetraphenylporphinatozinc. *Journal of the American Chemical Society, 100*(16), 5075-5080.

Nguyen, A., & Lee, P. (2006). *Ferroelectric copolymer P(VDF-TrFE) as gate dielectric in organic field effect transistors for memory application devices.* Paper presented at the 2006 IEEE Conference on Emerging Technologies - Nanoelectronics, Singapore.

Nyokong, T. (2010). Electronic spectral and electrochemical behavior of near infrared absorbing metallophthalocyanines. In *Functional Phthalocyanine Molecular Materials* (pp. 45-87). Berlin: Springer.

Ochiai, S., Imamura, S., Kannappan, S., Palanisamy, K., & Shin, P.-K. (2013). Characteristics and the effect of additives on the nanomorphology of PTB7/PC$_{71}$BM composite films. *Current Applied Physics, 13*, S58-S63.

Ochiai, S., Uchiyama, M., Kannappan, S., Jayaraman, R., & Shin, P.-K. (2012). Evaluation of the performance of an organic thin film solar cell prepared using the active layer of poly [[9-(1-octylnonyl)-9h-carbazole-2.7-diyl]-2.5-thiophenediyl-2.1. 3-benzothiadiazole-4.7-diyl-2.5-thiophenediyl]/[6, 6]-phenyl c 71 butyric acid methyl ester composite thin film. *Transactions on Electrical and Electronic Materials, 13*(1), 43-46.

Oleinick, N. L., Antunez, A. R., Clay, M. E., Rihter, B. D., & Kenney, M. E. (1993). New phthalocyanine photosensitizers for photodynamic therapy. *Photochemistry and photobiology, 57*(2), 242-247.

Padilla, M., Michl, B., Thaidigsmann, B., Warta, W., & Schubert, M. C. (2014). Short-circuit current density mapping for solar cells. *Solar Energy Materials and Solar Cells, 120*, 282-288.

Pan, Y., Wu, Y., Chen, L., Zhao, Y., Shen, Y., Li, F., . . . Huang, D. (1998). Structure and spectroscopic characterization of polycrystalline vanadyl phthalocyanine (VOPc) films fabricated by vacuum deposition. *Applied Physics A: Materials Science & Processing, 66*(5), 569-573.

Park, K. T., Miller, A., Klier, K., Opila, R. L., & Rowe, J. E. (2003). Heteroepitaxial copper phthalocyanine on Au(0 0 1) studied by high-resolution X-ray photoelectron spectroscopy. *Surface Science, 529*(3), L285-L292.

Perkinson, J. C. (2007). Organic field-effect transistors. Retrieved on March, 29, 2017, from http://web.mit.edu/joyp/Public/OFET%20Term%20Paper.pdf.

Przybyl, B., & Janczak, J. (2014). Structural characterisation and DFT calculations of three new complexes of zinc phthalocyanine with n-alkylamines. *Dyes and Pigments, 100*(1), 247-254.

Qi, Q., Zhang, T., Wang, S., & Zheng, X. (2009). Humidity sensing properties of KCl-doped ZnO nanofibers with super-rapid response and recovery. *Sensors and Actuators B: Chemical, 137*(2), 649-655.

Rafique, S., Abdullah, S. M., Mahmoud, W. E., Al-Ghamdi, A. A., & Sulaiman, K. (2016). Stability enhancement in organic solar cells by incorporating V_2O_5 nanoparticles in the hole transport layer. *RSC Advances, 6*(55), 50043-50052.

Rajaputra, S., Vallurupalli, S., & Singh, V. P. (2007). Copper phthalocyanine based Schottky diode solar cells. *Journal of Materials Science: Materials in Electronics, 18*(11), 1147-1150.

Rand, B. P., Cheyns, D., Vasseur, K., Giebink, N. C., Mothy, S., Yi, Y., . . . Brédas, J. L. (2012). The impact of molecular orientation on the photovoltaic properties of a phthalocyanine/fullerene heterojunction. *Advanced Functional Materials, 22*(14), 2987-2995.

Rao, S. V., Anusha, P. T., Prashant, T. S., Swain, D., & Tewari, S. P. (2011). Ultrafast nonlinear optical and optical limiting properties of phthalocyanine thin films studied using Z-scan. *Materials Sciences and Applications, 2*(05), 299-310.

Raza, E., Asif, M., Aziz, F., Azmer, M. I., Malik, H. A., Teh, C.-H., . . . Sulaiman, K. (2016). Influence of thermal annealing on a capacitive humidity sensor based on newly synthesized macroporous $PBObzT_2$. *Sensors and Actuators B: Chemical, 235*, 146-153.

Reséndiz, L., Estrada, M., Cerdeira, A., Iñiguez, B., & Deen, M. (2010). Effect of active layer thickness on the electrical characteristics of polymer thin film transistors. *Organic Electronics, 11*(12), 1920-1927.

Rittersma, Z. M. (2002). Recent achievements in miniaturised humidity sensors—a review of transduction techniques. *Sensors and Actuators A: Physical, 96*(2), 196-210.

Roncali, J. (2009). Molecular bulk heterojunctions: an emerging approach to organic solar cells. *Accounts of chemical research, 42*(11), 1719-1730.

Roslan, N. A., Abdullah, S. M., Halizan, M. Z. M., Bawazeer, T. M., Alsenany, N., Alsoufi, M. S., . . . Supangat, A. (2018). VTP as an Active Layer in a Vertical Organic Field Effect Transistor. *Journal of Electronic Materials, 47*(3), 2184-2191.

Roslan, N. A., Abdullah, S. M., Majid, W. H. A., & Supangat, A. (2018). Investigation of VTP:$PC_{71}BM$ organic composite as highly responsive organic photodetector. *Sensors and Actuators A: Physical, 279*, 361-366.

Rossi, G., d'Acapito, F., Amidani, L., Boscherini, F., & Pedio, M. (2016). Local environment of metal ions in phthalocyanines: K-edge X-ray absorption spectra. *Physical Chemistry Chemical Physics, 18*(34), 23686-23694.

Rubio, M., Roos, B. O., Serrano-Andrés, L., & Merchán, M. (1999). Theoretical study of the electronic spectrum of magnesium-porphyrin. *The Journal of Chemical Physics, 110*(15), 7202-7209.

Sakamoto, K., & Ohno, E. (1997). Synthesis and electron transfer property of phthalocyanine derivatives. *Progress in Organic Coatings, 31*(1-2), 139-145.

Sánchez-Vergara, M. E., Alonso-Huitron, J. C., Rodriguez-Gómez, A., & Reider-Burstin, J. N. (2012). Determination of the optical GAP in thin films of amorphous dilithium phthalocyanine using the Tauc and Cody models. *Molecules, 17*(9), 10000-10013.

Sarjidan, M. M., Shuhaimi, A., & Majid, W. A. (2018). Observation of saturation transfer characteristics in solution processed vertical organic field-effect transistors (VOFETs) with high leakage current. *Current Applied Physics, 18*(11), 1415-1421.

Sayyad, M. H., Saleem, M., Karimov, K. S., Yaseen, M., Ali, M., Cheong, K. Y., & Noor, A. F. M. (2010). Synthesis of Zn (II) 5, 10, 15, 20-tetrakis (4′ -isopropylphenyl) porphyrin and its use as a thin film sensor. *Applied Physics A, 98*(1), 103-109.

Schlaf, R., Schroeder, P., Nelson, M., Parkinson, B., Merritt, C., Crisafulli, L., . . . Kafafi, Z. (2000). Determination of interface dipole and band bending at the Ag/tris (8-hydroxyquinolinato) gallium organic Schottky contact by ultraviolet photoemission spectroscopy. *Surface Science, 450*(1-2), 142-152.

Scott, J. C., & Malliaras, G. G. (1999). Charge injection and recombination at the metal–organic interface. *Chemical Physics Letters, 299*(2), 115-119.

Servaites, J. D., Ratner, M. A., & Marks, T. J. (2011). Organic solar cells: A new look at traditional models. *Energy & Environmental Science, 4*(11), 4410-4422.

Shafiee, A., Salleh, M. M., & Yahaya, M. (2011). Determination of HOMO and LUMO of [6, 6]-phenyl C61-butyric acid 3-ethylthiophene ester and poly (3-octyl-thiophene-2, 5-diyl) through voltametry characterization. *Sains Malaysiana, 40*(2), 173-176.

Shang, D., Wang, Q., Chen, L., Dong, R., Li, X., & Zhang, W. (2006). Effect of carrier trapping on the hysteretic current-voltage characteristics in Ag/La 0.7 Ca 0.3 MnO 3⁄ Pt heterostructures. *Physical Review B, 73*(24), Article#245427.

Speight, J. G. (2019). *Handbook of industrial hydrocarbon processes*: Gulf Professional Publishing.

Srinivasan, M. V., Tsuda, N., Shin, P.-K., & Ochiai, S. (2015). Performance evaluation of PTB7 : PC71BM based organic solar cells fabricated by spray coating method using chlorine free solvent. *RSC Advances, 5*(69), 56262-56269.

Stenzel, O. (2005). *The physics of thin film optical spectra*. Switzerland: Springer.

Stutzmann, N., Friend, R. H., & Sirringhaus, H. (2003). Self-aligned, vertical-channel, polymer field-effect transistors. *Science, 299*(5614), 1881-1884.

Takano, T., Yamauchi, H., Iizuka, M., Nakamura, M., & Kudo, K. (2009). High-speed operation of vertical type organic transistors utilizing step-edge structures. *Applied Physics Express, 2*(7), Article#071501.

Tang, C. W. (1986). Two‐layer organic photovoltaic cell. *Applied Physics Letters, 48*(2), 183-185.

Tessler, N., & Ben-Sasson, A. (2014). Vertical organic field effect transistor and method of its manufacture. In: Google Patents #13. Retrieved on September, 18, 2017, from https://app.dimensions.ai/details/patent/WO-2010113163-A1.

Tripathy, A., Pramanik, S., Cho, J., Santhosh, J., & Osman, N. A. (2014). Role of morphological structure, doping, and coating of different materials in the sensing characteristics of humidity sensors. *Sensors (Basel), 14*(9), 16343-16422.

Tzeng, S., Hon, M., & Leu, I. (2010). Improvement in the photocurrent to dark current contrast ratio of ZnO/Au Schottky photodetector with PMMA microlens arrays. *Journal of The Electrochemical Society, 157*(10), H919-H923.

Usta, H., & Facchetti, A. (2015). Polymeric and small-molecule semiconductors for organic field-effect transistors. In *large area and flexible electronics* (pp. 1-100). John Wiley & Sons.

Viezbicke, B. D., Patel, S., Davis, B. E., & Birnie III, D. P. (2015). Evaluation of the Tauc method for optical absorption edge determination: ZnO thin films as a model system. *Physica Status Solidi (b), 252*(8), 1700-1710.

Wan, C., & Bowen, C. R. (2017). Multiscale-structuring of polyvinylidene fluoride for energy harvesting: the impact of molecular-, micro-and macro-structure. *Journal of Materials Chemistry A, 5*(7), 3091-3128.

Wang, H., Ji, Z., Liu, M., Shang, L., Liu, G., Liu, X., . . . Peng, Y. (2009). Advances in organic field-effect transistors and integrated circuits. *Science in China Series E: Technological Sciences, 52*(11), 53-65.

Wang, H., Wang, X., Fan, P., Yang, X., & Yu, J. (2015). Enhanced power conversion efficiency of P3HT:PC$_{71}$BM bulk heterojunction polymer solar cells by doping a high-mobility small organic molecule. *International Journal of Photoenergy, 2015*. Article#982064.

Wang, S., Kang, Y., Wang, L., Zhang, H., Wang, Y., & Wang, Y. (2013). Organic/inorganic hybrid sensors: A review. *Sensors and Actuators B: Chemical, 182*, 467-481.

Wang, X., Li, H., Su, Z., Fang, F., Zhang, G., Wang, J., . . . Li, B. (2014). Efficient organic near-infrared photodetectors based on lead phthalocyanine/C60 heterojunction. *Organic Electronics, 15*(10), 2367-2371.

Warner, M., Din, S., Tupitsyn, I. S., Morley, G. W., Stoneham, A. M., Gardener, J. A., . . . Kay, C. W. (2013). Potential for spin-based information processing in a thin-film molecular semiconductor. *Nature, 503*(7477), 504.

Xu, B., Gopalan, S.-A., Gopalan, A.-I., Muthuchamy, N., Lee, K.-P., Lee, J.-S., . . . Kim, J.-S. (2017). Functional solid additive modified PEDOT: PSS as an anode buffer layer for enhanced photovoltaic performance and stability in polymer solar cells. *Scientific Reports, 7*, Article#45079.

Yakuphanoglu, F. (2007). Photovoltaic properties of hybrid organic/inorganic semiconductor photodiode. *Synthetic Metals, 157*(21), 859-862.

Yang, D., & Ma, D. (2019). Development of organic semiconductor photodetectors: from mechanism to applications. *Advanced Optical Materials, 7*(1), Article#1800522.

Yang, Y., & Wudl, F. (2006). *High Performance Organic Materials and Devices*. Retrieved on September, 18, 2016 from https://apps.dtic.mil/dtic/tr/fulltext/u2/a445122.pdf.

Yi, R., Lou, Z., Hu, Y., Cui, S., Teng, F., Hou, Y., & Liu, X. (2014). Effects of gate dielectric thickness and semiconductor thickness on device performance of organic field-effect transistors based on pentacene. *Science China Technological Sciences, 57*(6), 1142-1146.

Yildirim, F., Ucurum, C., Schliewe, R., Bauhofer, W., Meixner, R., Goebel, H., & Krautschneider, W. (2007). Spin-cast composite gate insulation for low driving voltages and memory effect in organic field-effect transistors. *Applied Physics Letters, 90*(8), Article#083501.

Yu, H., Dong, Z., Guo, J., Kim, D., & So, F. (2016). Vertical organic field-effect transistors for integrated optoelectronic applications. *ACS Applied Material Interfaces, 8*(16), 10430-10435.

Yuen, A. P., Jovanovic, S. M., Hor, A.-M., Klenkler, R. A., Devenyi, G. A., Loutfy, R. O., & Preston, J. S. (2012). Photovoltaic properties of M-phthalocyanine/fullerene organic solar cells. *Solar Energy, 86*(6), 1683-1688.

Zafar, Q., Ahmad, Z., & Sulaiman, K. (2015). PFO-DBT: MEH-PPV:$PC_{71}BM$ ternary blend assisted platform as a photodetector. *Sensors (Basel), 15*(1), 965-978.

Zafar, Q., Ahmad, Z., Sulaiman, K., Hamzah, A. S., & Rahman, Z. A. (2014). A MEHPPV/VOPcPhO composite based diode as a photodetector. *Sensors and Actuators A: Physical, 206*, 138-143.

Zafar, Q., Aziz, F., & Sulaiman, K. (2016). Eco-benign visible wavelength photodetector based on phthalocyanine-low bandgap copolymer composite blend. *RSC Advances, 6*(16), 13101-13109.

Zafar, Q., Fatima, N., Karimov, K. S., Ahmed, M. M., & Sulaiman, K. (2017). Realizing broad-bandwidth visible wavelength photodiode based on solution-processed ZnPc/$PC_{71}BM$ dyad. *Optical Materials, 64*, 131-136.

Zafar, Q., Najeeb, M. A., Ahmad, Z., & Sulaiman, K. (2015). Organic–inorganic hybrid nanocomposite for enhanced photo-sensing of PFO-DBT:MEH-PPV:$PC_{71}BM$ blend-based photodetector. *Journal of Nanoparticle Research, 17*(9), 372-382..

Zhang, F., Gadisa, A., Inganäs, O., Svensson, M., & Andersson, M. (2004). Influence of buffer layers on the performance of polymer solar cells. *Applied Physics Letters, 84*(19), 3906-3908.

Zhang, Y., Learmonth, T., Wang, S., Matsuura, A. Y., Downes, J., Plucinski, L., . . . Smith, K. E. (2007). Electronic structure of the organic semiconductor vanadyl phthalocyanine (VO-Pc). *Journal of Materials Chemistry, 17*(13), 1276-1283.

Zhang, Z., Yuan, J., Wei, Q., & Zou, Y. (2018). Small-molecule electron acceptors for efficient non-fullerene organic solar cells. *Frontiers in Chemistry, 6*, Article#414.

Zhou, L., Zhuang, J. Y., Tongay, S., Su, W. M., & Cui, Z. (2013). Performance improvement of organic light emitting diode with aluminum oxide buffer layer for anode modification. *Journal of Applied Physics, 114*(7), Article#074506.

Zhou, Y., Han, S.-T., & Roy, V. A. L. (2014). 6 - Nanocomposite dielectric materials for organic flexible electronics. In S.-C. Tjong (Ed.), *Nanocrystalline Materials (Second Edition)* (pp. 195-220). Oxford, United Kingdom: Elsevier.

LIST OF PUBLICATIONS & PAPER PRESENTED

List of publications:

1. **Roslan, N. A.,** Abdullah, S. M., Halizan, M. Z. M., Bawazeer, T. M., Alsenany, N., Alsoufi, M. S., . . . Supangat, A. (2018). VTP as an Active Layer in a Vertical Organic Field Effect Transistor. *Journal of Electronic Materials, 47*(3), 2184-2191.

2. **Roslan, N. A.,** Abdullah, S. M., Majid, W. H. A., & Supangat, A. (2018). Investigation of VTP:$PC_{71}BM$ organic composite as highly responsive organic photodetector. *Sensors and Actuators A: Physical, 279*, 361-366.

3. **Roslan, N. A.,** Bakar, A. A., Bawazeer, T. M., Alsoufi, M. S., Alsenany, N., Majid, W. H. A., & Supangat, A. (2018). Enhancing the performance of vanadyl phthalocyanine-based humidity sensor by varying the thickness. *Sensors and Actuators B: Chemical*, *279*, 148-156.

Papers presented:

1. **Roslan, N. A.,** Abdullah, S. M., Majid, W. H. A., & Supangat, A. (2016). *Investigation of VTP as an active component in vertical organic field effect transistor.* Presented at National Physics Conference 2016 (PERFIK). 21 - 22 December 2016. Pullman Hotel, Kuala Lumpur, Malaysia.

2. **Roslan, N. A.**, Abdullah, S. M., Majid, W. H. A., & Supangat, A. (2018). *Investigation of VTP:$PC_{71}BM$ organic composite as highly responsive organic photodetector.* Presented at 1st UTM Emerging Scientists Conference, (UTM-ESCon) (2018). Johor Bahru, Malaysia.

3. **Roslan, N. A.,** Abdullah, S. M., Majid, W. H. A., & Supangat, A. (2018). *Photosensing performance of metal phthalocyanine/fullerene hetorojunction.* Bilateral Symposium on Advanced Materials between UM-NTU. 13 August 2018. University of Malaya, Kuala Lumpur. (Poster presentation).

4. **Roslan, N. A.,** Abdullah, S. M., Majid, W. H. A., & Supangat, A. (2019). *A novel hole transport layer based on UV-Ozone treated graphene oxide/PEDOT:PSS for highly efficient and stable organic solar cells (OSCs).* 18th International Symposium on Novel Aromatic Compounds (ISNA-18), (2019), Sapporo Convention Centre, Japan.